Order Number 9304647

Pitting corrosion of stainless steels: Microanalytical studies of pitting corrosion and analysis of corrosion transients

Cho, Jeong-Hwan, Ph.D.

City University of New York, 1992

U·M·I
300 N. Zeeb Rd.
Ann Arbor, MI 48106

PITTING CORROSION OF STAINLESS STEELS: MICROANALYTICAL STUDIES OF PITTING CORROSION AND ANALYSIS OF CORROSION TRANSIENTS

by
Jeong-Hwan Cho

A dissertation submitted to the Graduate Faculty in Chemistry in partial fulfillment of the requirements for the degree of Doctor of Philosophy, The City University of New York.

1992

This manuscript has been read and accepted for the Graduate Faculty in Chemistry in satisfaction of the dissertation requirement for the degree of Doctor of Philosophy.

7/20/92
Date

M. Tomkiewicz
Prof. Micha Tomkiewicz
Chair of Examining Committee

7/27/92
Date

Executive Officer

H. Isaacs
Dr. H. Isaacs, Brookhaven National Laboratory

A. Davenport
Dr. A. Davenport, Brookhaven National Laboratory

D. Howery
Prof. D. Howery, Brooklyn College

Supervisory Committee

The City University of New York

Abstract

PITTING CORROSION OF STAINLESS STEELS: MICROANALYTICAL STUDIES OF PITTING CORROSION AND ANALYSIS OF CORROSION TRANSIENTS

by

Jeong-Hwan Cho

Advisor: Professor Micha Tomkiewicz

The chemical compositions of the highly concentrated solutions developed during pitting corrosion of a commercial stainless steel foil in a 0.5 M NaCl + 0.5 M HCl solution were investigated. The application of *in situ* x-ray fluorescence microscopy (XRM) to investigate the chemical compositions of the solutions within a one-dimensional artificial pit was discussed. The saturated concentration at the metal interface during anodic dissolution was obtained at approximately 4.7 $\pm$ 0.1 M for the commercial stainless steel sample. The ratios of the relative metal ion concentrations along the pit were correlated with the diffusion coefficients of each species.

Video optical microscopy attached to the XRM beamline was applied to investigate the properties of salt films forming at metal interfaces during anodic dissolution of metals in acidic chloride solutions. The observation from the optical microscope showed that the thickness of the steady state salt film in the 1 - 2 mm deep artificial pit of the stainless steel foil at a constant potential of 600 mV (*vs.* SCE) was

approximately 5 - 10 μm. A more precise results obtained from the XRM data analysis showed that the ratio of metallic elements in the salt layer is Fe : Cr : Ni = 88 : 6 : 6, which is quite different from the metal (69 : 18 :13) and the solution (67 :22 : 11). Also, the thickness dependence on the applied potential and on the pit depth was observed.

AC impedance measurements on passive metal surfaces were investigated. The constant phase angle (θ) of 80° and the linear dependence of the magnitude on frequency in the range of 1 - 1000 Hz were the characteristic of the AC impedance with a uniform current density, Z_i, of the stainless steel electrode in Na_2SO_4 solutions. The magnitudes and the phase angles of the apparent impedance measured at different positions of electrode surfaces decreased exponentially depending upon the capacitance of electrode surface and the solution resistance. The effect of a local corrosion site along a transmission line on the apparent impedance measurements was investigated.

Acknowledgements

I would like to thank Professor Micha Tomkiewicz for his guidance and encouragement during this research. I express my inmost appreciation to Dr. Hugh Isaacs, who guided me with patience, and I am especially grateful to him for his contineous support and key suggestions during the entire research work. Dr. Alison Davenport's intuitions and advices in many areas of this work are also indebtedly acknowledged.

My special thanks are due to a number of people for their assistant: Drs. M. Rivers and S. Sutton from U. of Chicago (X-ray fluorescence microscopy), Dr. B. Sabatini (Scanning Electron microscopy), and Mr. K. Sutter (Technical assistant) at Brookhaven National Laboratory. I am pleased to acknowledge the support and helpful discussions of my colleagues (Mr. A. Aldykiewicz and Ms. M. Taube) in the Corrosion Group at Brookhaven National Laboratory.

I offer my special gratefulness to my family, especially to my wife Kum-Hee and my son Seung-Wook, for their dedication and countless support during the work.

Jeong-Hwan Cho.

July, 1992.

Table of Contents

List of Figures

List of Tables

Chapter 1

PITTING CORROSION OF STAINLESS STEELS

Corrosion is a destructive process describing electrochemical or chemical attack on metals and alloys in various environments. Corrosive processes may result in either uniform or local attack of the metal. Types of localized corrosion are: pitting, crevice, intergranular corrosion, stress corrosion cracking and corrosion fatigue. Crevice corrosion can occur within crevices or at shielded surfaces where a stagnant solution is present. The crevices can be formed by metal/metal or metal/nonmetal junctions. Intergranular corrosion is found at grain boundaries, which are disordered misfit regions separating grains of different crystallographic orientations. The misfit regions are favored sites for segregation or depletion of solute elements and precipitation of metal compounds. These changes (segregation, depletion or precipitation) lead to grain boundary attack and localized corrosion. Stress corrosion cracking occurs in the presence of tensile stress, either residual, applied or a combination of both, in corrosive environments. Corrosion fatigue is explained by the fatigue cracking of a metal under repeated cyclic stresses in the presence of liquid or gaseous environments that may or may not be particularly corrosive to the unstressed metals.

Many metals and alloys are usually protected from corrosive attacks by thin oxide films. Pitting is a form of localized corrosion attack which takes place on metals and

alloys covered by passive oxide films in the presence of aggressive anions such as chloride. It is generally understood that the process of pitting corrosion is a complex set of physical, chemical and electrochemical reactions occurring at the metal/solution interface. Extensive discussions concerning pitting corrosion have been presented in the literature (1-21) including passivity, mechanisms of pit initiation, solution chemistry within pits, dissolution kinetics, metal microstructure, alloying effects and environmental effects. The purpose of this chapter is to describe the various phenomena of pitting corrosion on stainless steels in chloride environments, such as mechanisms of pit initiation, properties of passive oxide films, chemistry of pit solution and salt layer.

1.1 Theories of Pit Initiation

The first stage of pitting corrosion is considered to be the failure of the passive layer followed by its breakdown. The failure of the passive layer will then lead either to repassivation or to pit propagation. Therefore pitting corrosion can be divided into two stages; initiation and propagation. Mechanisms of pit initiation have been addressed extensively in the literature (1-4,22-48) and the proposed major models include adsorption, penetration and migration, mechanical breakdown of the oxide film, localized acidification and point defect model (PDM).

1.1.1 Adsorption Theories

The adsorption theory was initially proposed by Uhlig (22-24) who described competitive adsorption of oxygen and chloride ions on the metal surface. The

competitive adsorption theory was based on the fact that the passive film was an adsorbed layer of oxygen on the metal surface, which is not correct for many metals and alloys (25). The theory was subsequently supported by Kolotyrkin (26,27) who suggested that pitting potential E_{np} was the potential at which the adsorption of aggressive anions on the metal surface displaces the adsorbed passivating species.

The localized adsorption theory explains that pit nucleation may begin with the formation of a chloride salt layer on the passive oxide surface (28-30). Heusler and Fisher (28) proposed that chemisorbed chlorides replace oxygen or hydroxyl ions at the passive surface which might lead to the formation of two dimensional chloride islands under which there was localized reduction in the thickness of the passive layer. The favored sites on the passive surfaces for chloride islands were not specified. However, Janik-Czachor (30) supported a different mechanism of pit initiation based on local adsorption theory and suggested that chloride ions locally accumulated at certain active sites on the passive film. The active sites were thought to be non-metallic inclusions and inhomogeneities on the film.

1.1.2 Penetration and Migration Theory

The penetration and migration theory mainly explains the specific ability of chloride ions to create pitting (31-35). Evans (31) first suggested this model and explained that chloride anions can permeate through the protective oxide film. Pryor (35) suggested that chloride incorporation occurred via substitution and exchange process

with oxygen ions, which required Al^{3+} ions from the lattice to enter solution to restore electroneutrality.

1.1.3 Mechanical Breakdown of Passivity

This model is based on local breakdown of the oxide film by mechanical forces (36,37). The mechanical breakdown theory suggests that the local breakdown of the oxide film may occurred due to a combination of electrostriction and surface tension (36). Chloride ions which adsorbed locally on the interface could reduce the surface tension of the film. Hoar (37) postulated that the adsorbing anions replace water on the oxide/solution interface and reduce the interfacial tension or interfacial free energy by mutually repulsive forces between the charged particles. The adsorbed anions push each other and produce cracks on the oxide film. The anions can further penetrate into the crack sites of the oxide and eventually induce local breakdown of the oxide film.

1.1.4 Localized Acidification Theory

This theory assumes that metal ions hydrolyze inside micropits already existing on the oxide film and that corrosion products diffuse into the bulk electrolyte (38-40). The local acidification theory is applicable not only to pit initiation, but also to pit propagation. Galvele (39,40) first proposed an unidirectional pit model and explained that metal dissolution and metal hydrolysis reaction took place on bare metal sites after breakdown of the oxide film, leading to local acidification.

The pit model (38) in one-dimension, shown in Fig. 1.1, was presented to calculate acidity and concentrations of ions in the pit as a function of $x \cdot i$, where x is the pit depth and i is the current density. The key assumptions in the model (38) were:

1. Metal dissolution only occurs at the bottom of the pit. The following general reaction was used:

$$Me = Me^{n+} + ne \qquad [1\text{-}1]$$

2. Reaction [1-1] is followed by the full hydrolysis reactions:

$$Me^{n+} + H_2O \rightleftharpoons Me(OH)^{(n-1)+} + H^+$$

$$Me(OH)^{+}_{n-1} + H_2O \rightleftharpoons Me(OH)_n + H^+ \qquad [1\text{-}2]$$

3. The aggressive anions act as a supporting electrolyte for the ionic species formed by reactions [1-1] and [1-2].

A critical acidification is necessary to hinder repassivation processes and sustain pit activity. For the majority of metals such as Zn, Fe, Ni, Co and Al, the necessary acidification can be established in pits as deep as 10^{-6} cm, the value of which was deduced from a calculation showing that the critical pH is reached with $x \cdot i$ below 10^{-6} A/cm (40).

1.1.5 Point Defect Model (PDM)

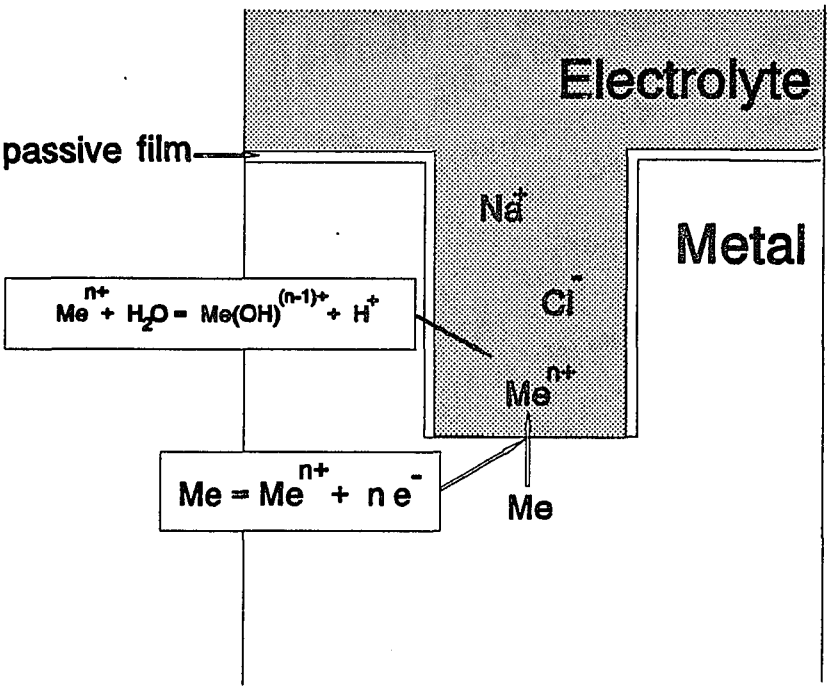

Fig. 1.1. Unidirectional pit model with side walls protected by passive film (38).

Chao *et. al.* (42) developed PDM to explain the growth and breakdown of the oxide film. This model was used to study the characteristics of the oxide film (43) and to predict the effect of alloy elements (44). Recently, a theory for the steady state properties of passive films formed on metals and alloys in aqueous solution was proposed by Macdonald (45) who predicted that the steady state thickness of the barrier film and the log of the steady state current will vary linearly with applied potential. In his model, the oxide film responsible for passivity contains high concentration of point defects and is covered by the porous, precipitated outer film. This outer layer, which may be gel-like amorphous phase, is not responsible for passivity.

There were other theories proposed in the literature (46-48) which do not significantly differ from the above theories. Most of these theories have concluded that local failure of the oxide film is the imperative process for pit initiation. It also seems probable that combinations of various aspects of the different theories may provide a more plausible explanation of pit initiation. Another type of pitting corrosion is distinguished by "etch pit" (49). The mechanism of this type of pit and application of this phenomenon has been developed for determining crystal structure and dislocation density on metal surfaces.

1.2 Passive Oxide Films of Stainless Steels

Passive oxide films are generally very thin: 50 Å or less for stainless steels. Therefore the study of passive films is very difficult and requires surface-sensitive

analytical techniques. Several measurement techniques have been applied for the study of oxide film (13). The experimental methods can be divided into *ex situ* and *in situ* spectroscopic techniques as shown in Table 1-I. In principle, *in situ* methods are more desirable because no alteration of the passive film during sample transfer can occur. However, *ex situ* methods (50-55), such as Auger electron spectroscopy (AES), x-ray photoelectron spectroscopy (XPS), secondary ion mass spectrometry (SIMS) and ion scattering spectroscopy (ISS), provide more direct and complete chemical information, and they can be applied to a wider range of problems of practical interest.

XPS and AES are essentially surface tools, as the electrons have little chance to escape if they originate deeper than 5 nm below the surface of a sample. They can be also applied to investigation of bulk samples but only if the surface is representative of the bulk composition. The Auger effect is a competitive process with fluorescence emission which will be discussed in Chapter 4. Fig. 1.2 shows the probabilities of the Auger process and of x-ray fluorescence emission as a function of atomic number (56). Therefore, AES is particularly valuable for analysis of light elements. ISS and SIMS use a beam of positive ions bombarding a solid sample, which removes atoms from the surface of a solid sample.

1.2.1 Chemical Composition of Passive Oxide Films

A study of the passive film on an iron-chromium alloy by XPS (50) showed that the chromium content of the film formed in deaerated 1 M H_2SO_4 solution increased by

Table 1-I. Spectroscopic methods for the characterization of passive films (13).

Ex situ	*In situ*
AES	ellipsometry
XPS	MRS
SIMS	Raman
ISS	EXAFS, XANES
GDS	Neutron activation
EELS	Mössbauer
SNMS	

AES, XPS, SIMS, ISS, and XANES = see text

GDS = glow discharge spectroscopy

EELS = electron energy loss spectroscopy

SNMS = sputtered neutrals mass spectroscopy

MRS = modulation reflection spectroscopy

EXAFS = extended x-ray absorption fine structure spectroscopy

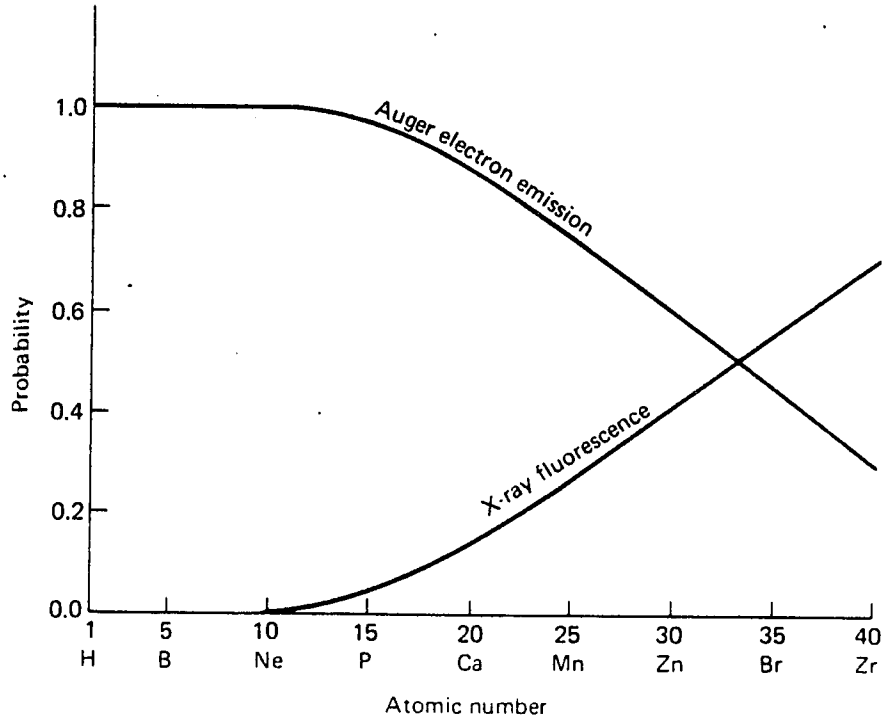

Fig. 1.2. Probability of Auger and of x-ray fluorescence emission vs. atomic number (56).

approximately 13 %. ISS was utilized by Frankenthal and Malm (51) who studied the composition of air-formed oxide films on a series of iron-chromium alloys. They measured the chromium content at the air/oxide interface. The Cr content was a little at the air/oxide interface, increased rapidly to a maximum, and then decreased to the level of chromium of the bulk steel at the oxide/metal interface. Okamoto *et. al.* (52) studied the composition of the passive film on Fe-18Cr-8Ni stainless steels using XPS and showed that the peak ratios Cr/Fe and Ni/Fe have maxima for the oxide film formed at 0.4 V (vs SCE) in sulfuric acid solution. The measurements by AES and SIMS also supported Cr enrichment in the film (53).

Olefjord and Elfstrom (54) investigated the passive film on stainless steels formed at the passive region in 0.1 M HCl + 0.4 M NaCl solution. They determined that 1) the passive film consisted of chromium oxide, 2) iron was preferentially dissolved during passivation, 3) nickel was present to a small extent, and 4) molybdenum enrichment was observed for a stainless steel containing 6% Mo. The Mo enrichment was supported by Barnes *et. al.* (55), who used AES to study the oxide film on 316 stainless steel (2% Mo) and found nearly 14% Mo content in the film.

The chloride content of the passive films on stainless steels polarized in chloride solution was analyzed using AES by several authors (50,57). In general they detected Cl^- presence in the passive films. Fromhold and Noh (58) theoretically examined the microscopic non-uniformity such as impurities, dislocations, grain boundaries and point

defects on current flow in passive layers. The results of the theoretical calculations showed that if microscopic regions surrounding Cl^- ions have lower activation energies for charge motion than the medium itself, the current would increase rapidly with Cl^- concentration in the passive film. They concluded that lower amount of Cl^- could lead to breakdown if there were grain boundaries and other easy diffusion paths in the passive film. Non-crystalline films can be more effective than crystalline films for maintaining passivity.

The characteristics of the passive film on stainless steels in 1 M $NaClO_4$ solution were investigated by photoelectrochemical techniques (59) supplemented with capacitance data obtained from impedance measurements. Photoelectrochemical laser imaging (PECLI) and photocurrent spectroscopy techniques were employed to obtain the optical gap which may be different from the band gap energy in the case of non-crystalline films and to obtain *in situ* images of the passive surfaces. They concluded that the passive film on 304 stainless steels was a highly doped n-type semiconductor amorphous in character.

1.2.2 Chromium Chemistry inside the Oxide Films

Cr enrichment on the passive film makes the film amorphous and thinner, which provides better corrosion resistance to stainless steels (58,59). The chemistry of Cr in the oxide film has been studied for many years and an *ex situ* XPS study (60) presented evidence for the presence of a Cr(VI) state in the oxide film. However, the study questioned the stability of a Cr(VI) state. Urretabizkaya *et al.* (61) used cyclic

voltammetry and potential jump techniques to investigate the role of Cr in the oxide film on pitting corrosion of stainless steel. They concluded that Cr(III) species oxidized to Cr(VI) to form soluble CrO_4^{2-} at a short anodization time. This soluble chromate formed at the outer oxide film was diffusing into the solution, but the chromate in the inner film was retained in the film. As the anodization time increased Cr(III) was transformed into another stable form, probably iron chromite ($FeCr_2O_4$) which exhibited the oxidation potential more positive than that of Cr(III).

Recently, *in situ* x-ray absorption near edge spectroscopy (XANES) was used to investigate the oxidation states of Cr in the oxide film on Fe-Cr and Al-Cr alloys (62,63) under electrochemical control. XANES technique can determine the chemical state of an element very accurately by comparing the shape of the absorption edge with standards of known valence. However, the technique is not surface-sensitive. To overcome this limitation, Davenport *et al.* (62) used an electrochemical cell in which the working electrode consisted of the thin alloy film ($\sim$ 20 - 40 Å) deposited on a tantalum layer ($\sim$ 100 Å) (to provide electrical contact) sputtered on Mylar plastic. The thin alloy film was then anodized in a borate buffer solution in order to form the oxide film. The presence of Cr(VI) was detected from XANES data in the transpassive region of the cyclic voltammogram and the reduction of Cr(VI) to Cr(III) was observed with the corresponding reduction curve (63).

1.3 Anodic Polarization Behavior of Stainless Steels in Chloride Solution

Polarization measurements are commonly used for investigation of a variety of corrosion phenomena for many metals and alloys (9). Such measurements can be used for studies of the reaction mechanism and the kinetics of corrosion processes and metal deposition. The potential-controlled methods (1) which are usually used to generate the curves can be summarized as: 1) scanning potential at a constant rate (potentiodynamic), 2) holding potential at a certain potential until a constant current is observed (stationary), and 3) changing the potential stepwise at a desirable rate (quasi-stationary). Changes in current density with potential are in general measured from the corrosion potential (open circuit potential E_{oc}) to a certain anodic potential higher than the pitting potential.

Typical polarization curves are shown in Fig. 1.3 for stainless steels in chloride environments (1). Curve (a) is usually seen in the case of stainless steels in neutral NaCl solution. The curve is clearly distinguished by two regions. In the region having very low, constant current density, the metal is protected by the thin passive film, so that no localized corrosion takes place, i.e., a passive region. However, some careful measurements often show tiny current peaks in the region that indicate the event of pit initiation and repassivation processes (4,15-16). Frankel (16) observed a short-duration current transient due to metastable pitting in the passive region of a Type 302 stainless steel in a 0.1 N chloride solution and discussed pit stability in terms of potential drop and pH inside pits. The transients associated with pitting will be extensively discussed in Chapter 2.

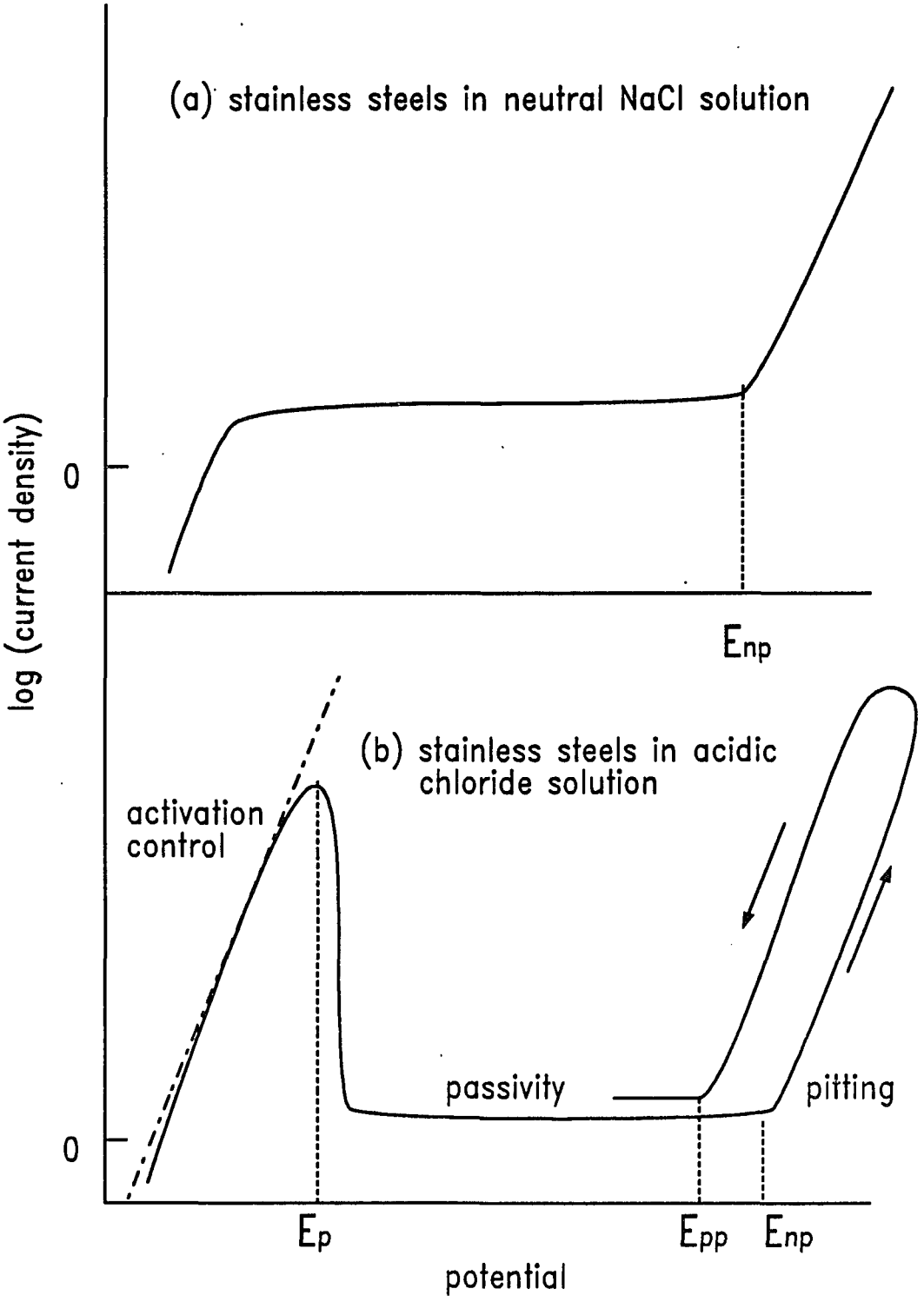

Fig. 1.3. Schematic polarization curves for stainless steels in chloride environments (1,4).

In the region that showed rapid increase of current density, breakdown of the film takes place and pits start growing on the metal surface. The pitting potential or critical potential, E_{np}, normally expresses the potential at which pits initiate and continue to grow. The pitting potential is one of the most important parameters for estimating the susceptibility of metals or alloys to pitting corrosion (65) in a given environment. This potential varies with metal, solution concentration, pH, surface morphology, heat treatment, cell geometry and measurement conditions (40,66).

Smialowska (67) determined the pitting potential of different materials in 3% NaCl solution from the corresponding polarization curves and showed that a Type 316 stainless steel had the highest pitting potential among nickel, Type 430, 304 and 316 stainless steels. Mild steel did not show a passive region and was attacked by uniform corrosion.

A reverse scan shown in Fig. 1.3 (b) reveals another characteristic potential, the protection potential or repassivation potential E_{pp} which was identified by Pourbaix *et al.* (64), as the potential below which no pitting occurs and above which pits that already nucleated, can grow. The anodic polarization curve of stainless steels in Fig. 1.3 (b) can normally be seen in acidic chloride solutions. Uniform dissolution of the metal occurs in the active region. The dissolution process in this region is under activation control which is expressed by the Butler-Volmer equations (4,68,69) for the anodic and cathodic current densities:

$$i = i_a - i_c = i_o \left[\exp\frac{(1-\beta)zF\eta}{RT} - \exp\frac{-\beta zF\eta}{RT}\right] \qquad [1\text{-}3]$$

where i_a = anodic current density,

i_c = cathodic current density,

i_0 = exchange current density,

η = overpotential (= E - E_e, where E_e is an equilibrium potential),

β = symmetry factor (normally ~ 0.5),

z = charge,

F = Faraday constant (C),

R = gas constant (J/mole/K), and

T = absolute temperature (K).

This Butler-Volmer equation is a fundamental equation for electrodic kinetics, which shows how the current density across a metal/solution interface depends on the difference in the overpotential. The equation is simplified by either high field (E > E_e), i.e., η is large, or low field (E ≈ E_e), i.e., $\eta \to 0$, approximations (68,69). The high field approximation yields

$$i \approx i_o \exp\frac{(1-\beta)zF\eta}{RT} \qquad [1\text{-}4]$$

or, as given by Tafel (70),

$$\eta = -\frac{2.303RT}{(1-\beta)zF}\log i_o + \frac{2.303RT}{(1-\beta)zF}\log i \qquad [1\text{-}5]$$

Therefore a plot of log i against potential produces a straight line as shown in the active

region of curve (b) with a slope of $(1-\beta)zF/2.303RT$. The low field approximation eliminates the exponential terms and gives:

$$i \approx \frac{i_o zF\eta}{RT} \qquad [1\text{-}6]$$

Thus, electrodic reactions across interfaces exhibit simple ohmic behavior under low-field conditions.

As the potential is made more positive, the dissolution current increases, obeying the linear Tafel behavior (68,69). However, at a certain potential, i.e, the passivating potential E_p shown in the curve (b), the curve starts decreasing rapidly with potential. The metal is apparently protected by the passive oxide or hydroxide film from dissolution in the passive region.

1.4 Pit Propagation - Theoretical View

Fig. 1.4 shows a simplified schematic diagram of the electrochemical pitting process. Several processes occur in a pit during pit propagation, including metal dissolution, mass transport, and chemical reactions such as hydrolysis and metal-anion complexation. As pits initiate, rapid anodic dissolution of metals takes place at pitting sites and the corresponding cathodic reactions such as oxygen reduction ($O_2 + 2H_2O + 4e^- = 4OH^-$) and hydrogen evolution ($2H^+ + 2e^- = H_2$) occur at the passive surfaces adjacent to pitting sites. Metal ions accumulate in the occluded regions of the growing pits. Diffusion, migration and chemical reactions among the species will then establish

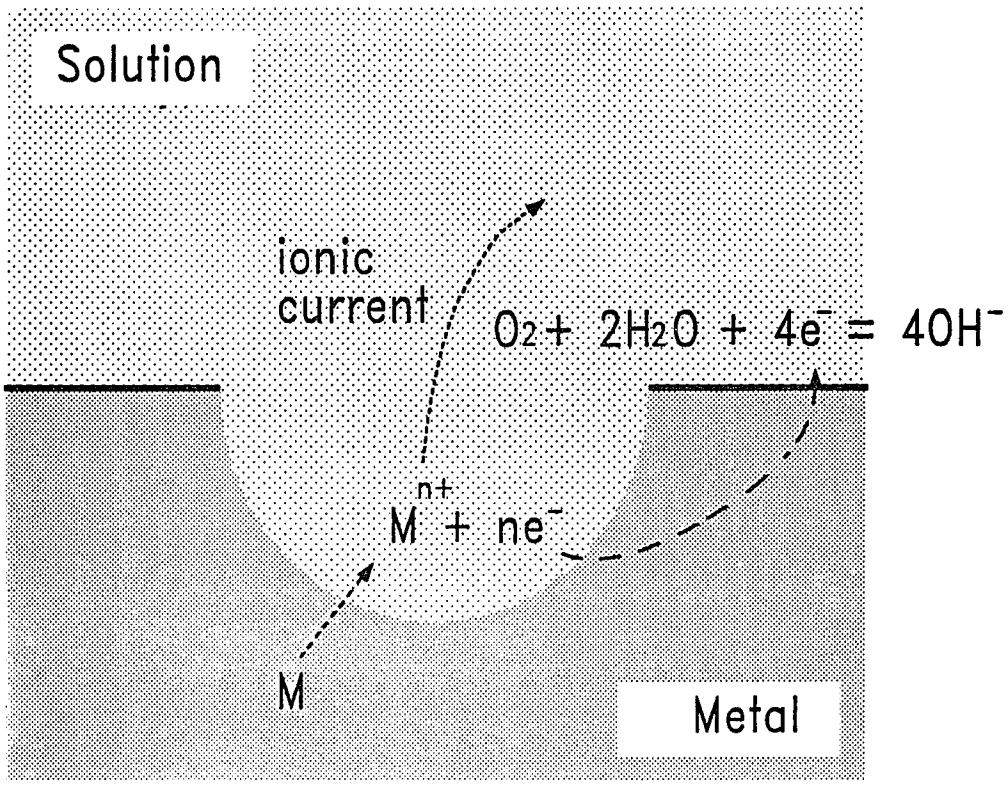

Fig. 1.4. A schematic diagram of electrochemical pitting processes.

the necessary conditions inside a pit for pit propagation. Whether this pit will grow or repassivate depends on several factors which may be quantified by understanding the chemical properties of the solution within the pit. The properties of the solution within pits during pit propagation can be illustrated by using the following model.

1.4.1 Basic Equations for a One-dimensional Pit Model

The laws governing mass transport in solution have been well established in the literature (5). The Nernst-Plank equation (69) in infinite dilute solution is defined by the following equation:

$$J_j = - D_j \nabla C_j - \frac{z_j F}{RT} D_j C_j \nabla \phi + C_j v \qquad [1\text{-}7]$$

where J_j = flux (mole/sec/cm^2),

D_j = diffusion coefficient (cm^2/sec),

C_j = concentration (mole/cm^3),

z_j = charge,

v = convection velocity (cm/sec), and

ϕ = potential (V).

The first term on the right side of the equation provides for the diffusion flux due to concentration gradients, the second for the migration flux of charged particles under a potential field and the last term for the convection flux. From Fig. 1.1, for linear mass transfer where convection is absent, equation [1-7] can be simplified at a given distance x from a metal/solution interface:

$$J_j(x) = -D_j\frac{\partial C_j}{\partial x} - u_j C_j\frac{\partial \phi}{\partial x} \qquad [1\text{-}8]$$

where u_j = mobility ($|z_j| FD_j/RT$)

Also the relationship between current and flux is:

$$-J_j = \frac{I_j}{z_j FA} \qquad [1\text{-}9]$$

where I_j is current due to the flux of the jth element and A is the cross-sectional area. At quasi-steady state dissolution inside a pit, the concentration will be time independent:

$$\frac{\partial C_j}{\partial t} = -\frac{\partial J_j}{\partial x} + R_j = 0 \qquad [1\text{-}10]$$

where R_j refers to all chemical reactions that occur in the pit solution. Charge neutrality:

$$\sum_{j=1}^{m} z_j C_j = 0 \qquad [1\text{-}11]$$

is generally assumed in theoretical calculations.

The chemistry of the pit solution therefore can be studied through theoretical calculations using the above equations with necessary input data and considering chemical reactions among reactants if the solution is homogeneous (5).

1.4.2 Theoretical Models of Pit Solution

Since Galvele (38-40) established a simplified model for the processes occurring in pit solutions, a number of theoretical models (71-82) have been developed to understand the physical and chemical nature of the solution inside stable pits and crevices, which might be considered as macroscopic pits and have environments similar

to growing pits. These models, in general, give detailed information for the solution inside pits or crevices and have been used to investigate the roles of each element in alloys and to predict some of the important characteristics of localized corrosion such as critical Cl^- concentrations and pH, the critical size of cavities for the propagation of pits or crevices, induction time and the pitting potential.

Ateya and Pickering (78) studied mass transfer in aqueous solutions on repassivation of activated surfaces and the stability of protective films on metals. They used a model similar to Galvele (38), but considered only steady state dissolution of metals at the bottom of the pit. The model predicted that oxide films are, in general, more stable when nonaggressive anions are present than when chloride ion is present and that the concentration of polyvalent anions such as CrO_4^{2-} and MoO_4^{2-} in the diffusion layer inside pits is higher than that of monovalent anions Cl^-. Sharland and co-workers (73,74) developed a finite-element model of the propagation of corrosion pits and crevices. The model calculations applied to pitting corrosion of carbon steels in chloride solutions and demonstrated good agreement with the experimental results of Beaver and Thompson (80). Watson and Postlethwaite (79) applied a numerical simulation for crevice solutions of stainless steels and nickel alloys in chloride solutions. The numerical simulation results suggest that there is a distinct delineation between a metal exhibiting passivity or active crevice corrosion for a given crevice depth or average crevice gap, and predicted the induction times (incubation periods) of crevice corrosion of the alloys based on a critical pH for the crevice solution.

Tester and Isaacs (81) introduced activities and viscosities to correct the concentrations and diffusivities for highly concentrated solutions and constructed mass transfer models for the observed current transients and quasi-steady state periods of dissolution. McCafferty used activity coefficients to calculate the equilibrium conditions within a localized corrosion cell of iron (82). Alkire *et al.* (83) studied the role of conductivity variations within artificial pits experimentally and theoretically for copper/copper sulfate systems. They concluded that increasing the conductivity of the solution inside pits initiated auto-acceleration of the dissolution rate.

The theoretical models use infinite dilution theory (68) as a basic assumption and also additional assumptions that simplify the calculations. The additional assumptions used in the literature are summarized:

1) electroneutrality in the pit solution
2) instantaneous chemical reactions
3) no convection inside a pit
4) transport only by diffusion of metal ions (anions act as a supporting electrolyte) (38-40,76,78)
5) inert side wall (38-40,78) or active side wall (73,74,79)
6) steady state dissolution (38-40,76-78), and
7) solution concentration proportional to the concentration of the element in the alloy (79)

In addition to these assumptions, proper boundary conditions and accurate data for diffusion coefficients and equilibrium constants are necessary to complete the mathematical calculations. However, it is often difficult to find diffusion coefficients for ions in binary or tertiary solutions. The assumptions and the approximations made in the calculations of the theoretical models might not be valid for the corrosion systems being considered and the correct input data for calculations may not be found. Therefore it is highly desirable to carry out experimental measurements to study the properties of solutions in such a system in order to verify model calculations.

1.5 Pit Propagation - Experimental View

A number of studies concerning the experimental measurements of pit or crevice solutions in various corrosion systems have appeared in the literature (6,84-102). The experimental methods for study of pitting corrosion can be divided into the following groups (84):

1) direct *in situ* measurements - use of microelectrodes,
2) semi-direct *ex situ* chemical analysis of the solution obtained by solution extraction techniques,
3) use of artificial pits and occluded cells, and
4) simulation of the chemistry of localized corrosion, i.e., use of highly concentrated acidic metal chloride solutions.

1.5.1 Direct *In Situ* Measurements

A majority of the measurements use microelectrode probes (85-90) having tip diameters from a few micrometers to a hundred micrometers. However the size of the tips may be still large relative to the size of actual pits. The critical concern of this approach is therefore the possibility of perturbing the environment in the pit with the probe and of blocking the diffusion path of metal ions. These microelectrode techniques are, in general, not able to measure metal contents in the pit solution.

Techniques using Ag/AgCl and tungsten needle microelectrodes were recently applied by Ives and Luo (89) to analyze chloride concentration and pH of the solution within a "pencil-type" artificial pit formed by dissolution of a nickel wire in chloride environments. The geometry and dimension of the tips employed are shown in Fig. 1.5. The cross-section of the Ag/AgCl probe was 3% of the pit cross-sectional area and of the pH probe (tungsten needle) was 0.4%. These were considered insufficient to interfere significantly with the transport processes. They have reported *in situ* measurements of the concentration of chloride ions, potential and pH as a function of depth within the pit and established the conditions necessary for steady pit growth during pitting corrosion. They demonstrated that micro-electrodes are sensitive enough to characterize the variation of electrolyte composition within a small pit and have high stability with good spatial resolution. The local conductivity of the solution inside a pit increased exponentially with the pit depth, which indicates the aggressiveness of the pit solution. They concluded that the steady development of a pit is due to both the increasing aggressiveness of the pit solution and the IR drop inside a pit.

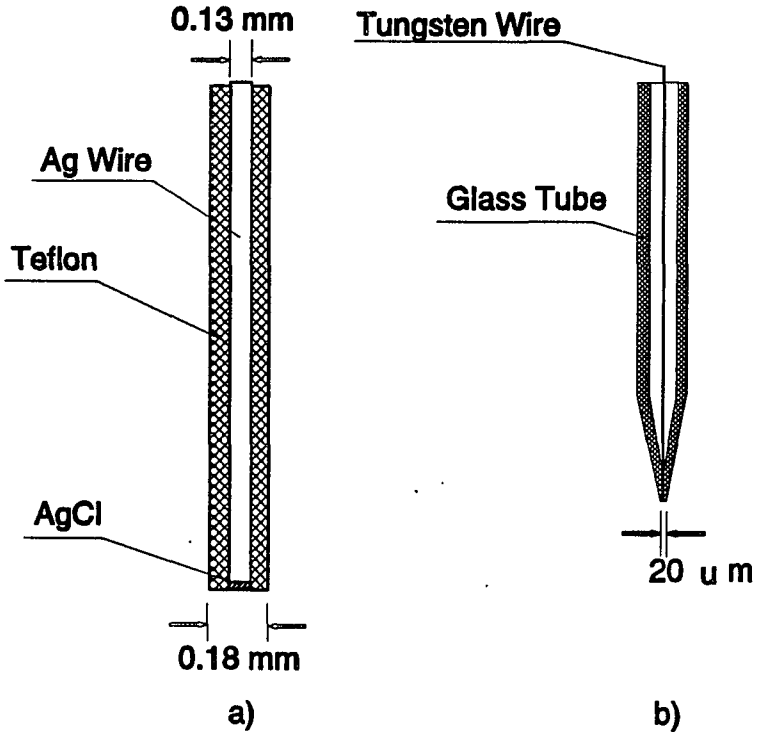

Fig. 1.5. Schematic diagram of microelectrodes: (a) Ag/AgCl electrode, and (b) pH probe (89).

1.5.2 Semi-direct *Ex Situ* Methods

The techniques described in this section involve sampling solution from the pit or cavity and analyzing for the various species of interest. The analysis of the solution may be made at the extraction sites (90,91), in which miniature pH and Ag/AgCl electrodes can be used to measure pH and Cl^- concentration, respectively. But, again, this method cannot analyze metal concentrations. The usual analytical method is that small volumes of solutions are removed from pits or crevices and that chemical analysis is applied to analyze them at a later stage.

Lott and Alkire (92) obtained time sequence information for variation of the relative metal contents in the solutions extracted from the crevices developed by dissolution of stainless steels in a 0.1 N NaCl solution. They separated the crevice solution by draining the bulk electrolyte and diluted it with distilled water. Inductively coupled plasma spectroscopy (ICP) was used to analyze iron, nickel and chromium concentrations in the solution. Nash and Kelly (93) used ion chromatography (IC) to obtain the metal ion concentrations of the solution extracted from the artificial pit dissolved by stainless steel wires in 1 M HCl solution. Simultaneous determination of all the metal ions in a sample could be made and the analytical results showed the presence of Fe^{3+} ions, that might be formed by oxidation during the processes of extraction and dilution, and the preferential dissolution of Cr and Mn from the alloys.

Castle and Qiu (94) applied inductively coupled plasma-source mass spectroscopy (ICP-MS) and XPS to study ion selectivity during passivation of stainless steels in 0.1 M sulfuric acid solution. They introduced the selectivity factor S to characterize the selective dissolution of ions from the steels and the enrichment factor *f* to characterize the selective enrichment of ions in the passive films. In contrast to Nash and Kelly's result (93), they found the selective dissolution of Ni at the early stage of dissolution and the selective dissolution of Fe at the later stage. As a consequence of this selective dissolution, they also found the selective enrichment of Cr and Mo in the passive films.

Tsuru *et al.* (95) used atomic absorption spectroscopy (AAS) for analysis of metal ions and potentiometric titration for analysis of chloride ion in the solution confined in an occluded cell. They estimated apparent transport numbers of chloride anions and metal cations in an occluded cell from chemical analysis of solutions obtained by dissolving a stainless steel and Fe-Cr alloy in a chloride solution, which were different from those calculated from known mobility data and deduced the presence of the metal-chloride complex ion $FeCl^+$. The complex formation between iron and chloride ions is also suggested by X-ray absorption spectroscopy (EXAFS and XANES) study of iron(II) chloride solutions between 0.4 M and 4.0 M, having various Fe/Cl ratios (0.1 ~ 0.5) (96). The solutions having different Fe/Cr ratios were prepared by using concentrated HCl solutions.

1.5.3 Artificial Pit, Crevice and Occluded Cells

A wide variety of artificial cavities have been developed to simplify the problems of solution analysis and electrochemical measurements. This has included the development of occluded cells (95,97), shown in Fig. 1.6 (a), which simulate localized corrosion environments by restricting mass transport from dissolving sites to bulk solutions. A "pencil-type" artificial pit, shown in Fig. 1.6 (b), in which metal wire is mounted in epoxy is frequently used for the study of pitting and crevice corrosion because of well-defined geometric conditions (89). The contribution which these studies of artificial pits have made to understanding of localized corrosion processes has been considerable, even though it is important to be aware that care must be taken in applying the results.

1.5.4 Simulation of the Chemistry of Localized Corrosion

This approach uses solutions of highly concentrated metal chlorides, concentrated hydrochloric acids or mixture of both that simulate the environments inside pits and crevices. The results from this technique ignore mass transport, but they can provide information on the pH in pit solutions and the steady state potential or current of metal in these environments. Sathler *et al.* (98) carried out a detailed investigation of the electrochemical behavior of iron in ferrous chloride solution. They measured the potential and pH when iron was immersed in a deaerated solution of saturated $FeCl_2$. The pH and potential in the saturated solution was found to be 3.8 and -0.569 V (vs SCE), respectively.

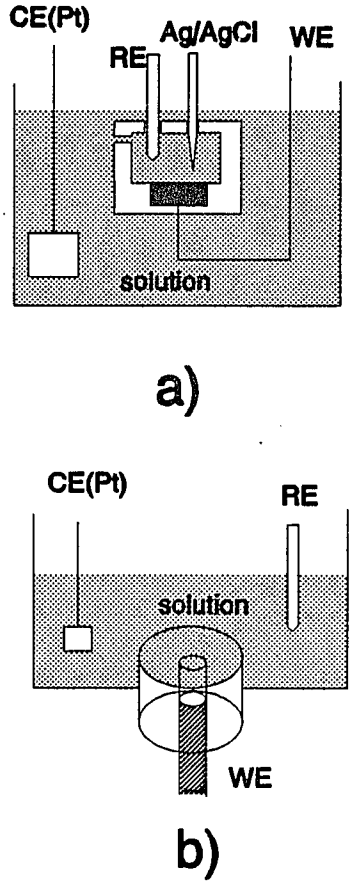

Fig. 1.6. Artificial pits: a) occluded cell (95), and b) "pencil-type" one-dimensional pit (84).

Hakkarainen (6) studied anodic behavior of stainless steels in simulated pit solution obtained by dissolution of stainless steels in 10 M HCl until the amount of dissolved metal ions was equivalent to the amount of chloride ions in the solution. He found that above the pitting potential, there was a critical minimum concentration below which an abrupt change from a dissolution state to a passive state was observed. The effects of chloride ions and metal chlorides ($FeCl_2$, $NiCl_2$ and $CrCl_3$) on pH and the pitting potential will be discussed in the next section.

Most of the experimental studies other than microelectrode measurements were, however, carried out either by *ex situ* chemical analyses of solutions extracted by various techniques or by indirect electrochemical measurements. The results therefore may not correctly represents the nature of solutions, especially for metal ionic concentration, confined within stable pits and crevices. It should be also emphasized that the results by chemical and electrochemical analysis only provide average information on pit solutions. Therefore it is necessary to develop *in situ* microanalytical methods to analyze the local compositions of the solution inside pits and crevices. The features of x-ray fluorescence microscopy (XRM) (99,100), which will be described in Chapter 4 and 5, meet certain requirements for the non-destructive microanalysis of the solution within pits without interfering with the electrochemical corrosion processes and for obtaining spacial resolution on the micron scale.

1.6 The Effects of Chloride Concentration on pH and the Pitting Potential

Passive oxide films on stainless steels are certainly responsible for the protection of stainless steels from corrosion. However, once local break down of the film occurs, the metals are attacked by pitting corrosion. As a pit initiates, a sudden potential change at metal/solution interface leads to current flow from the pitting site to the surrounding passive surface (101). The capacitive interface is initially discharged and then recharged due to electrochemical Faradaic reaction which consist of metal dissolution as the anodic reaction and possibly oxygen reduction and hydrogen evolution as the cathodic reactions. Once metal dissolution occurs in a pitting site, the solution inside the pit becomes highly concentrated and the anodic reaction can be catalyzed by this aggressive pit solution in the presence of chloride ions. The potential change inside a pit may bring the potential to the active region and the pH is shifted to the acidic region by hydrolysis reactions. The pH inside pits decreases further as metal chloride accumulates.

The effect of metal chlorides on pH has been studied and the relationship has been quantitatively established by a number of authors in the literature (40,64,67,79,102-104). Galvele (40) calculated and analyzed the variation of the pitting potential as a function of chloride concentration, concluding with the following equation:

$$E_{np} = E^{o} - B\log[Cl^{-}] \qquad [1\text{-}12]$$

where B = 0.0592 V at room temperature, and

E^{o} = pitting potential at $[Cl^{-}]$ = 1 M.

He explained that this equation is only valid for dilute solutions and needs to be corrected for ohmic drops outside pits to accommodate other experimental results on the pitting

potential.

Batista *et al.* (66) investigated the polarization behavior of INCOLOY 800 and Type 304 stainless steel in synthetic metal chloride ion solutions within an occluded cell and found that the anodic behavior of the alloys depends on the chloride concentration and pH of the solution. They suggested that the use of an acidic NaCl solution would be desirable to investigate the propagation process of localized corrosion. The following equation was formulated by Watson and Postlethwaite (79) using data in the literature (102) to model metal chlorides effect on pH:

$$pH = pH^{o} - 0.33[CrCl_3] - 0.22([FeCl_2] + [NiCl_2]) \qquad [1\text{-}13]$$

The pH variation of metal chloride solution is probably due to high activity coefficients of hydrogen ion in solution and production of hydrogen ions by formation of hydroxy-chloro-metal complexes (95,97).

1.7 Salt Layer on Metal Surfaces during Pit Propagation

Since Muller (105) in 1933 reported the existence of salt films during the passivation of iron and nickel, a number of investigations have appeared in the literature (106-123). Strehblow and co-workers (109,110), Beck (111) and Isaacs (112) provided convincing evidence that the processes of pit propagation are closely related to the formation of salt layers at the pit bottom. During pit propagation, the rate of dissolution is controlled by diffusion of metal ions within an occluded area of pitting corrosion to the bulk electrolyte. Potentiostatic or galvanostatic dissolution using one-dimensional

artificial pits has been widely used to study the properties of the salt films and mass transport during localized corrosion (81,89,110-113,117,119).

1.7.1 The Role of Salt Layer during Metal Dissolution

A typical current transient, shown in Fig. 1.7, for anodic dissolution of a Type 304 stainless steel wire in chloride solution was presented by Tester and Isaacs (81). The current showed a current maximum and a region of quasi-steady state current. A sudden increase in potential above the pitting potential causes loss of passivity and initiates dissolution of the metal, which results in a current increase. However, dissolution of the surface is a microscopic phenomenon and a number of pits are nucleating and growing on the surface simultaneously. The current increases continuously until supersaturation on the whole surface area is reached at a time τ. Then the salt layer precipitates on the surface providing resistance across the interface. This salt layer displays a self-regulating effect in balancing the layer current with the diffusion flux in solution (112). Finally, a quasi-steady state of dissolution is established. At this stage, decrease in current is inversely proportional to pit depth.

A rotating disc electrode was used to study the presence of the salt layer and diffusion limited mass transport phenomenon (113) for dissolution of iron in chloride solution. The results indicate that under limiting current conditions, the anode was covered by a thin layer of $FeCl_2$. Later, a one-dimensional diffusion cell for iron wire in chloride solution was galvanostatically investigated to observe the presence of the salt

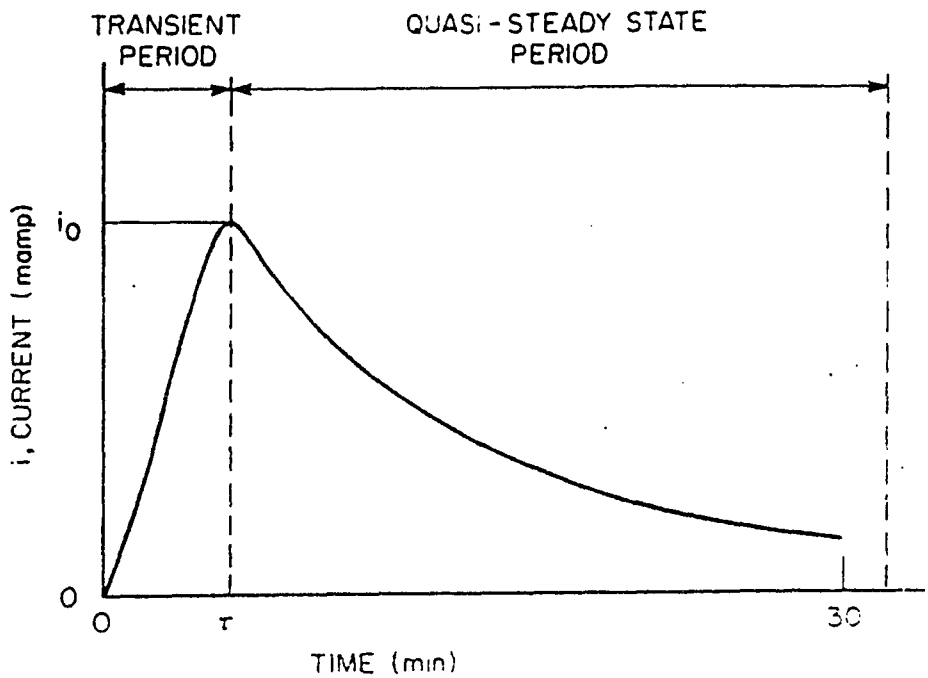

Fig. 1.7. A typical current transient observed during dissolution of a stainless steel wire in chloride solutions (81).

layer (114). The conclusion suggested that supersaturation is necessary to induce salt precipitation.

1.7.2 The Properties of Salt Layers

Alkire *et al.* (117) presented a mathematical model to describe the processes whereby the transient appearance of a salt film occurs during the initial stages of corrosion of a bare metal surface. The model calculation predicted supersaturation prior to precipitation of a salt layer and dissolution of the salt film to repassivate the metal surface. They suggested that the chloride salt film on a titanium surface would be 20 - 100 Å thick and that it would disappear within the time of 10^{-5} - 10^{-3} sec after the generation of oxide-free surface. Rosenfeld *et al.* (118) investigated the pitting corrosion of stainless steel in acidic chloride solutions. They were able to show that the corrosion rates inside pits (50 - 60 mA/cm^2) are independent of the potential and suggested that the repassivation potential of a pit does not correspond to the metal potential at the pit bottom but is highly variable and cannot be used to rank metals according to their pitting resistance.

Salt layers on metal surfaces were not observed directly until 1982 when Beck (119) first made microscopic observation of a crystalline salt on a metal surface when iron dissolved in HCl, $HClO_4$ and H_2SO_4 solutions. The crystalline salt was present only transiently, disappearing soon after its formation. Beck concluded that the $FeCl_2$ salt layer precipitates on the surface in 6 N HCl and ferrous salt layers form on iron, in

1 N or higher concentration of $HClO_4$ and H_2SO_4 solutions at potentials and current densities greater than threshold values determined by mass transport conditions. Below the passivation potential E_p a salt film remains and above it an oxide film subsequently forms underneath the salt layer causing passivation. He also suggested that formation and dissolution of salt layers coupled to change in pH under the salt layers due to mass transport could explain oscillatory phenomena (122) during passivation of iron.

Measurements of AC impedance and current/potential transient (120) were employed to determine the ohmic potential drop across chloride salt films, the electric conductivities of the films and the film thickness. The results showed that the ohmic potential drop increases with decreasing diffusion limited current density and with potential. The critical potential for formation of a salt film was found to be -0.19 and -0.08 V (vs SCE) for a Type 302 stainless steel and nickel, respectively. The specific electric conductivity of the films is $\sim 1.4 \times 10^{-5}$ and 4.4×10^{-5} Scm^{-1} for SS 302 and nickel, respectively, where S is Ω^{-1}. The salt film was very thin compared to the pit depth (> 1.5 % at an applied potential of 1.2 V) and linearly increased with potential and chloride concentrations.

Recently, Danielson (121) studied the properties of salt films on nickel in 0.5 N HCl solution using a one-dimensional artificial pit, high frequency impedance measurements, and potentiostatic and potential step experiments. The calculated value of field strengths for the salt layer formed on a nickel surface was 400 V/cm indicating

that a low field transport process was operative, and the estimated thickness of the salt films was in the range of 0 - 10 μm depending on the applied potential and pit depth. He concluded following Beck's results (119) that the potential drop across the salt layers results in a shift in pH in the basic direction at the metal/salt interface, which may cause formation of passive oxide film underneath the salt layer. A study by Clerc and Landolt (123) supports Danielson's conclusion, showing that 10 nm thick oxide layer was present underneath the 200 nm thick salt layer on nickel in LiCl solution.

1.8 The Present Thesis

The present thesis investigates complicated electrochemical phenomena occurring during localized (pitting or crevice) corrosion of stainless steels in chloride environments.

1.8.1 Structure of the Thesis

Chapter 1 presents an introductory view of pitting corrosion of stainless steels in the presence of chloride solution by reviewing literature in this subject and raises some problems with existing experimental and theoretical methods to study various aspects of pitting corrosion. Since the present work mainly focuses on chemistry inside pits and on localized corrosion transients, a larger portion of this chapter discusses investigations of pit solutions and salt layers. Chapter 2 then focuses on localized corrosion transients including: historical background, the properties of surface impedances and their effects on measurements of the transients. Chapter 3 is the brief summary of Chapter 1 and 2, which concludes the literature survey on pitting corrosion. Chapter 4 presents

fundamental principles and applications of x-ray fluorescence spectroscopy (XRF) which is one of the main experimental techniques employed in the present work.

Chapter 5 extensively describes the experimental procedures carried out in this work. Chapter 6 presents and analyzes the experimental results obtained from x-ray fluorescence microprobe measurements and optical microscope observation to investigate the chemistry of pit solutions and salt layers. The quantitative analytical results of x-ray fluorescence microscopy (XRM) are compared with the data available from the literature. Chapter 7 presents and analyzes the results of the investigations concerning localized corrosion transients. Finally, Chapter 8 summarizes all the work done in the present research project and suggests further work necessary to develop a better understanding of pitting corrosion.

1.8.2 Motivation and Direction of the Thesis

The present work pursues two aspects of pitting corrosion: the chemistry inside pits and localized corrosion transients. The first main objective is to understand the chemistry of pit solutions during dissolution of metals. Conventional experimental methods have only provided limited information to this subject, while theoretical models offer a full description of chemistry inside pits. However, uncertainty in the input parameters required for model calculations still exists and, for stainless steels which are the main materials in the present investigation, uncertainty increases. Therefore results from model calculations for stainless steel/chloride systems may not be adequate for

understanding the solution chemistry occurring inside pits. Development of new experimental methods that can verify the results from model calculations are required.

Microscopic techniques such as x-ray fluorescence microscopy (XRM), optical microscopy and scanning electron microscopy (SEM) are employed to study an artificial pit. XRM has been recently available (99) and widely used to analyze local compositions of various samples in the gas, liquid or solid phase, and to determine impurity or trace elements quantitatively down to 10^{-15} gram. This is possible due to developments in the theory and the availability of synchrotron sources with x-ray intensities orders of magnitude greater than conventional rotating anode x-ray sources. Optical microscopy has been used in many areas of science for a number of years and a new technology employing a video camera interfaced with a computer provides the capability to digitally store and to enhance the quality of the images (185). Signal transients are investigated using EIS measurements and pulse measurements.

A new geometry for a one-dimensional artificial pit is designed to perform x-ray microanalysis and optical microscopic observations of the cavity forming during metal dissolution. Microanalysis of *in situ* x-ray fluorescence measurements are carried out to measure the concentration gradients and diffusion coefficients of metal ionic species within a simulated pit during dissolution of stainless steel in an acidic chloride (or bromide) solution. The insoluble corrosion products in the dissolved area, the compositions of which differ by their shape and locations, are also observed and analyzed

by optical microscopy, scanning electron microscopy (SEM) and energy-dispersive spectroscopy (EDS).

The chemical properties of salt layers observed during metal dissolution are investigated using *in situ* video optical microscopy (VOM), x-ray fluorescence microscopy (XRM) and electrochemical measurements. The thickness of the salt layer is microscopically determined as a function of applied potential and of pit depth. The time evolution of forming the salt layer is compared with the corresponding current transients.

The second aspect is to understand localized corrosion transients in corrosion cells. Localized corrosion transients are closely related to the corrosion processes taking place locally on metal/solution interfaces. However the true transients are not easily detected by electronic instruments. They are normally delayed and altered by surrounding passive surface and solution. This effect will be extensively discussed in chapter 2.

A main idea dealing with this subject is that corrosion cells and transmission lines can be represented by the corresponding equivalent electrical circuits.
A simple transmission line model using resistive (R) and capacitive (C) elements has been developed to understand transient behavior along a one-dimensional corrosion cell. The present work investigates the AC impedance (Z) of the metal/solution interface which

may not be simply interpreted by ordinary ideal circuit elements. A modified model for a one-dimensional transmission line is presented. Combination of the model and Fourier analysis of transients can yield a method that can locate a site of localized corrosion along a transmission line and recover the original shape of early stage localized corrosion transients. This method is tested by applying a known shape of transients, measuring the responses and comparing them with model calculations. It is believed that this study can contribute to the study of early stages of pitting corrosion since unaltered localized corrosion transients provide direct information on the kinetics and mechanisms of localized corrosion processes.

Chapter 2

LOCALIZED CORROSION TRANSIENTS

Potential or current transients correlated to localized corrosion were known since Iverson (124) measured the sporadic potential fluctuations of corroding metals. He measured potential fluctuations between a platinum electrode and various metal electrodes, including aluminum, aluminum alloys, magnesium, iron, mild steel and zinc, in a 0.1 % NaCl solution. In sodium nitrate solutions which act as a corrosion inhibitor (125), no fluctuations were observed. It was postulated that the potential fluctuations are caused by minute transient changes in the electrical charge on the electrode produced as a result of cathodic and anodic reactions during the corrosion process and that the imbalance of charge may also be due to transient changes in cathodic or anodic areas. He concluded that investigations of potential fluctuations appear to offer promise for the detection and study of the corrosion process and for the study of corrosion inhibitors.

More quantitative analysis of the transients has been later carried out by several authors (15,126-128,196-200). Blanc *et al.* (126) studied electrochemical noise and reported the results of experiments using autocorrelation and correlation functions. Epelboin *et al.* (127) presented the results of spectral densities derived from voltage fluctuations for both redox systems and corroding electrodes. They observed relatively high levels of noise for a corroding iron electrode which were shown to be much greater

than the thermal noise generated by the electrode impedance. It was reported that on imposing an anodic current, the low frequency noise decreased, and as hydrogen evolution also decreases with increasing anodic potential, it was concluded that the random fluctuations could be linked to gaseous hydrogen evolution.

A detailed analysis of the potential fluctuations of corroding electrodes was presented by Searson and Dawson (128) who suggested that the form of the noise spectra may give information on the nature of attack and differentiate between uniform and localized corrosion. They found some evidence that the standard deviation of the noise may be proportional to the dissolution rate. Bertocci (15,198,199) presented a stochastic model for the current fluctuations of electrochemical corrosion systems and reproduced experimental data using the model calculations. He pointed out that electrochemical noise or signal fluctuations might be associated with microscopic and fast corrosion processes occurring on metal surfaces.

2.1 The Current or Potential Transients Associated with Pit Initiation and Repassivation

Recently attention has been on single fluctuation of the potential fluctuations (4,10,16,101,129). Isaacs and Ishikawa (101) presented potential transients related to the processes of pit initiation and repassivation of stainless steels in a NaCl solution. They interpreted the potential transients and current flowing from localized corrosion sites (LCS) by comparing them with calculated results obtained from the equivalent

circuit that represented a capacitive passive surface and a resistive localized corrosion site. Magaino *et al.* (129) observed the different potential transient and power spectral density (PSD) between pitting and crevice corrosion on stainless steels in NaCl solutions containing NaClO.

Fig. 2.1 (a) and (b) illustrate the potential fluctuations of a Type 304 stainless steel in a mixture of NaCl and NaClO solution at E_{oc}. It was found that initiation and repassivation of micropits took place with potential fluctuations in the form of a rapid drop followed by a slow rise. When crevice corrosion was proceeding, potential fluctuations in the form of rapid rise followed by slow drop were observed. However, they also presented another potential transients obtained for a long time period. It showed that E_{oc} initially increases slowly when no corrosion takes place, but decreases rapidly when crevice corrosion occurs, and lingers at this lowered potential with some small potential fluctuation for the rest of the measurement period. Fig. 2.1 (b) is not the typical transient directly associated with the electrochemical processes of crevice corrosion, but may be related to gas evolution inside crevices. This argument was supported by Acoustic Emission (AE) signals and optical microscope observation which were subsequently monitored with potential transients. On the other hand, the potential transients of Fig. 2.1 (a) are directly correlated with the corrosion processes taking place on metal surfaces, i.e., pit initiation and repassivation.

Frankel discussed pit stability of stainless steels in a 0.1 M NaCl solution using

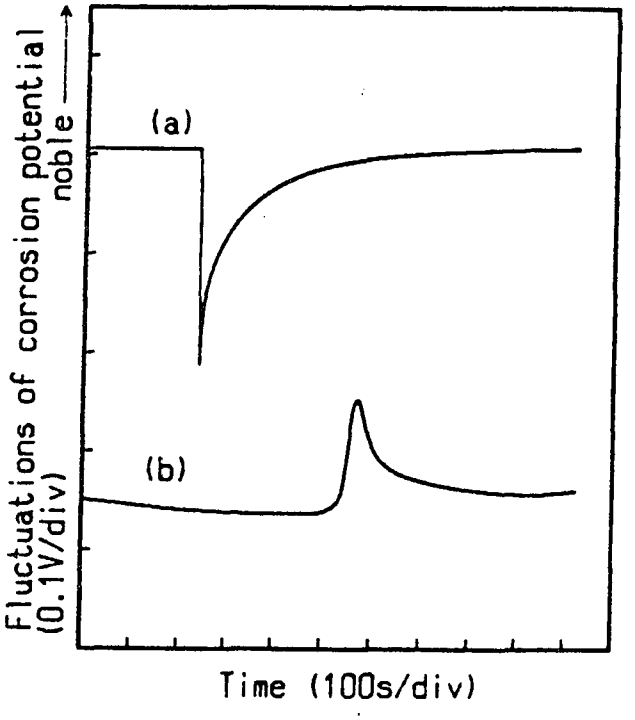

Fig. 2.1. Typical potential fluctuations observed (a) when micropits were formed, and (b) when crevice corrosion was proceeding (129).

a term "metastable pit" which symbolizes the non-propagating pits observed below the pitting potential E_{np}, and its current transient (16). The current transients shown in Fig. 2.2 associated with the processes of pit initiation and repassivation were recorded under potentiostatic control. He suggested that pits could be stabilized by the ohmic potential drop inside the pits which originated either from the precipitation of a salt film or from the oxide film remaining over the metastable pit. Stewart (4) also studied anodic current transients related to early stages of pitting corrosion on stainless steels in chloride solutions. He emphasized that sulphide inclusions in the oxide films dominate as pit nucleation sites and that the driving force for pit nucleation is the current in the passive state.

Accurate measurements of the current or potential transients associated with localized corrosion have become more and more important to the study of the mechanisms of pit initiation and repassivation. Oltra and Keddam (10) used a focused laser beam and abrasion by SiC particles to initiate breakdown of passive oxide films and studied the subsequent current transients related to the repassivation process. The following conclusions were made:

1) The time constant of the transient response cannot be related directly to the repassivation kinetics.

2) The electrochemical processes associated with the transient consist of two steps: (a) repassivation of the depassivated area by coupling with the surrounding surface and then (b) potentiostatic charging of the surrounding passive surface.

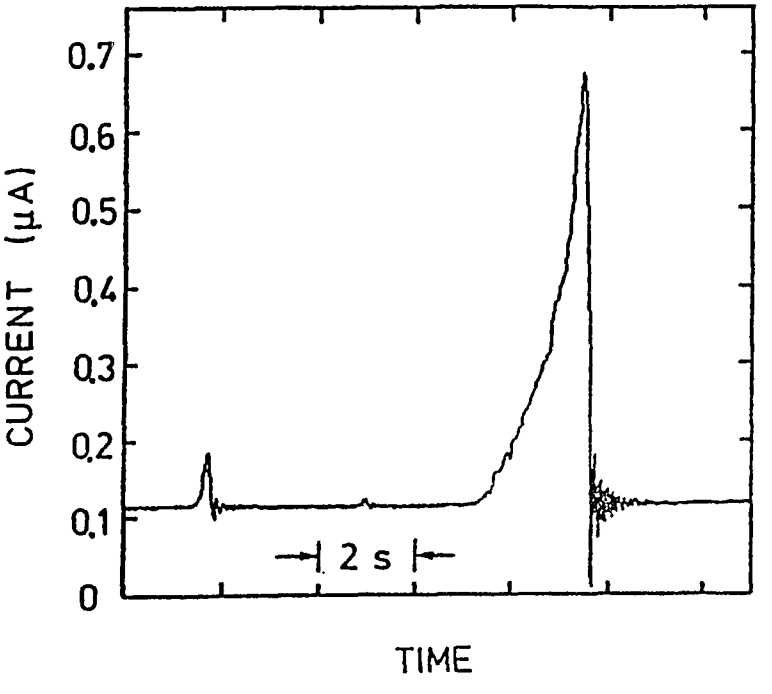

Fig. 2.2. Current transients observed during formation of a "metastable" pit (16).

3) The time constant of the current transient would be reduced in the presence of chloride, which would be then interpreted wrongly, i.e., a decrease in the time of repassivation would be measured in the presence of this depassivating Cl^- ion. Therefore the time constant of the transient response cannot be related directly to the repassivation kinetics.

The current response during depassivation and repassivation has been investigated by scratching oxide-covered metal surfaces (130-132). Pearson *et al.* (130) carried out scratching experiments of potentiostatically controlled copper strips and constructed a mathematical model that predicts the effect of the electrolyte resistance on the flow of current to a scratched electrode assuming the scratch to be shallow and represented by a rectangular planar strip. They found that the model calculations agree with experimental results. Wei *et al.* (131) measured peak current densities of Type 304 stainless steel samples with various surface areas and a fixed area of bare metal surface in a 0.6 M NaCl solution using a rapid fracture technique. They placed a reference electrode close to a site where the bared metal surface was exposed when the specimen fractured. The results demonstrated that peak current densities are logarithmically proportional to the ratio of film/bare surface. They also suggested that the very high bare-surface current densities (1 to 100 A/cm^2) reported in the literature were inflated and the effect of surrounding passive surface must be considered in the corrections. On the other hand, Kelly and Newman (132) reported peak current densities which were independent of the ratio of film/bare surface. In this case, a reference electrode was far

from the place where the scratching event took place on the metal.

Comparison of these results suggests that the characteristics of the signal transient are the result of complicated processes occurring in electrochemical cells. The current or potential transients include not only the intrinsic properties of the cells such as anodic reaction rates at localized corrosion sites, cathodic reactions at surrounding passive surface, formation of passive film, and charge and discharge of capacitive surface, but also the extrinsic influences such as the processes of film breakdown and position of the electrode. Therefore, the true electrical response which results from pit initiation and repassivation may not be completely understood without considering the effects of surrounding surfaces and solutions on signal transmission.

Isaacs *et al.* (201) used a simple 2-dimensional model to investigate the transients taking place during repassivation of the passive oxide film. They demonstrated that computer simulation can be used to construct the current response following creation of a scratch on a passive electrode. The results showed that the current response recorded from a potentiostat would be very sensitive to the positions of a reference electrode and a counter electrode. They suggested that careful analysis of the transients can yield repassivation kinetics by accounting for the contributions of the resistance, but the convolutions due to the capacitance of the passive surface are more complex and are best minimized by proper experimental setup.

2.2 Effect of Passive Surface and Solution Resistance on Localized Corrosion Transients

It has been realized that the measurement of rapid current or potential transients taking place locally on corroding electrodes is complicated by rapid electrochemical changes of metal/solution interface and transmission of the signal along the surrounding capacitive electrode surface and solution resistance (130,133-136). Oltra *et al.* (134) proposed a mathematical model to analyze the current and potential transients during pit initiation and repassivation. The model allowed one to calculate the actual current transient involved during pitting, either in potentiostatic or in free corrosion conditions. They showed the importance of the electrical characteristics of the passive surface through the value of resistance and capacitance, which can be obtained by impedance measurements even though the nature of electrochemical kinetics involved in the passive state remained unclear.

The analysis of the signal transients along a one-dimensional RC transmission line has been presented by Isaacs and co-workers (135,136). They carried out measurements of the pulse responses at various distances from one end of a semi-infinite wire where a rectangular pulse was introduced. A one-dimensional mathematical model was used for analysis of the response. Fig. 2.3 shows the equivalent circuit representing a one-dimensional transmission line model used in the model calculation. They demonstrated that the delayed time of the maximum slope and the first increase of the potential transient were induced by surface capacitance and solution resistance. However, the

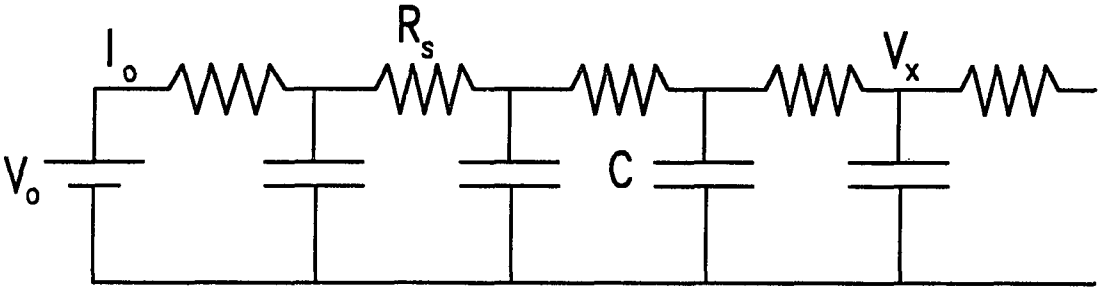

Fig. 2.3. A one-dimensional model for RC transmission lines (18).

observed time of the first increase in potential was not in accordance with predictions. This may be because the high frequency components of the transients dissipate more rapidly and the low frequencies slowly diminish.

2.3 Electrochemical Impedance Spectroscopy (EIS) Measurement

Electrochemical impedance spectroscopy (EIS) is a relatively new and powerful method of characterizing many of the electrical properties of materials and their interfaces with electronically conducting electrodes. Impedance is a more general concept than resistance or capacitance because it takes phase differences or time effects into account, and is a fundamental and essential concept in electrical engineering and electrochemistry. Impedance $Z(\omega)$ is simply defined by

$$Z(\omega) = v(t) / i(t) \qquad [2\text{-}1]$$

where $v(t)$ (applied small sinusoidal voltage) $= V_0 \sin(\omega t)$, and the resulting sinusoidal current $i(t) = I_0 \sin(\omega t + \theta)$. ω is angular frequency ($2\pi f$) and θ is the phase difference between the voltage and the current. AC impedance can be represented by a complex number:

$$Z(\omega) = a + j\,b = Z' + j\,Z'' \qquad [2\text{-}2]$$

where a and b are usually frequency-dependent real numbers. $Z(\omega)$ can be plotted in the plane with either rectangular or polar coordinates, as shown in Fig. 2.4 (137). The rectangular coordinate values are then:

$$\text{Re}\,(Z) \equiv Z' = |Z| \cos\theta \qquad [2\text{-}3]$$

$$\text{Im}\,(Z) \equiv Z'' = |Z| \sin\theta \qquad [2\text{-}4]$$

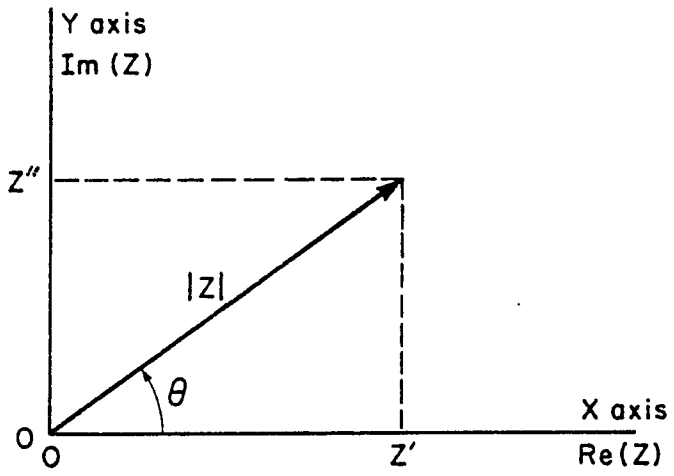

Fig. 2.4. A impedance Z plotted as a planar vector using rectangular and polar coordinates (19).

The phase angle $\theta = tan^{-1}$ (Z"/Z') and the magnitude $|Z| = [(Z')^2 + (Z")^2]^{1/2}$. Z is frequency-dependent.

EIS consists of measurement of Z as a function of f or ω over a wide frequency range. There are three different methods to generate impedance spectra. A step function of voltage can be applied at time $t = 0$ to the system and the resulting time-dependent current $i(t)$ measured. A second method is to apply a voltage $v(t)$ composed of random (white) noise to the system and measure the resulting current. Both methods require Fourier transformation to convert time-dependent results into the frequency domain. The usual and standard method is to measure impedance directly in the frequency domain by applying a single-frequency voltage to the system and by measuring the resulting current.

A typical electrochemical impedance spectrum (EIS) in the complex plane is represented by a semi-circle as shown in Fig. 2.5 (a). In this case the impedance of the system can be represented by an ohmic electrolyte resistance R_s in series with a parallel combination of the polarization resistance R_p and the interfacial capacitance C_i. However, in many systems there are apparent deviations, shown in Fig. 2.5 (b), from the ideal semi-circle exist corresponding to a rotation of the center of the capacitive semi-circle by an angle ϕ below the real axis. The deviations, which have been attributed to inhomogeneities in surfaces, are approximated by the Cole-Cole frequency dispersion formula (138):

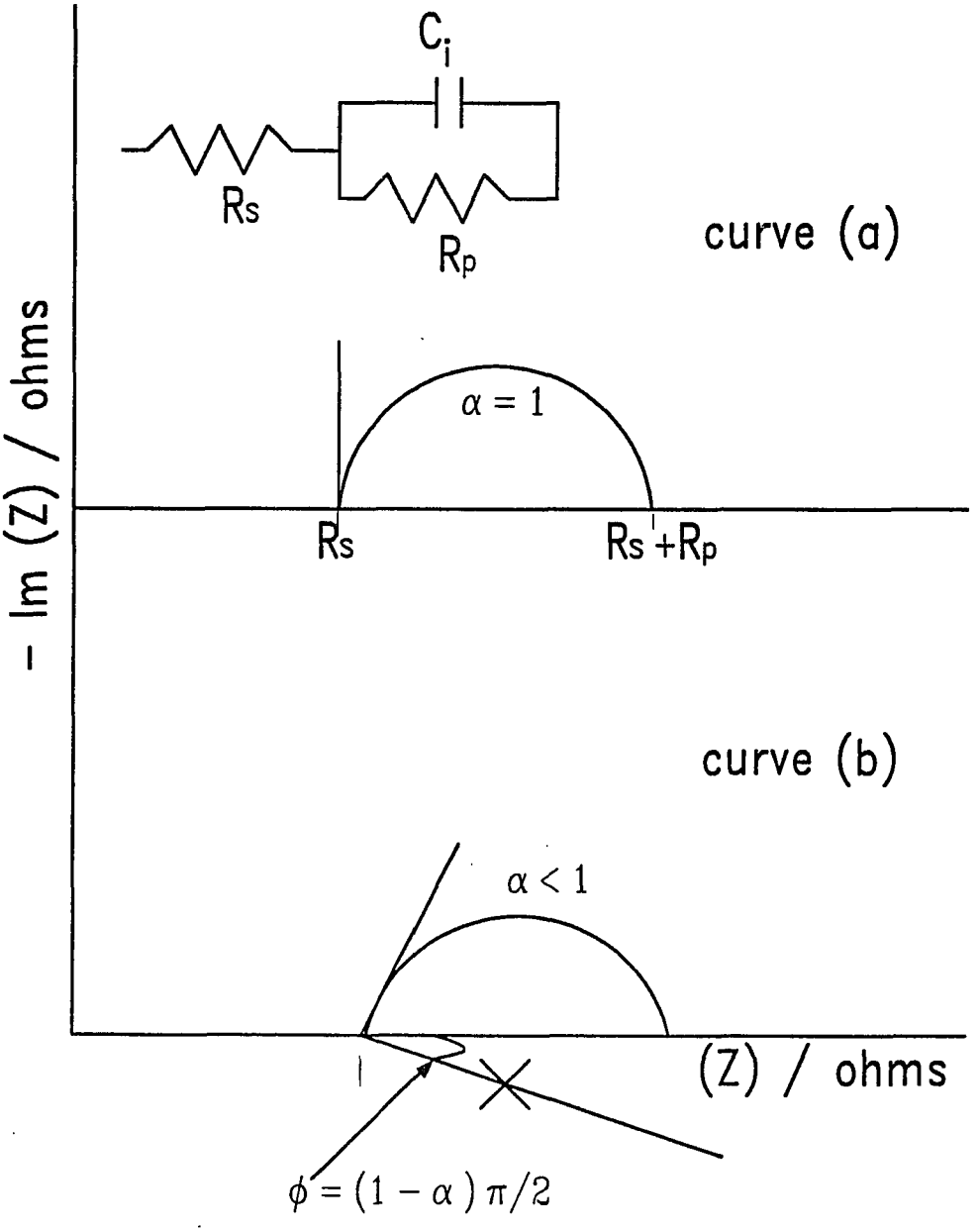

Fig. 2.5. Typical impedance spectra in a complex plane. (a) an impedance spectrum of interfaces ideally represented by RC combination and (b) an impedance spectrum resulting from frequency dispersion.

$$Z(\omega) = \frac{R_p}{1 + (j\omega C_i R_p)^{\alpha}} \qquad [2\text{-}5]$$

where α is an empirical exponent between 0 and 1 which is associated with the angle ϕ through the equation $\phi = (1 - \alpha)\pi/2$.

Another type of spectrum is designated by the constant phase angle (CPA) or constant phase element (CPE), the impedance of which has the form:

$$Z(\omega) = K\,(j\omega)^{-\beta} \qquad [2\text{-}6]$$

where K and β are frequency independent real constants and $j = \sqrt{-1}$. One of the most common constant phase angle impedances encountered in electrochemistry, that due to semi-infinite diffusion, has been known as the Warburg impedance (with $\beta = 0.5$) (139). The CPA spectrum can not be physically displayed by a limited number of RC circuit elements and the physical meaning is not clearly understood (140) except for the Warburg impedance. CPA elements can include contributions from porosity, a random mixture of conductor and insulator, dynamic disorder such as diffusion either in the electrolyte or in the solid, or fractal geometries of interfaces. Theoretical treatments using fractal geometry (141) have attempted to describe CPA phenomena, suggesting that CPA is related to the electrochemical response of fractal surfaces (142-145). Liu (143) has established a linear relationship between β and fractal dimension D_f:

$$\beta = 3 - D_f \qquad [2\text{-}7]$$

where β will become 1 for a smooth surface, the fractal dimension of which is 2. As the fractal dimension increases corresponding to the roughness of surfaces, the value of α

will linearly decrease toward 0. Kahanda and Tomkiewicz (144) discussed the impedances of silver electrodes. They compared experimental impedance data with simulated data based on equivalent circuit diagrams that contain CPA elements as well as ordinary RC elements and demonstrated that Ag deposition on silver electrodes reveals fractal geometries.

2.4 Application of AC Impedance to the Study of Localized Corrosion

EIS has been widely applied to investigate various corrosion phenomena, including mechanisms and rates of corrosion. The application of AC impedance measurements has extended to the study of localized corrosion (146-151), such as pitting or crevice corrosion (146,147), stress corrosion cracking or corrosion fatigue (148) and corrosion under porous layers (149).

Oltra and Keddam (146,147) discussed impedance models for corroding surfaces and compared experimental results with model calculations. They demonstrated that impedance spectra change during localized corrosion of passive metal surfaces resulted from frequency dependence of the AC current distribution between localized corrosion sites (LCS) and surrounding passive surfaces. In the high frequency region, the whole surface acts as an electrical conductor while in the low frequency region the passive surface is an insulator and most of the current flows into the LCS. Juttner (150) used EIS measurements to study the properties of organic coatings on metal surfaces, anodized aluminum surfaces and localized corrosion of metals. He concluded that surface

inhomogeneities can be detected *in situ* by EIS and that other characteristic parameters of composite surface layers structures in corrosion systems can be obtained by comparing experimental EIS data with appropriate model calculations of electrode interfaces.

Mansfeld *et al.* (151) evaluated corrosion behavior of polybutadiene-coated metals by EIS measurements. They demonstrated the applicability of EIS techniques to the characterization of organic coating/metal systems and to monitoring the coating efficiency of pre-treated metal surfaces. Mansfeld (152) also pointed out that the full power of the AC impedance technique is only useful if suitable models for the impedance behavior and computer programs for the analysis of data are developed, emphasizing that the development of suitable models which describe the observed corrosion behavior is critical to allow the transition from the data collection stage to the data analysis stage. Recently Crundwell (35) established a model for the impedance of an electrode covered by a precipitated salt film. A model for the dissolution of copper in HCl solutions in the limiting current range that described the modulation of the thickness of the precipitated CuCl film was derived and was shown to give a good description of the experimental data.

2.6 Application of AC Impedance to Transmission Lines

It is evident from the preceding discussion that metal/solution or metal oxide/solution interfaces cannot always be represented by a combination of generalized electrical circuit elements such as resistance, capacitance and inductance. de Levie (154)

derived a mathematical model of the AC impedance of porous electrodes. He showed that the phase angle of the impedance in a single pore is half that for planar electrodes and the magnitude is proportional to the square root of the magnitude for planar electrodes. Macdonald *et al.* (155) theoretically examined the applicability of EIS for detection of localized corrosion on rebar in concrete using a transmission line model. The results of the theoretical calculations suggested that corrosion can only be detected at very low frequencies. The calculations relied on theoretical interfacial impedances consisting of various circuit elements.

Fiaud *et al.* (156) have considered the impedance behavior of disc electrodes with different positions of a reference electrode as a function of electrolyte thickness. They concluded that the impedance of a distributed system is strongly dependent on the location of the potential probe and that a simple model can be used to interpret the impedance data, optimizing the position of the reference tip with respect to the effect of the frequency-dependent potential distribution.

Chapter 3

CONCLUSIONS FROM LITERATURE SURVEY

Chapters 1 and 2 extensively discussed various aspects of pitting corrosion. A number of studies on pitting corrosion have been carried out since the early 20th century and significant progress has been accomplished in many areas such as new spectroscopic techniques to investigate passive films, model calculations of pit solutions, understanding of the role of salt layers for pit propagation and the application EIS techniques to corrosion studies. However, there still exists many unknown parameters for a thorough understanding of pitting corrosion from its initiation to propagation and repassivation. For example, the cause of pit initiation is unclear even though various theories can explain it to some extent. This should be understood through a study of passive films, the properties of which may vary with the intrinsic properties of metals such as composition, heat treatment and level of impurity, and extrinsic parameters including potential and surrounding environments. We suggest that a variety of *in situ* techniques should be developed to study many aspects of passive films.

The properties of solutions inside localized corrosion sites may be better characterized than the properties of passive films. This is mostly due to theoretical calculations that use simple diffusion/migration equations with various plausible assumptions. However, in the case of stainless steels, complexity arises from the

solution mixture of iron, chromium and nickel ions inside pits in the presence of chloride ions. The main difficulty is that diffusion coefficients of the metal ions, solubility of the salt mixture and stability constants of various metal-chloride complexes in this system are not available. The other uncertainty may come from the ratio of the alloy elements (mainly iron, chromium and nickel) in the solution mixture developed inside localized corrosion sites. Many model calculations assumed that the ratio of the metal ions in the pit solution equals that in the alloys. The experimental results by Lott and Alkire (91) and Nash and Kelly (92) did not support the assumption. But the chemical compositions of the solutions analyzed by various *ex situ* techniques also can raise doubts whether the results correctly represented the chemical compositions of the solutions inside the cavity areas where localized corrosion takes place. The *ex situ* techniques for analysis of such solutions may not provide the results which can verify theoretical models.

The studies concerning salt film during metal dissolution have been carried out extensively: however, the experimental methods were mostly limited to electrochemical measurements. Chemical analysis of salt layers has not been carried out because their presence only occurs during dissolution of metals. *Ex situ* analytical methods were therefore not applicable and *in situ* techniques must to be developed to study the chemistry of salt layers.

A number of investigations have been carried out using EIS measurements, concentrating on a primary ability of EIS technique, that is, establishing a generalized

equivalent circuit corresponding to a passive interface or localized corrosion site. However little attention was paid to the AC impedance technique for investigating corrosion transients. The power of EIS technique can be expended to the study of complicated localized corrosion transients. The use of interfacial impedance data for model calculations along transmission lines promises to punish an accurate estimation of the effects of solution and of surrounding surface on localized corrosion transients.

Chapter 4

X-RAY FLUORESCENCE SPECTROSCOPY

4.1 Fundamentals of X-ray Fluorescence Technique

4.1.1 Electronic Transitions in an Atom

The fundamental ideas of x-ray spectroscopic techniques are based on electronic transitions between energy levels in an atom, that are induced by x-rays. Fig. 4.1 illustrates the processes of x-ray absorption and fluorescent emission by electronic transitions between energy levels in an atom (159). The excited state is achieved by electron transition from lower energy levels to higher levels. Bombarding an atom with charged particles such as electrons, protons and ion beams or with photons having a sufficiently high energy can eject electrons from the core levels (usually K, L shell) to the empty continuum levels (the unoccupied valence band). The excitation process consequently creates a hole at the core level. The reverse process of the electronic transitions to its ground state involves most frequently electronic transitions to the core levels from the level situated immediately above it, with emission of a x-ray fluorescence photon with an energy corresponding to the difference between the energy levels.

The difference in atomic excitation by photons and by charged particles is in the excitation process (160,161). A photon of electromagnetic radiation transfers its energy to an electron bound in an atom. This photoelectric absorption may occur if the photon

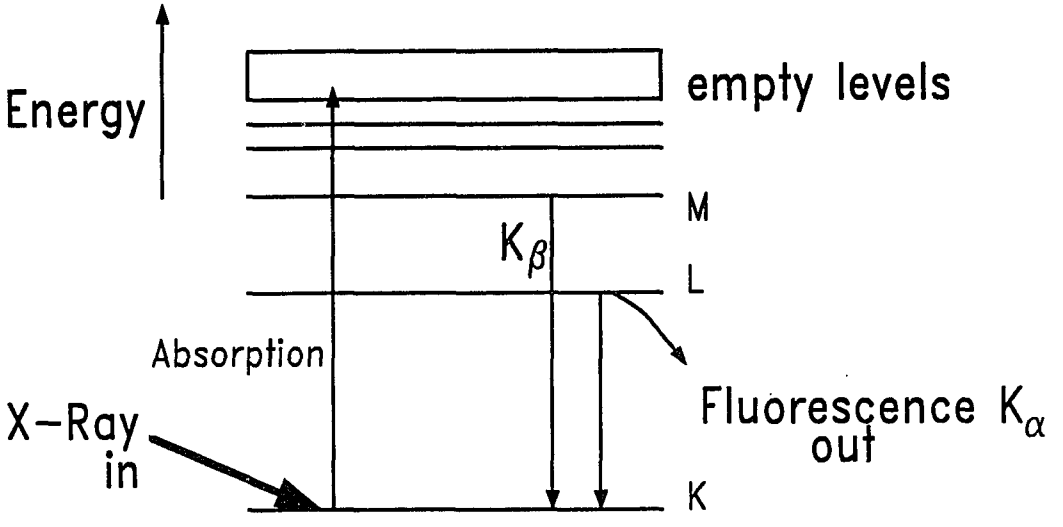

Fig. 4.1. A schematic diagram of electronic transition between energy levels in an atom during x-ray absorption and fluorescence.

energy $h\nu$ satisfies the following condition:

$$h\nu \geq E_b \qquad [4\text{-}1]$$

where E_b is the binding energy of the electron in a given energy level. The difference between the primary energy of the photon and the binding energy of the electron is carried away by the electron, in the form of its kinetic energy T:

$$T = h\nu - E_b \qquad [4\text{-}2]$$

The K absorption edge corresponds to the binding energy of the 1*s* electron (162). On the other hand, atom excitation by the charged particles simply ionize an atom by ejecting the electron in the core energy levels if the charged particles have a sufficient energy, i.e., greater than the ionization energy of the core levels in an atom. However, the subsequent process of emission of x-ray fluorescence is the same for both cases. The yields for atomic excitation by charged particles are larger by several orders of magnitude than the corresponding photon excitation and charged particles can be strongly focused, which allows microanalysis of the sample. The disadvantages of using charged particles is: 1) the strong *Bremsstrahlung* (braking radiation) overlaying the characteristic radiation of the sample and 2) the system needs a high vacuum environment.

The characteristic x-ray fluorescence which results from an electronic transition to the K energy level from the L level is named K_α and the electronic transition from the M level is named K_β. The energy of the individual fluorescent lines of characteristic radiation is always slightly lower than the excitation energy (absorption edge) of the

corresponding level. Each atom has a characteristic set of x-ray energies, which can be used for the identification of the element. Table 4-I presents the K absorption edges, and the corresponding fluorescence K_α and K_β values of the elements of interest in this work (162).

4.1.2 Photon Excitation Yield

Atomic excitation by photoelectric absorption involves transferring of the photon energy to an electron bound in an atom. The higher the binding energy of an electron, the higher the probability of photoelectric absorption, i.e., the absorption takes place mainly in the K energy level (163). The mass absorption coefficient μ_{ph} (159) is given by

$$\mu_{ph} = a\frac{Z^5}{(h\nu)^3}\frac{N}{A} \qquad [4\text{-}3]$$

where N = Avogadro's number,

A = the atomic mass of an element,

$h\nu$ = the energy of incident radiation,

a = a proportionality constant, and

Z = the charge of a nucleus.

The μ_{ph} represents in practice the "excitation yield" or "photon-excitation yield of atoms". The excitation yield increases with the atomic number. However, an increase in the photon energy of the incident radiation decreases rapidly the excitation yield.

Table 4-I. Photoelectric absorption edges and x-ray energies of K-series (in KeV).

Z	Element	K	K_{α}	K_{β}
18	Argon	3.203	2.957	3.192
22	Titanium	4.964	4.510	4.931
24	Chromium	5.988	5.414	5.946
26	Iron	7.111	6.403	7.057
28	Nickel	8.331	7.477	8.264
29	Copper	8.980	8.047	8.904
35	Bromine	13.48	11.92	13.29

Therefore the excitation yield of the atoms in a given energy level does not increase with the atomic number, but rather shows a rapid decrease.

4.1.3 Fluorescence Yield

The "fluorescence yield" ω_K is expressed as the ratio of the number of fluorescence photons $N_K^{(f)}$ belonging to a given series to the number of all the atoms N_K which have been excited in this level within the same time interval (164):

$$\omega_K = \frac{N_K^{(f)}}{N_K} \qquad [4\text{-}4]$$

X-ray fluorescence is competitive with the Auger effect which can only take place when the energy difference between K and L level is greater than the energy of L level. The value of the fluorescence yield is always less than unity and increases with the atomic number since the Auger effect decreases with increasing atomic number. The fluorescence yield for series K is always higher than that for series L. Fig. 4.2 illustrates the fluorescence yield vs. atomic number.

4.2 Quantitative Data Analysis

Quantitative x-ray fluorescence analysis has been well established for many years and a number of possible methods of calibration are available (159). The basic principles were presented by Gigante and Hanson (165). Two methods are mainly used for quantitative analysis. The first is an empirical method exemplified by the multiple regression treatment of Lucas-Tooth and Pyne (166). This method calculates the

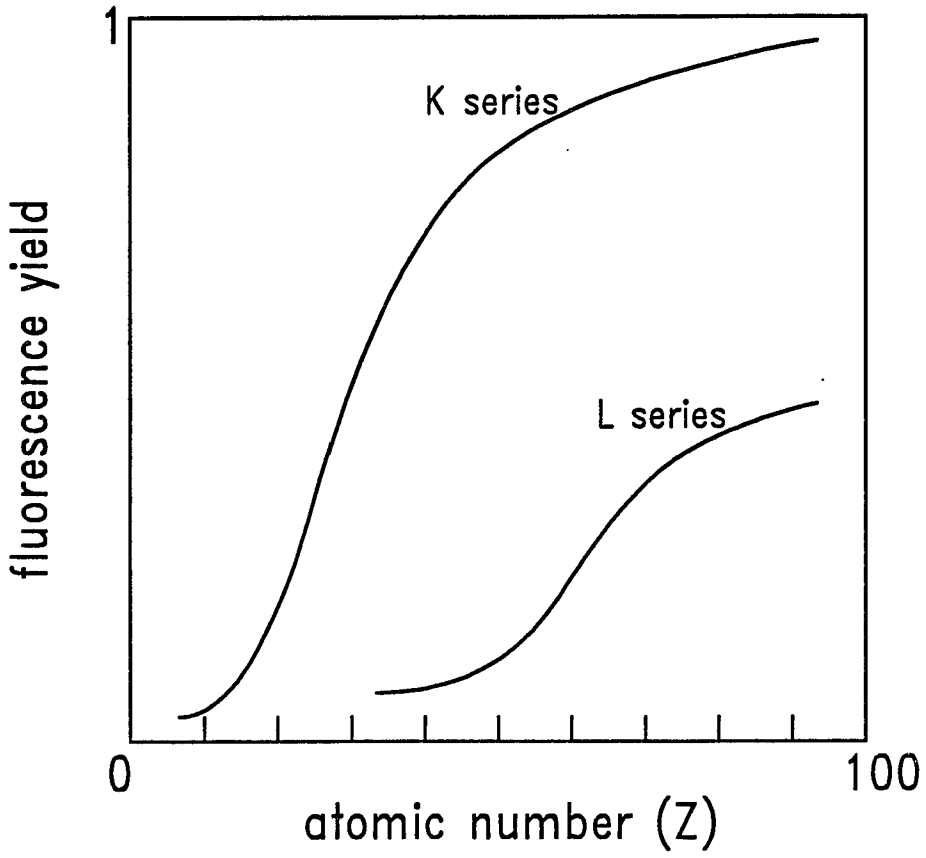

Fig. 4.2. Fluorescence yield as a function of atomic number (159).

absorption and scattering effects of each element present in a sample from the fluorescent intensities measured. Standards are required which are similar to the sample. The second is the fundamental-parameter method (167,168). This method derives the expected intensities from a sample composition and geometry and three sets of basic information: the x-ray spectral distribution of the incoming beam, the mass absorption coefficients for each element in the sample, and their fluorescence yields.

In the present study, the fundamental-parameter method was employed to convert fluorescent intensities to concentrations and the reliability of this approach was investigated using known standards. The theoretical relationship between the concentration and the fluorescence intensity I_i of a given element and the individual concentrations of all the components in a sample was given by Sherman (171,172), Shiraiwa and Fujino (173), Criss and Birks (167) and Zhang (174). A generalized form of the equation including absorption and enhancement effects is represented by

$$I_i = KW_i \sum_{k=1}^{N} F_{ik}(E_k)[1 + \phi_{ik}(E_k, W_1, W_2, \ldots, W_j, \ldots, W_n)] \qquad [4\text{-}5]$$

where K = a constant depending on sample geometry and the fluorescence yield of the element,

W_i = weight fraction of the specific element i,

$F_{ik}(E_k)$ = absorption function of the matrix dependent upon the chemical composition of the sample at the energy E_K, and

ϕ_{ik} = enhancement function of the intensity due to the fluorescence radiation of all the elements in a sample.

The measured intensities of the elements are expressed relative to the x-ray intensities of standard samples R_i^m. Knowing all these parameters, equation [3-5] can be used for calculating the relative intensities or the concentrations of the specific elements. The calculations must be carried out by an iterative procedure. After every stage of such an iteration procedure, a new estimate of the intensity or the concentration (weight fraction) for the element i is made which approach closer and closer the actual value. Fig. 4.3 illustrates the procedure for obtaining the concentration of the element by iteration. The procedure can be explained as follows:

1. The relative fluorescence intensities of the specific elements are obtained from the intensities of the sample and the standard:

$$R_i^m = \frac{I_i^m}{I_i^o} \qquad [4\text{-}6]$$

The relative intensities R_i^m serve as the first estimates of the W_i values, as shown by a straight line in Fig. 4.3.

2. The W_i values are scaled so that their sum is unity,

$$\Sigma W_i = 1 \qquad [4\text{-}7]$$

3. The obtained concentration W_i values are inserted into equation [4-7] and the corresponding relative intensities R_i' are calculated for each element i.

4. These new relative intensities R_i' are used for calculating new estimates of concentrations W_i'. The following linear relationship is usually used:

The new estimates of concentrations are again scaled to add to unity.

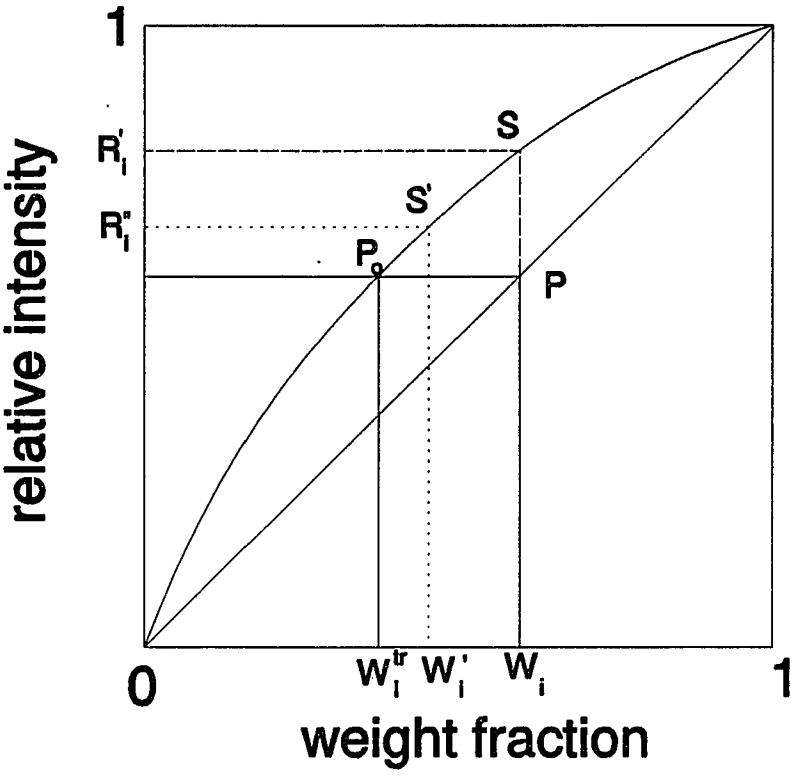

Fig. 4.3. Principle of the iterative procedure for calculating concentration

$$W_i' = \frac{R_i^m}{R_i'} W_i \qquad [4\text{-}8]$$

5. The sequence of steps 2, 3 and 4 is repeated n times until the corresponding S point of curve 2 approaches, within the desired limit, the point P_0 which corresponds to the actual concentration W_i^{tr} of the element i. As this true value is never known, the iteration stops when the difference between the successive estimates is less than the required accuracy of iteration. The fundamental parameter method was seriously hindered in the early stage of its use by the fact that it required the use of a large computer and long computing time. However this difficulty has been overcome by development of computer technology and software.

4.3 Comparison of XRF and Other Analytical Methods

The principal advantage of x-ray fluorescence analysis is its simplicity and the accuracy of the technique for analysis of elements in a sample. Moreover, the method is a non-destructive one and can be used for on-line or on-stream measurements, speeding up the automation of various industrial processes. Analysis using XRF gives some advantages over other techniques (175). Ultraviolet emission (UVE) and atomic absorption (AA) as well as XRF are commonly employed in a routine analytical laboratory. UVE has multichannel capability with fast analysis of a sample. The desirable sample type is a solid disk or pellet. However, interelemental influences are not easy to predict. AA has a very high accuracy in determining the amount of elements

in a sample and interelemental effects are predictable, but it is typically a single-channel instrument and mostly needs a solution-type sample. XRF may not match the speed of UVE and sensitivity (detection limit) of AA; however, the x-ray technique is capable of multicomponent analysis, applicable over a wide concentration range and has predictable interelemental effects. X-ray spectra are unique and relatively uncomplicated. Elemental spectral overlap is uncommon and the relationship between characteristic line intensity vs concentration can be obtained easily.

It is useful to make a distinction between techniques that use a crystal spectrometer, which are referred to wavelength-dispersive (WD) (176), and energy-dispersive which use solid state detectors (ED) (177). The energy-dispersive spectrometer (EDS) techniques are of great interest since they allow for the simultaneous detection of more than one fluorescence line while providing a better efficiency than is available with a crystal spectrometer (WD).

4.4 Synchrotron Radiation (SR) X-ray Sources

The basic mechanism producing x-ray fluorescence radiation is the same from both SR and conventional primary x-ray radiation. The difference arises from the characteristics of the primary x-ray radiation. Unlike those from conventional x-ray sources, the x-rays from synchrotron light sources have very high intensity. Electrons or positrons are injected in discrete bunches into a circular vacuum chamber from some preaccelerator device. These charged particles are steered around the storage ring and

focused by electro-magnets and maintained at a constant high energy in the 100 million eV range using radiofrequency (rf) boosters (178). This rf energy input is required to compensate for the energy loss due to emitted synchrotron radiation resulting from acceleration of the charged particles.

Besides high intensity, SR x-rays posses a lower emittance than conventional radiation sources (178). The x-rays with low emittance are naturally collimated in a direction normal to the ring and maximize the intensity on a sample specimen. These SR x-rays makes it easier to construct a microprobe. The conventional x-ray sources are characterized by a large divergence of the beam that makes it more difficult to collimate the primary radiation. A synchrotron produces photons that are linearly polarized in the plane of the electron orbit, i.e., the plane of the storage ring shown in Fig. 4.4 (21). By placing the detector in the plane of the storage ring at 90 ^{o} to the beam, the intensity of the scattered radiation emitted by the sample decreases. The divergence angle $1/\gamma$, where γ is the ratio of the ring energy to the rest energy of the charge, is approximately 0.0012^{o} at National Synchrotron Light Source (NSLS) at Brookhaven National Laboratory (BNL). When compared with conventional XRF, SRXRF can have a better minimum detection limit (MDL) and provides opportunities for microanalysis. The acquisition time for data collection is significantly smaller than the time required by conventional XRF.

4.5 The Present Work

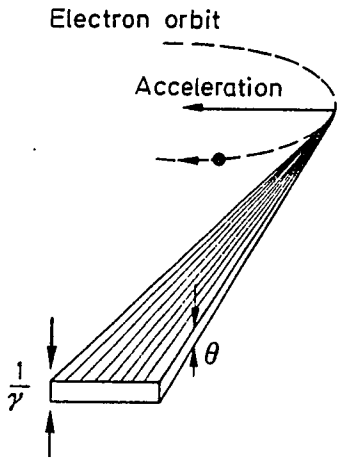

Fig. 4.4. Schematic of x-ray beam from a synchrotron source and its polarization characteristic (179).

Analysis of chemical compositions of metals and alloys by the XRF technique was discussed by Von Hevesy (180) over 40 years ago. Since then, rapid growth of this technique has continued at a steady pace. In today's highly automated production facilities, x-ray fluorescence spectrometry has been found to be widely applicable to process control in the metal industries.

In the present work, *in situ* fluorescence microanalysis using SR white x-rays and an energy-dispersive spectrometer (EDS) (181,182) are carried out in order to determine the chemical compositions of the solution and the salt layer within a one-dimensional artificial pit of stainless steels in a chloride solution. This enables simultaneous counting of the x-ray fluorescence from all the elements in the sample solution of an occluded area at each position and calibration with the fundamental parameter method reduces the time required to obtain concentration gradients. Measurements of the fluorescent intensities of the major constituents (Fe, Cr, and Ni) of the stainless steels, using synchrotron radiation x-ray fluorescence spectrometer (SRXRF), can be made *in situ* under electrochemical control of the sample and more rapidly than any other analytical method.

A modified "NRLXRF" Fortran program (168) is used to convert fluorescent intensities to the concentrations of the metal elements as a function of position in an artificial cavity formed by dissolution of the stainless steel foil in a acidic chloride solution. The chloride compounds of the metal elements are assumed to be $FeCl_2 \cdot 4H_2O$, $CrCl_3 \cdot 6H_2O$ and $NiCl_2 \cdot 6H_2O$ in the solution phase with a density of

1.92, 1.76 and 1.85, respectively (169,170). Minor elements and impurities of the steel which are present in the solution, were not included in the calculations. The experimental procedures will be discussed in Chapter 5.

Chapter 5

EXPERIMENTAL

The experimental methods used in this work are divided into two parts; (i) *in situ* and *ex situ* microanalysis of artificial pits and corrosion products, and (ii) measurements of electrochemical impedance spectroscopy (EIS) and signal transients along a one-dimensional transmission line.

5.1 Microanalytical Measurements during Anodic Dissolution of the Metal

Most of the analytical methods which have been used to measure metal concentrations of pit solutions are *ex situ* (84). The experimental results presented in the literature (92-95) are somewhat controversial and also not comparable to theoretical models (79) which give microscopic information on the metal ionic concentrations of the solution within occluded areas of localized corrosion. However model calculations (79) assume that the relative ratio of metal ions in the pit solution equals that in the alloys, but this was not observed experimentally (94,95). XRM (183) is used in this work to determine relative local compositions of metal ions in the solution within an artificial pit. The results from XRM measurements will allow comparison of the experimental data with model calculations.

The microanalytical measurements and microscopic observations were carried out

using several experimental methods:

1) design of a one-dimensional artificial pit to allow x-ray measurements and microscopic observations,
2) *in situ* x-ray fluorescence measurement of concentration gradients pit solutions and salt layers,
3) *in situ* video optical microscopy (VOM) observation of the salt layer during anodic dissolution of the metal, and
4) optical microscope observation and SEM analyses of the corrosion products.

5.1.1 A Novel One-dimensional Artificial Pit

Since the microscopic size of a pit makes it difficult to perform the experiments and to make measurements, various kinds of simulated pits have been used (84). Among them, a "pencil-type" simulated pit or crevice, shown in Fig. 1.6 (b), made with a wire embedded in an insulator has been widely used because of its symmetrical geometry which simplifies theoretical calculations (the dimensionality of the system is reduced to one). The use of a pencil-type pit with various *in situ* electrochemical methods (121) and micro-electrode analytical techniques (89) has contributed to the understanding of the chemistry of the solution within localized corrosion sites (LCS).

However, this geometry is not suitable for x-ray measurements and optical microscopy observations. The cell for x-ray measurements should be uniformly thin.

A very thin metal foil has been selected as an electrode instead of a wire electrode. A new geometry, a "sandwich-type" pit (77,100) shown in Fig. 5.1, was designed not only to simulate one-dimensional diffusion processes taking place in pitting or crevice corrosion, but also to fulfill the requirement of x-ray fluorescence measurements. The cell is called a "XRM pit cell" in the present thesis. This geometry allows x-ray fluorescence intensities to be obtained from the bulk solution to the metal. The other cell shown in Fig. 5.2, which is called a "XAS pit cell" in the present thesis, being developed for x-ray absorption measurements is unsuitable, for good spacial resolution and for the measurements at the region of the pit mouth due to thickness effect of the plastic and epoxy. However, the use of the XAS pit cell is essential in order to investigate the chemical nature of elements and structures of the metal complexes in the pit solution.

The XRM pit cell consists of a thin stainless steel foil strip, approximately 2 mm wide (thickness depends on the types of the metal: the pure stainless steel is 12 μm, the commercial stainless steel is 16 μm, and the nickel is 30 μm), mounted between thin Mylar sheets (200 μm in thickness) and sealed with an epoxy glue (Epoxy 50, Transene Co, Inc.). The compositions of the commercial and the pure stainless steel foils are presented in Table 5-I. The thickness of the foils were measured using a micrometer and SEM photographs. The epoxy was cured at 100^{o}C for 4 hours in air. This sandwiched unit adhered to a thick plastic block using 5 minute epoxy (Devcon Co.). The cross-section of the unit was polished with a 600 grit finish and cleaned with distilled water. The bottom unit of the cell was connected to the upper unit using a Teflon tape (100 μm

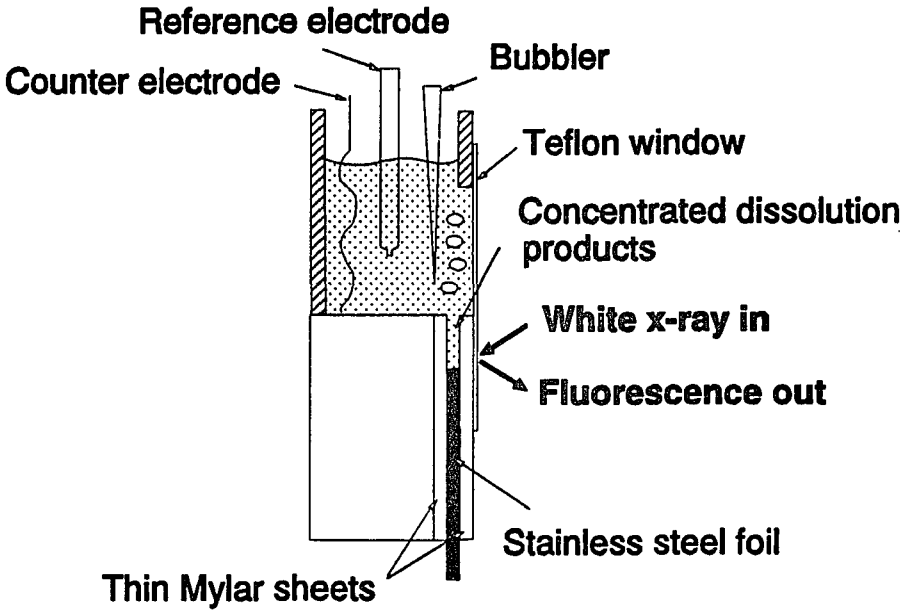

Fig. 5.1. XRM cell of one-dimensional artificial pit.

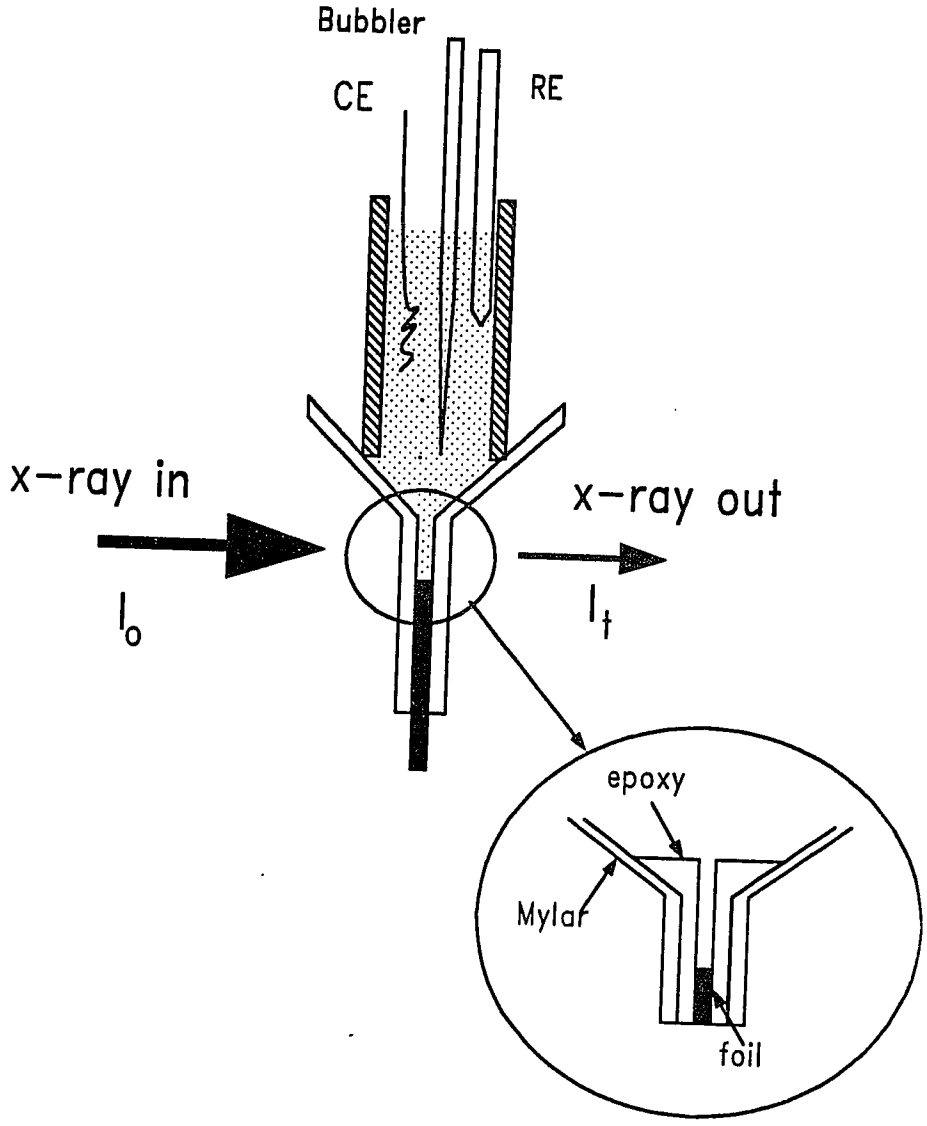

Fig. 5.2. XAS cell of one-dimensional artificial pit.

Table 5-I. Composition of stainless steels, by weight %

Element	Commercial steel	High purity steel
C	0.11	0.005
Mn	1.70	0.01
P	0.013	0.003
S	0.002	0.003
Si	0.54	0.01
Cr	17.73	17.87
Ni	12.81	11.95
Cu	0.12	0.01
Al	----	0.005
Ca, Mg	----	0.001
O	----	0.01
N	----	0.001
Mo	0.28	-----
Fe	Balance	Balance

in thickness) that formed a window to the cell and through which the x-ray beam entered. Kapton, Mylar and Teflon are mostly used in synchrotron radiation x-ray experiments because of their durability in high intensity x-ray beams and small interference with x-ray signals (184).

The cross-section of the foil strip was exposed to the electrolyte, a 0.5 M HCl + 0.5 M NaCl solution which was made by mixing equal amounts of 1 M HCl and 1 M NaCl solutions. The foil was dissolved downward at a constant potential of 600 mV (vs SCE) leaving a rectangular shaped artificial pit. During dissolution *in situ* XRM measurements and VOM observation were carried out. The potential was controlled by a PAR Model 173 potentiostat and the corresponding current, i.e., the localized corrosion current i_{lcc}, was recorded with a HP7132A recorder.

5.1.2 *In situ* XRM Measurements during Dissolution of the Stainless Steel Foils in Chloride Solutions.

Synchrotron radiation (SR) x-ray sources have been discussed extensively in the literature (181-183). Electrons or positrons at energies of several GeV are confined in a path comprised of circular and straight sections by a set of magnets. X-rays are emitted by the acceleration of the beam as it moves in a circular path in the bending magnet sections. Three important properties of the SR x-ray source must be considered when applied to the XRM measurements (183). The first one requires a wide and continuous spectral range of very high intensity photons. The second is a high degree

of polarization in the plane of the electron orbit. This reduces background scattering into a detector positioned at 90^{o} to the sample in the plane of the ring. The last requirement is a natural collimation that permits the focusing of the x-rays.

The fluorescence measurements were carried out with high intensity white x-rays at the National Synchrotron Light Source Beamline X-26A (181,182). A schematic diagram of the beamline is shown in Fig. 5.3 (181). The beam coming from the storage ring was initially collimated to approximately $100 \times 100\ \mu m^2$ by a set of motorized slits and was further collimated down to a size of about 20 or 8 μm in diameter after passing through a "pinhole". This micron-size of the beam provides sufficient fluorescent intensities to the solid state detector. The cell was positioned with the plane of the foil at 45^{o} to the beam. It was held on a motorized X-Y-Z stage and the dissolution of the foil was initiated by applying a constant potential of 600 mV (vs SCE) in chloride solution. Between the incident beam and the detector a video camera connected with a microscope was installed so that the sample was monitored during the x-ray measurements. Helium gas was bubbled into the bulk solution to stir the bulk solution and thus avoid the concentration build-up of diffusing species at the mouth of the cavity. A thin film of titanium ($\sim$ 500 Å) deposited on a thin Kapton film ($\sim$ 100 μm) was placed in front of the XRM pit cell to provide a constant fluorescence intensity per unit second which can be used for normalizing the fluorescence intensities of the metal elements in the sample solution.

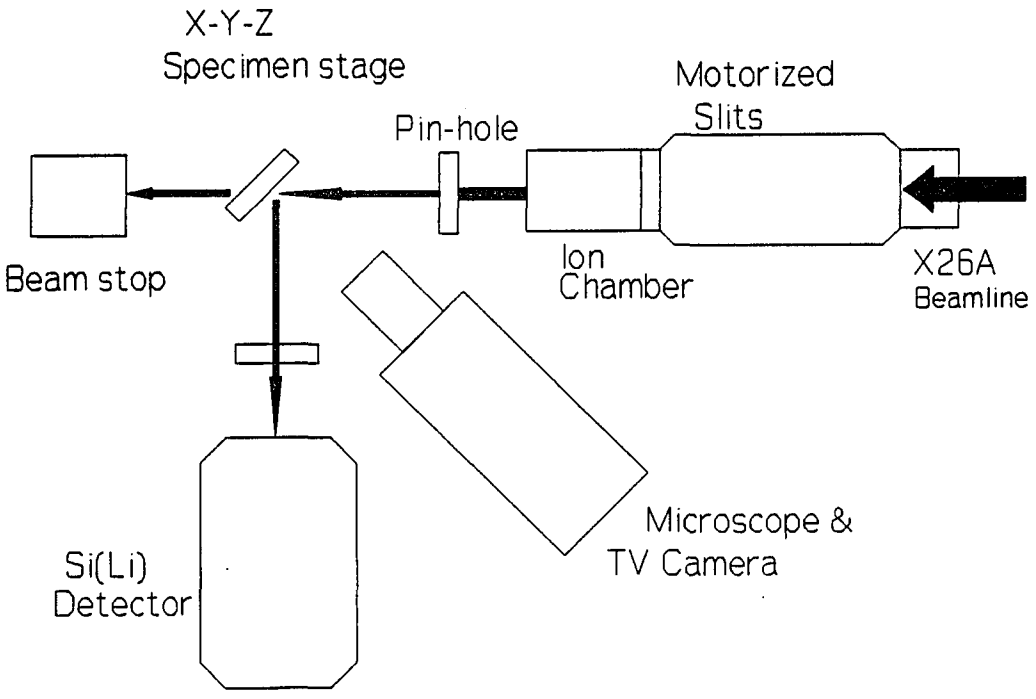

Fig. 5.3. A schematic diagram of X-26A beamline.

There are two modes of collecting data. The first one is the "spectrum" mode that stores data as a full fluorescence spectrum which can immediately show relative composition in a sample. The other is the "region-of-interest (ROI)" mode that only stores the fluorescence intensities under the peaks which are predefined by the user. A computer program that runs the XRM measurements and collects data automatically subtracts background fluorescence counts. Fig. 5.4 shows a schematic diagram of this computation. In Fig. 5.4, E_l and E_r are a left and right ends, respectively, of the predefined energy range for an element of interest. The slope a is computed from the fluorescent intensities measured at the both ends (E_l and E_r). A background-subtracted fluorescent intensity F_{true} at energy E_1 is then calculated from the equation $F_{true} = F^{E1} - F(E_1)$, where F^{E1} and $F(E_1)$ are the fluorescent intensity and the background fluorescent intensity at energy E_1. Consecutive computations between $E_l \leq E \leq E_r$ are carried out to complete background correction. ROI mode is useful when two or more sets of data need to be compared and analyzed. In this work, ROI mode was generally used and the predefined regions of the peak areas were, in most cases; argon K_α, titanium K_α, chromium K_α, iron K_α, nickel K_α, and copper K_β. Table 5-II shows the ROI selected for each element.

It takes a finite time for the electronics of the solid state detector to process the signal from a single photon. During this time, other photons incident on the detector will not be collected. For high photon fluxes, this gives a significant "dead-time" so that counting only takes place for a measured fraction of the total time available. The

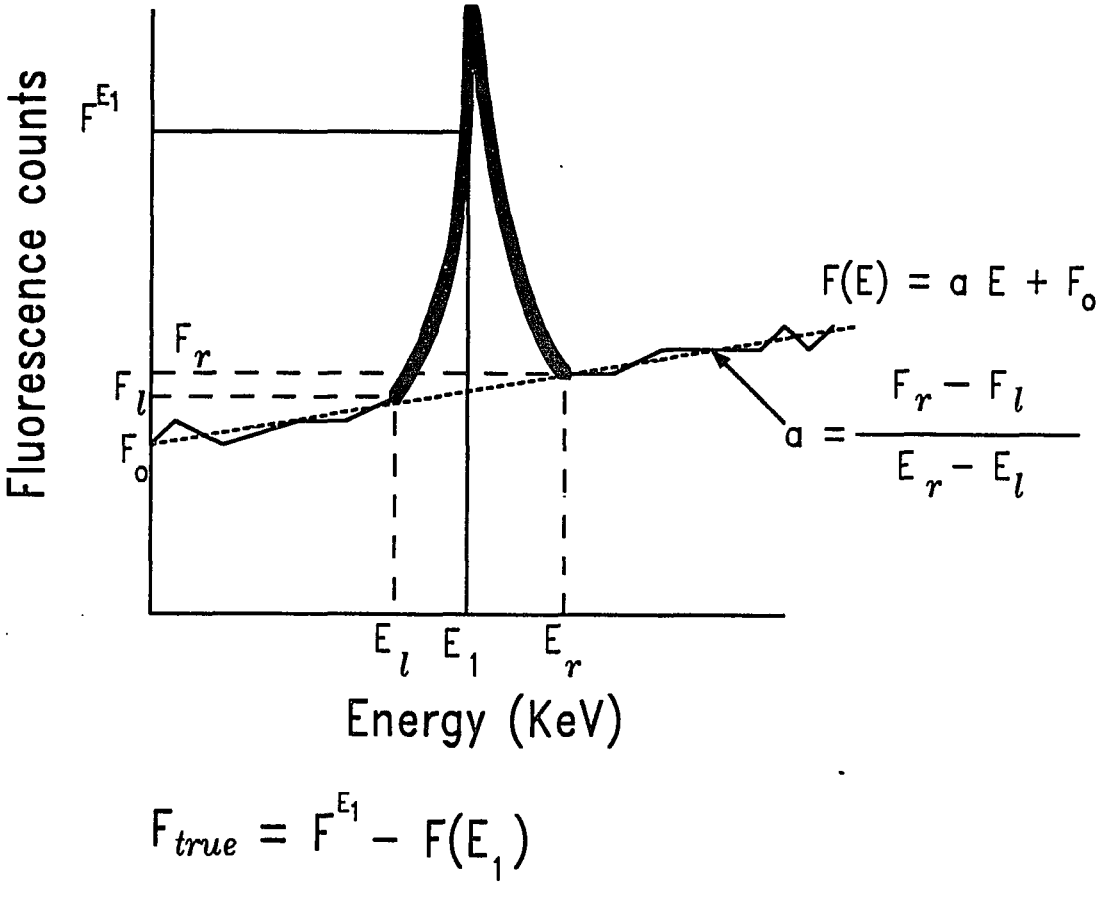

Fig. 5.4. A method of calculating a fluorescent intensity in a region-of-interest.

Table 5-II. Energy ranges of region-of-interest for each element preset during the XRM measurements.

Z	Element	Energy range (KeV)
18	Argon	2.79 - 3.12
22	Titanium	4.30 - 4.73
24	Chromium	5.11 - 5.66
26	Iron	6.12 - 6.72
28	Nickel	7.27 - 7.81
29	Copper	8.82 - 9.03

number of counts is therefore normalized to this "live-time". This value is then divided by the current in the storage ring, which is proportional to the incident x-ray intensity that may vary during measurements. Other methods to normalize the counts will be discussed in Chapter 6.

5.1.3 X-ray Microprobe Scan over the Pit Solutions

Linear scans, after establishing a steadily dissolving foil edge at a constant potential of 600 mV (vs SCE), were made from the base foil to the bulk solution, through the artificial pit, by stepping the cell vertically with a step size between 25 ~ 50 μm and a sampling time (real time) of 30 ~ 60 sec. A beam size of 20 or 8 μm in diameter was used for the scan over the pit solution. The fluorescent intensities of each element (Ar, Ti, Cr, Fe, Ni and Cu) in the pit solution were collected as a function of distance from the metal interface. Consecutive linear scans allowed us to collect sets of data for various pit depths, which resulted from continuous dissolution of the foil. One scan typically took 10 - 20 minutes depending on the pit depth, step size and sampling time. Variation of current during one full scan was less than 2 % if a pit is deeper than 1 mm.

5.1.4 X-ray Microprobe Scan across the Metal/Solution Interface

A fine step size of 2 μm and a sampling time of 60 sec were applied for the scans across the interface to study the chemistry of the salt layer. A fine scan over the interface (the total length of the scan was approximately 40 ~ 60 μm) and a linear scan

across the pit solution were alternatively carried out to obtain chemical information of pit solution and salt layer as a function of pit depth. The current was recorded with a HP7132A recorder and monitored with a Keithley 614 electrometer. The potential which was not interrupted or changed from the beginning of dissolution until finishing the scans had a constant value of 600 mV.

After finishing the scans over the metal and the pit solution and across the salt layer, the fine scans across the interface were continued to study the chemical composition of salt layers as a function of applied potential. The artificial cavity was sufficiently deep so that minimum changes in the depth took place during the study. First, the applied potential varied between 1.0 V to 0 V with a step of 200 mV and the fine scans were carried out after each potential change when the current stabilized back to the steady state value. The thicknesses of the salt layers were also monitored through the optical microscope during each measurement. Next, the applied potential was turned off to allow the salt layer to dissolve away, and a scan over the interface which had no salt layer was then taken. The potential was also interrupted by disconnecting the potentiostat for a short period of time (5 - 30 sec) to observe the changes that takes place at the metal interface. These potential-interruption experiments were carried out only after finishing the XRM measurements because potential interruption resulted in metal fragments being left within the cavity acting as a barrier to the diffusion path, that would complicate the XRM measurements.

An accurate determination of the beam profile after passing through a 20 or 8 μm "pin-hole" was made by scanning the beam across a 4 μm Au coated tungsten wire with a step size of 2 μm. After finishing all the XRM measurements the bulk electrolyte was changed to a standard solution of 0.5 M $NiCl_2$ + 0.8 M $CrCl_3$ to examine the uniformity of the thickness within the artificial pit. Scans over the cavity containing the standard solution were carried out until the fluorescent intensity indicated that the diffusion of the standard solution was complete across the artificial pit.

5.1.5 Video Optical Microscopy (VOM) Observation of Salt Layers

Video optical microscopy (VOM) has been widely used, especially in biological studies (185). Recently Isaacs *et al.* (186) used a VOM system with the vibrating probe technique to investigate the *in situ* changes in the current density distribution over corroding steel surfaces. Tobias *et al.*(187) adapted video microscopy to study electrodeposition. A video camera attached to an optical microscope gives an image of the object changing with time, so that a live photograph can be obtained using a graphic printer in order to compare the micrometer-size change of metal/solution interfaces during anodic dissolution of metals in the artificial pit. Video tape and computer disk can be used as a storage medium. These stored images can be retrieved and displayed on a video monitor for further analyses and enhancement of the images by using a computer.

Two VOM systems were used for the observations: one was at the x-ray Beamline

X-26A and the other wa constructed in our laboratory. Fig. 5.5 illustrates a schematic representation of the latter system. A cell was placed on the sample stage shown in Fig. 5.5 (a). The video microscopy observations were carried out similarly as done at the x-ray beamline. During anodic (600 mV vs SCE) dissolution of the stainless steel foil the thickness of the salt layers was closely monitored through a *NEC* MultiSync 3D monitor, and a JAVELIN JE2362A video camera interfaced with a Metrabyte MV-1 frame grabber that records images from an optical microscope. Video tape recording (SONY SLV-373UC) was performed from initiation to steady state dissolution of metal and during the electrochemical measurements. The video optical microscope system installed in the laboratory is capable of projecting images at magnification up to 200X, where 1 cm on the monitor screen is vertically equivalent to 20 μm in the actual cell. A video graphic printer (SONY UP-850N) was connected as a printing device. The video camera was connected to the frame grabber, placed in a computer, so that the contrast of the images could be adjusted to obtain fine quality of the image on the monitor and image files could be stored in the computer for later use.

5.1.6 Electrochemical Impedance Spectroscopy (EIS) Measurements of Salt Layers

Electrochemical impedance spectroscopy (EIS) measurements were carried out to determine the resistance of the salt layer across the metal interface. A XAS or XRM pit cell with a 0.5 M HCl + 0.5 M NaCl solution were used for the measurements. A schematic diagram was presented in Fig. 5.6. A small AC potential (10 mV) generated from a Solatron 1170 frequency analyzer was superimposed with a DC potential which

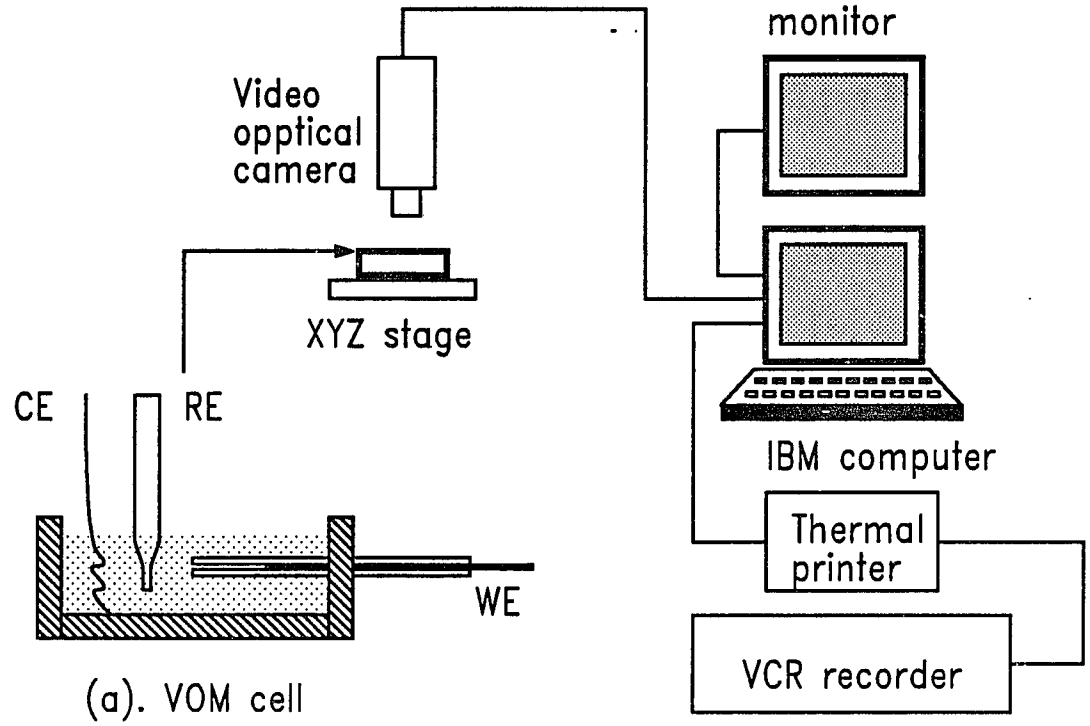

Fig. 5.5. A schematic diagram of video optical microscopy (VOM) instrumentation.

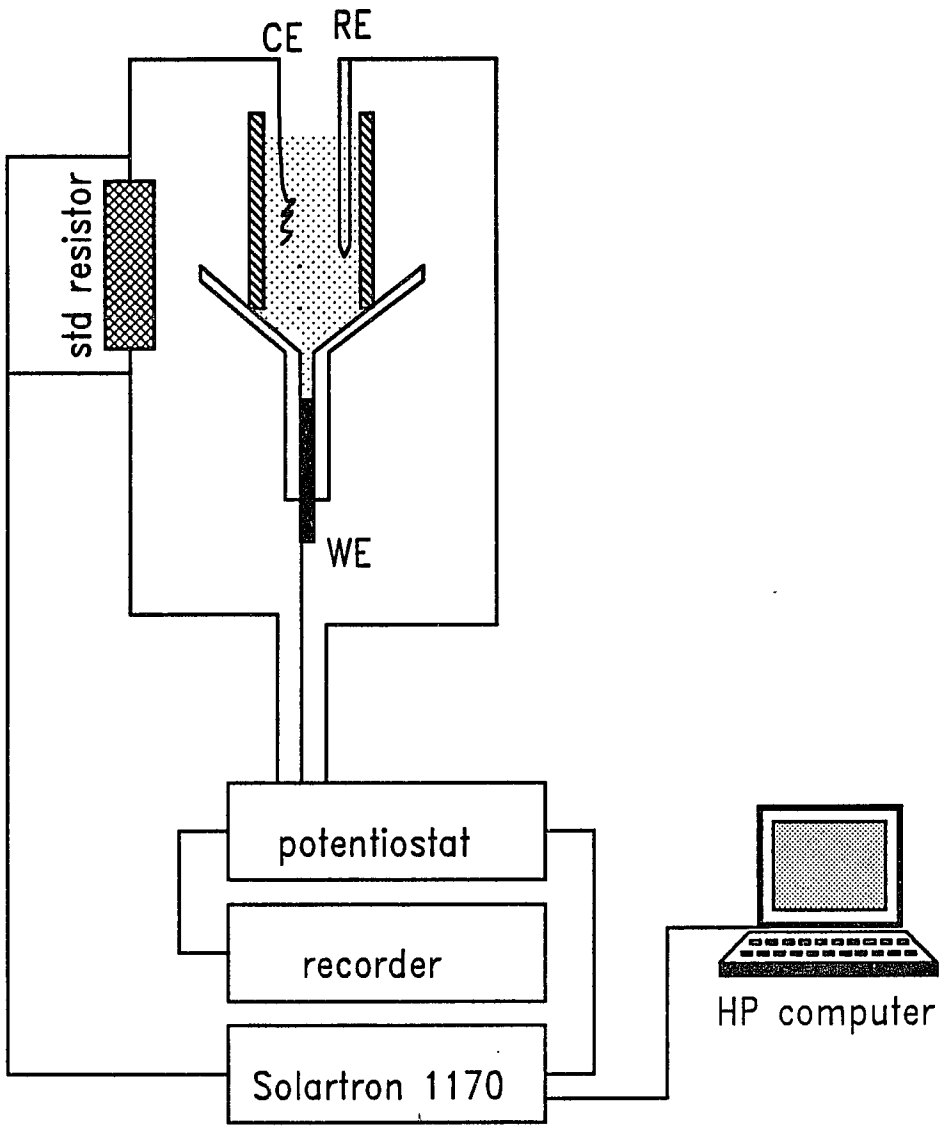

Fig. 5.6. EIS measurement of an artificial pit.

was set by a PAR Model 173 potentiostat. A HP 9836 computer controlled the frequency analyzer to vary the frequency and calculated the AC impedance from the measured AC potential and AC current. A frequency range of 10 ~ 10 kHz was applied in order to obtain an impedance spectrum before dissolution of metal (at the open circuit potential) and during anodic (600 mV vs SCE) dissolution of the metal. The AC impedance, at a given pit depth, was measured with and without the salt layer to subtract solution resistance. The current was continuously monitored throughout the measurements. The measurements were continued until sufficient data were obtained to ascertain the relationship between pit depth (approximately up to 1.5 mm) and the resistance of the salt layer. After reaching a pit depth of approximately 1.5 mm, the potential was varied between 0 and 1000 mV and the AC impedance was measured to obtain the thickness-potential relationship of the salt layer at a fixed pit depth.

5.1.7 Scanning Electron Microscopy (SEM) Investigation of Corrosion Products

Tiny insoluble corrosion products and a gel-like silica band were observed during potentiostatic dissolution of the commercial stainless steel foil in the chloride solution. SEM pictures of these products were taken and EDS analysis was performed after carefully collecting these products. Also the dissolved cross-section of the foils were examined from SEM photographs.

5.2 Signal Transient along Transmission Lines

5.2.1 Interfacial AC Impedance of a Type 304 Stainless Steel Wire

The interfacial AC impedance Z_i of the steel wire in Na_2SO_4 solutions was measured in a frequency range of 1 - 1000 Hz. Fig. 5.7 (a) shows the geometry of the electrochemical cell for the impedance measurements using a short wire of the stainless steel (3 cm long) with a uniform current density. Solution resistance was either calculated from the conductivity data measured with HI 8333 conductivity meter (HANNA Instrument Co.) and the cross-sectional area of the tube (0.352 cm^2), or obtained directly using AC impedance measurements of the cell shown in Fig. 5.7 (b).

The applied DC potential of the system was fixed throughout the impedance measurements using a PAR Model 173 potentiostat. The range of the applied DC potential was between - 100 ~ + 200 mV (vs SCE). The polarization curve and the AC impedances of the short wire electrode, in Na_2SO_4 solutions, showed a very small current in this potential range, indicating passivity of the electrode. Measurements and calculations of the AC impedance were made with a HP 9836 personal computer connected with a Solartron 1170 frequency analyzer.

5.2.2 EIS Measurements along a Passive Wire Electrode

A one-dimensional electrochemical transmission line cell and the equivalent electrical circuit are shown schematically in Fig. 5.8. The apparatus consists of a Type 304 stainless steel wire (0.56 mm in diameter, 130 cm in length) as a working electrode, a counter electrode (Pt wire), a reference electrode and a sensing reference electrode (Ag tip, 1 mm in diameter) placed at a specific point along a narrow plastic tube (6.7 mm in

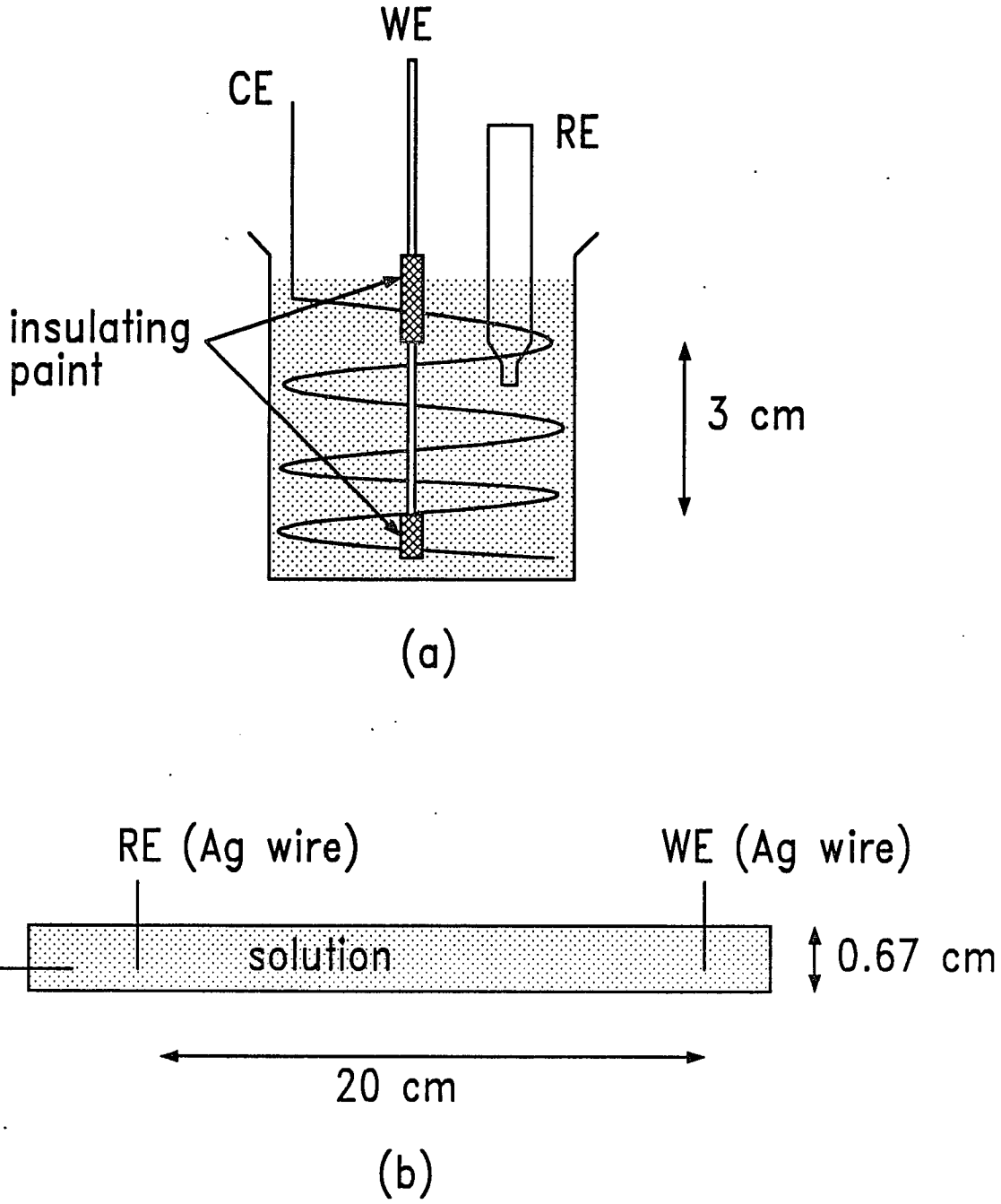

Fig. 5.7. Electrochemical cells for: a) interfacial AC impedance, and b) solution resistance measurements.

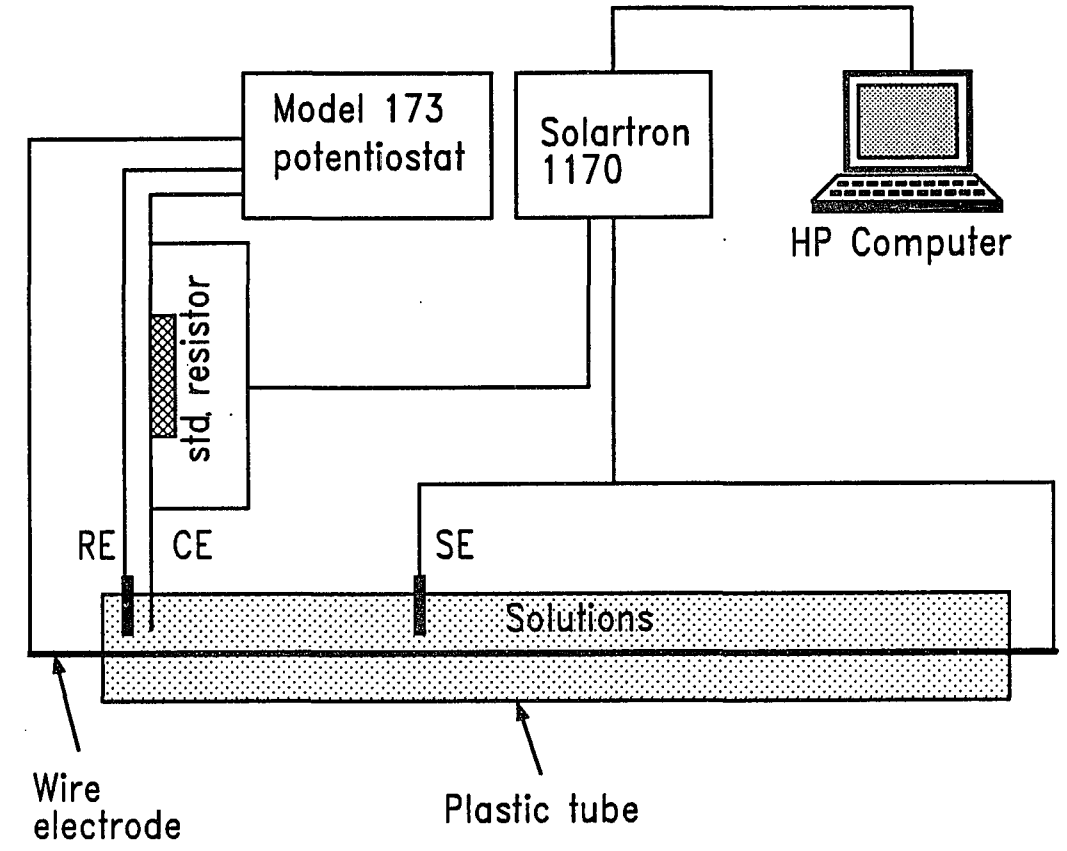

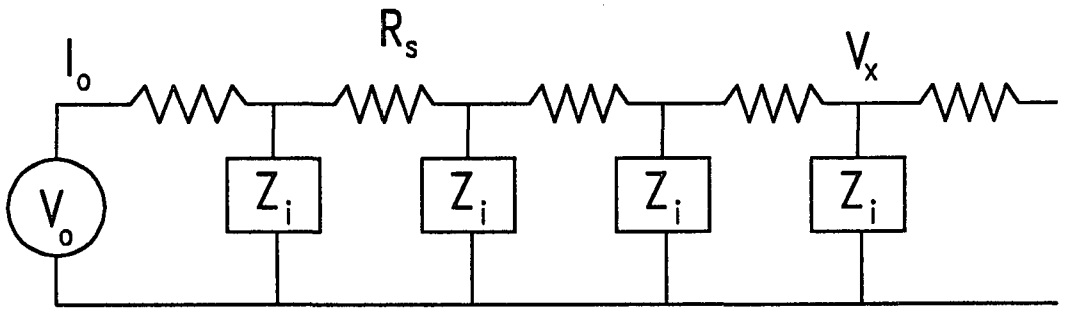

$$V_o = V_{ac} + V_{dc}$$

Fig. 5.8. A one-dimensional transmission line and its equivalent circuit.

diameter). The tube was completely filled with an aqueous solution of 1, 0.1 or 0.01 M Na_2S0_4 with the measured conductivities 80, 15, and 1.8 $mScm^{-1}$ respectively. The wire electrode was abraded to a 600 grit finish and cleaned with acetone, methanol and distilled water before being inserted in the tube. This cell geometry was used both for EIS and pulse transient measurements. The AC potential, V(x), was measured at a given distance along the electrode while the total AC current, I(0), was measured at 0 cm using a standard resistor of 100 ohm connected between the potentiostat and the counter electrode.

5.2.3 EIS measurements of a Passive Wire Electrode in the Presence of a Iron Wire

The apparent impedance of the wire electrode in the tube filled with a 0.55 M NaCl solution was measured at the origin of the tube with a small piece of a iron wire inserted at the distance (4, 9 and 16 cm) from the origin of the tube. The iron piece which was connected to the stainless steel wire simulates a localized corrosion site of the passive wire electrode at a potential of 0 mV (vs Ag/AgCl).

5.2.4 Measurements of Pulse Transients

In order to study the signal response of localized corrosion transients, i.e., potential transients along transmission lines, a rectangular pulse with a very short duration (2 msec and 200 mV in amplitude) was used as a simulated potential transient for localized corrosion transients. The tube was filled with a 0.1 M Na_2SO_4 solution. The pulse was added to a constant potential of 0 mV (vs Ag electrode) at the origin of

the wire electrode. A PAR Model 175 Universal Programmer connected to a PAR Model 173 potentiostat was used to control the potential and to introduce the pulse. The potential responses at the two different positions from the origin were recorded at channels A and B of a Keithley 194A High Speed Voltmeter. A sampling time of 10 μsec/point was selected. A HP 9836 computer collected transient data from the voltmeter.

Chapter 6

RESULTS AND DISCUSSION:

I. *In Situ* Microanalytical Study of Artificial Pits

6.1 Observations Using the Optical Microscope and Scanning Electron Microscope (SEM)

6.1.1 Pit Solution

An artificial pit was formed by dissolution of commercial stainless steel foil in the 0.5 M HCl + 0.5 M NaCl solution at a constant potential of 600 mV (vs SCE). An investigation of the dissolution process of the sandwich type cell was carried out to ensure that the dissolving edge remained parallel to the mouth of the cell and that uniform mass transport controlled the dissolution process. The dissolution process at the early stage of the present investigation was slightly different from the explanation given in the experimental section (Chapter 5). The steel foil was dissolved down to approximately 1 ~ 2 mm deep from the initial foil interface (the pit mouth) in the laboratory and the dissolved area was then ultrasonically cleaned before the XRM pit cell was placed in the sample stage of the beamline X-26A. The foil was redissolved at the beamline and the XRM measurements were carried out after establishing a quasi-steady state of dissolution.

However, it was found, from the optical microscope, that the ultrasonically-

cleaned dissolved area was distinguishable from the dissolved area formed during the XRM measurements. Fig. 6.1 shows the photograph with the three distinct areas, taken through the optical microscope during the XRM experiments. The bottom part of the picture, the black region, is the steel foil. The bright upper part is also the dissolved area obtained as a result of the initial dissolution sequence and the ultrasonic cleaning process in the laboratory. The gray area in the middle is the dissolved area of the foil formed during the XRM measurements. A subsequent analysis of this dissolved area using SEM and EDS showed that the area is mostly filled with Si. The gel was formed from the silicon in the stainless steel (0.5 %wt) which expanded to occupy the volume of the dissolved steel. More distinct effects were observed with iron containing 3% Si because of the six times greater amount of Si. The gel extruded from the cavity as the dissolution proceeded.

Ultrasonic cleaning of the cavity to remove the gel did not produce an observable difference in the fluorescence intensities across the boundary between the first and second dissolution sequences. However, this pre-dissolution process created some hindrance to the diffusion path of the dissolving metal ions and to the XRM measurements. With or without ultrasonic removal of the gel, if the applied potential was turned off for a enough time to allow for the steel interface to repassivate completely, subsequent dissolution often left fragments of the steel under the passive surface that were undermined when the adjacent surface was reactivated.

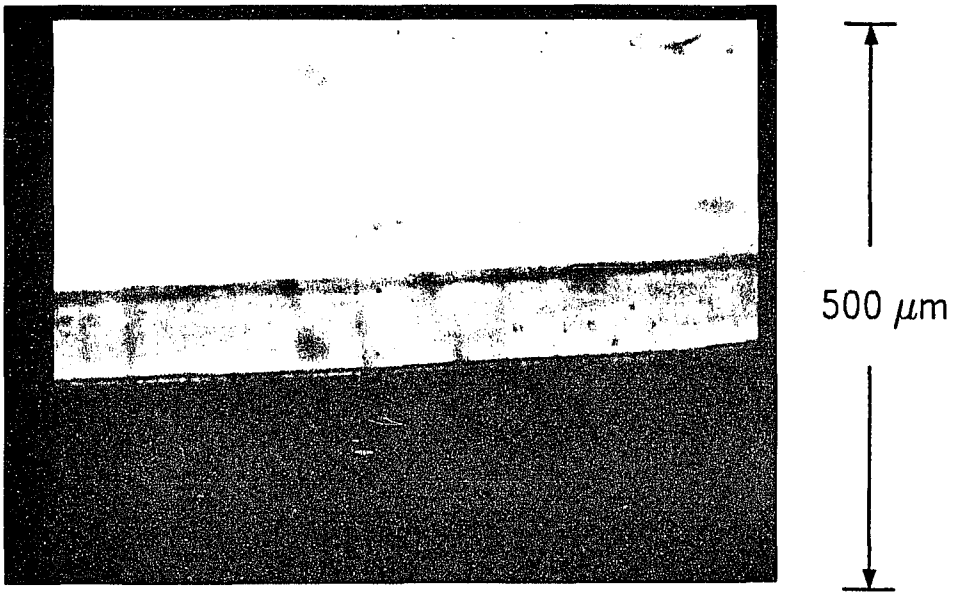

Fig. 6.1. A photograph of an artificial pit taken during dissolution of a commercial stainless steel foil in a 0.5 M HCl + 0.5 M NaCl solution at 600 mV (vs SCE).

Fig. 6.2 shows a microphotograph of the dissolved area of the steel and Fig. 6.3 is the plot of the corresponding current transient during anodic dissolution with a couple of potential interruptions. The potential was turned off for 5 minutes after 30 minutes anodic dissolution (600 mV vs SCE) and the bulk solution was changed during that period. After dissolution, the bulk solution was removed and the dissolved area was gently washed with distilled water. The photograph was then taken with a polaroid camera attached to an optical microscope (Unitron Co.). The bright area in the bottom is the steel foil and the dark portion of the picture in the upper part is the region of the pit mouth. The middle part showing the three strips is the dissolved area of the steel. The strips in the photograph were investigated using SEM with EDS analysis and the results showed that the composition of the strips is the same as that of the steel. The remnants (strips) acted as obstacles to diffusion with major perturbation in the concentration gradients. The XRM measurements were therefore carried out during a single continuous dissolution of the foil.

6.1.2 The Metal/Solution Interface (Salt Layer)

Two different current transients obtained by potential interruption experiments are shown in Fig. 6.4 during anodic dissolution (600 mV vs. SCE) of the stainless steel foil in the acidic chloride solution when the pit depth was approximately 1.5 mm deep. The transient showing no current minimum in Fig. 6.4 (a) was observed when the potential was interrupted for more than a minute. This current transient is analogue to the transient shown in Fig. 6.3 and the experimental conditions between the two transients

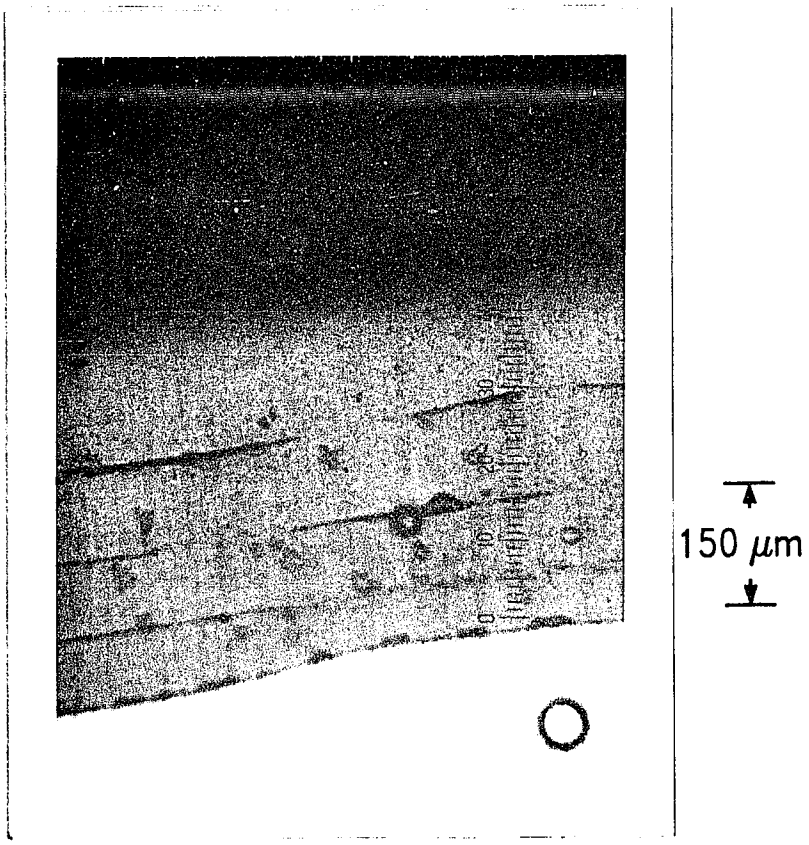

Fig. 6.2. The dissolved area of the steel (see the text for a detailed explanation.

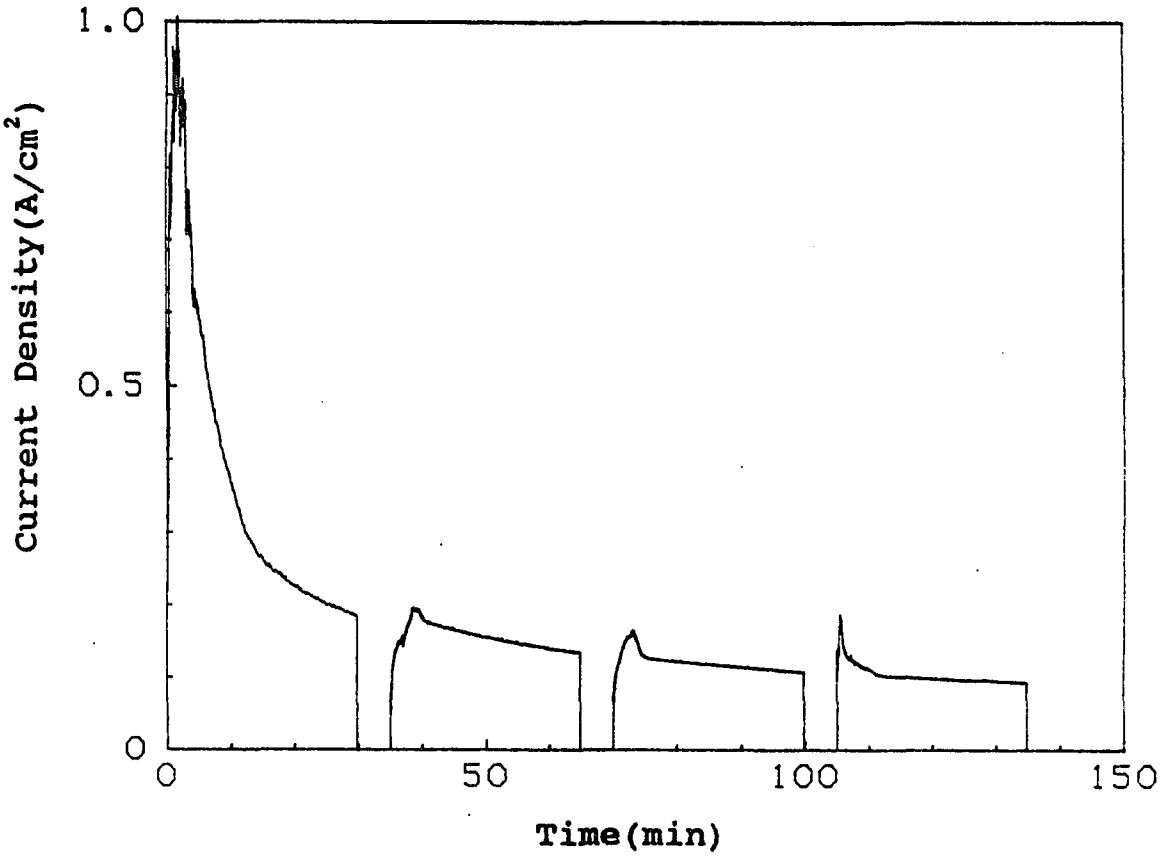

Fig. 6.3. Current transient during anodic dissolution (600 mV vs SCE) of the steel. Zero current indicates the potential was turned off during that period.

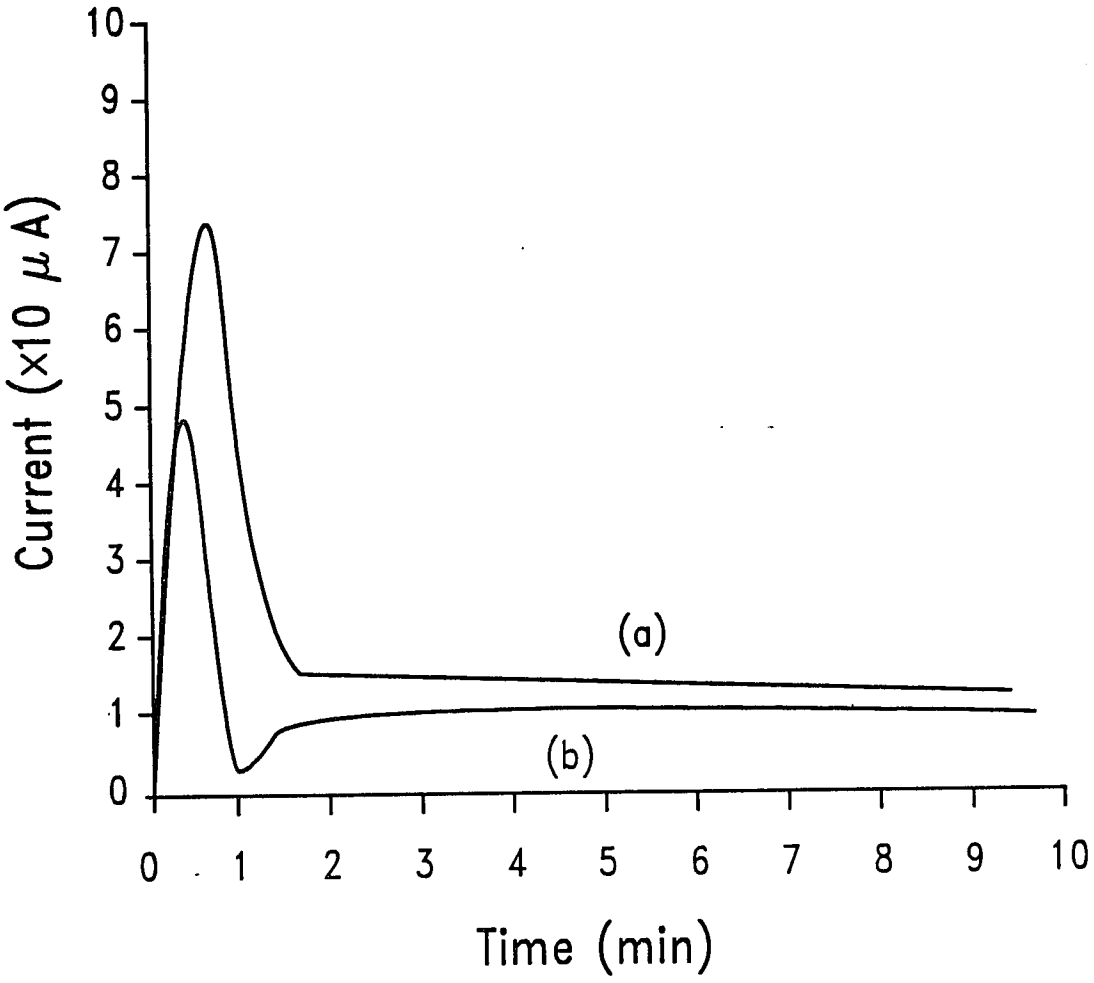

Fig. 6.4. Current transients recorded during potential interruption. Potential was interrupted for (a) more than 60 sec and (b) less than 30 sec.

are similar in terms of the interruption period (more than 1 minute). However, with a short interruption period (less than 30 sec), the current transient appears to have a minimum followed by rapidly decreasing current and then to reach a quasi-steady state value, as shown in Fig. 6.4 (b).

Fig. 6.5 shows a series of microphotographs of the interface taken at the beamline during the XRM measurements. The photographs were obtained from the video camera connected to an optical microscope. It shows the time sequence of the interfacial images changing as potential was interrupted. Fig. 6.5 (a) is the image taken during continuous anodic dissolution at a potential of 600 mV (vs SCE) with a pit depth of 1.5 mm and Fig. 6.5 (b) was obtained after turning off the potential for 5 sec. Still a salt layer remained at the right hand side of the picture. The potential was turned on again to 600 mV (vs SCE) after 5 sec. Fig. 6.5 (c) and (d) are the photographs obtained consecutively at 5 sec and 20 sec, respectively, after potential was turned on again. Fig. 6.6 shows the current transient monitored during the potential interruption period with the indication of the time when the photographs were taken.

It was clearly observed, from a comparison between the *in situ* images and the corresponding current transient, that nucleation of the salt layer was initiated as soon as the current passed the maximum. The crystalline salt precipitates on the metal surface with rapidly growth and spreads to the entire metal surface until the current arrives at its minimum. The salt layer forming at this stage, when a current minimum occurred,

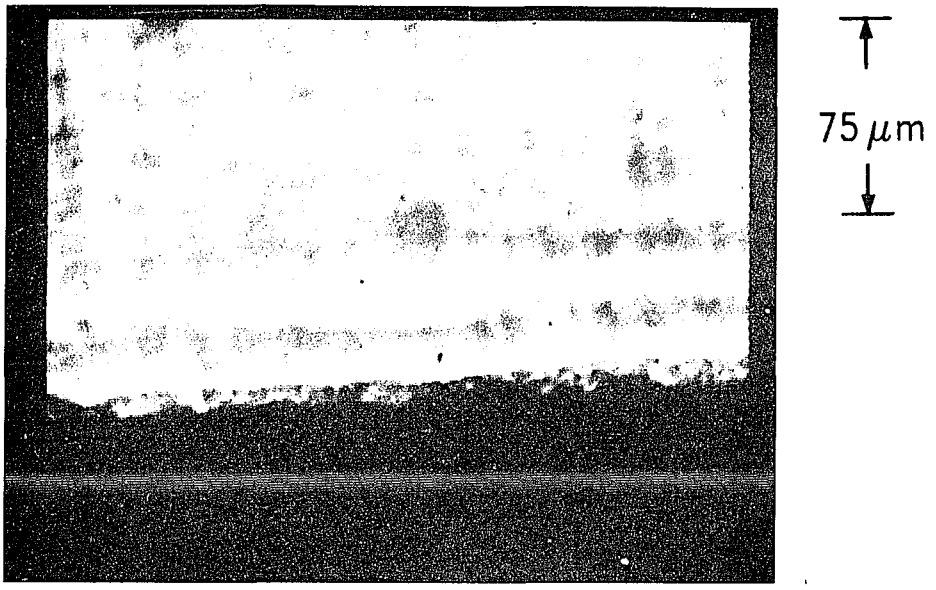

(a)

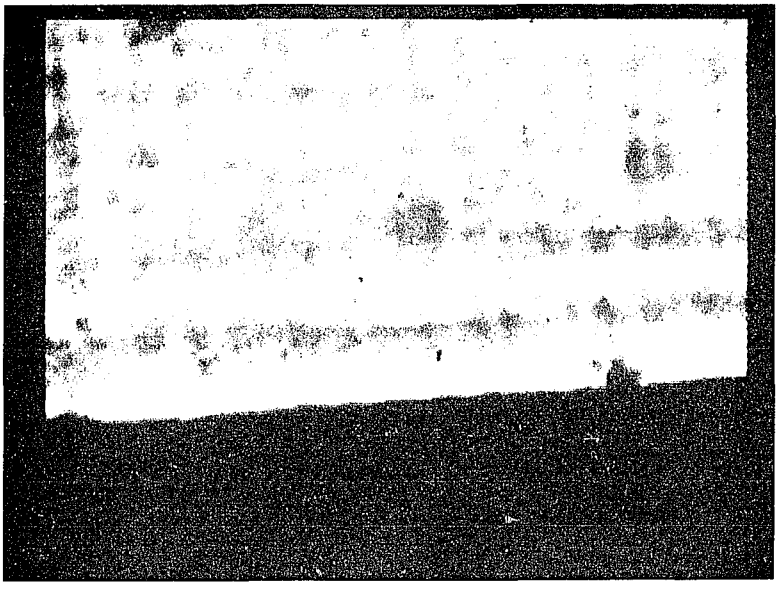

(b)

Fig. 6.5. The time sequence of the interfacial images during potential interruption experiment: (a) before potential interruption and (b) after 5 sec of potential interruption. (continued)

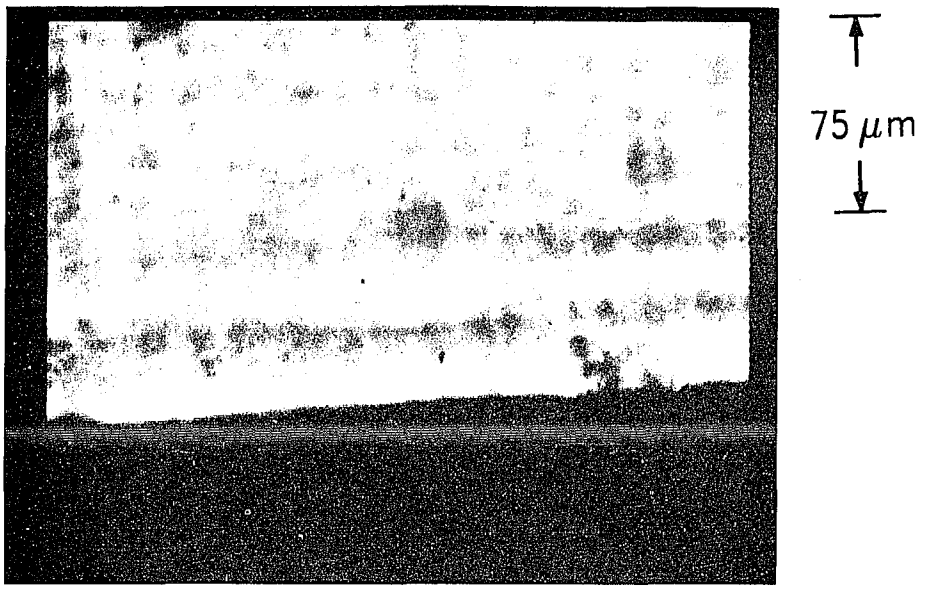

(c)

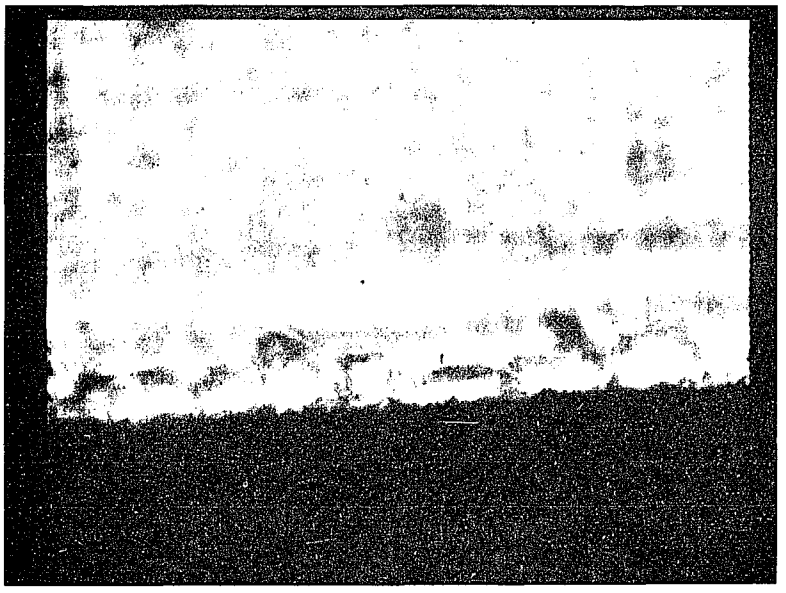

(d)

Fig. 6.5. (c) 5 sec after potential was turned on, and (d) 20 sec after the potential was turned on.

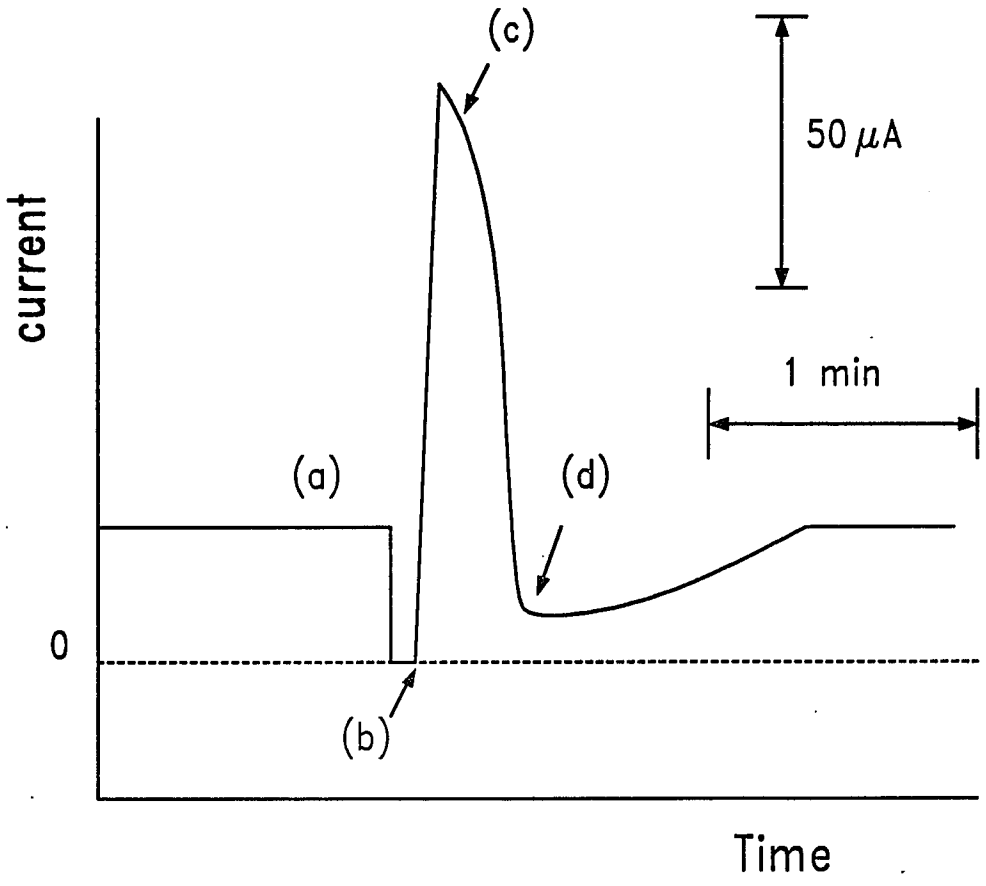

Fig. 6.6. The current transient during the potential interruption period. (a), (b), (c) and (d) indicate when the photographs in Fig. 6.5 were taken.

was crystalline and thicker (about 20 μm) than the salt layer observed during continuous dissolution (less than 10 μm). This crystalline salt (119) decreases the potential gradient at the metal surface, which reduces the rate of metal dissolution, while the diffusion rate in the solution remains constant. As a result, the crystalline salt becomes thinner and smoother, which slowly increases the potential gradient on the metal surface. Finally, the dissolution process stabilizes when a uniform thickness of salt layer is established (101).

Based on the observations from optical microscopy, a probable explanation as to the reason why no current minimum is observed in Fig. 6.4 (a), is as follows: When the potential is turned off, repassivation of the metal surface occurs followed by complete dissolution of the salt layer into the solution, which will be accomplished within a few seconds (121). But the solution near the interface is still aggressive enough to hinder or to delay the repassivation processes. With a long interruption period, a less aggressive solution at the interface will be achieved, which allows the surface to be repassivated completely. Reactivation of the passive metal surface is a non-uniform process (81) and the formation of the salt layer on the whole surface does not occur rapidly and simultaneously. The slow dissolution process with sporadic, microscopic nucleation results in the formation of a reasonably thin salt layer to maintain quasi-steady state dissolution as shown in Fig. 6.5 (a).

The thickness of the salt layer at this stage of dissolution could be measured

directly from the optical microscopy, yet there are some difficulties due to possible artifacts in the images on a TV monitor such as light effects, focusing problems, light scattering and camera resolution which are a main disadvantage of using a video camera with an optical microscope (187). Therefore the exact salt thickness was not determined using video optical microscopy (VOM). However, VOM observation clearly demonstrated that the salt layer is a few μm thick which could be detected by x-ray microprobe techniques.

6.2 *In Situ* X-ray Fluorescence Microscopy (XRM) Measurements

Fig. 6.7 shows a fluorescent spectrum of the solution inside the artificial cavity at 0.05 mm above the metal surface. The spectrum was obtained in the absence of the Kapton thin film deposited with Ti for a real counting time of 600 seconds while the steel foil was dissolved anodically (600 mV vs. SCE). The spectrum shows that the fluorescent peaks of all the elements, except the elements lighter than argon (Cl, O and H), in the sample solution are within the detection limits. The counts under the K_α energy peak for each element (except Cu) were integrated after background correction explained in Chapter 5 and used to determine the concentration of each metal element in the solution at a given position of the cavity. The K_β peak was used for Cu because of the overlap between the Ni K_β and the Cu K_α peaks. The argon peak was from the air. The source of the As and Br could be due to their presence as impurities in the Mylar plastic, the Teflon window or the epoxy glue. Mo and Ti were the minor constituents in the steel. The minor elements and the impurities were only observed after a long

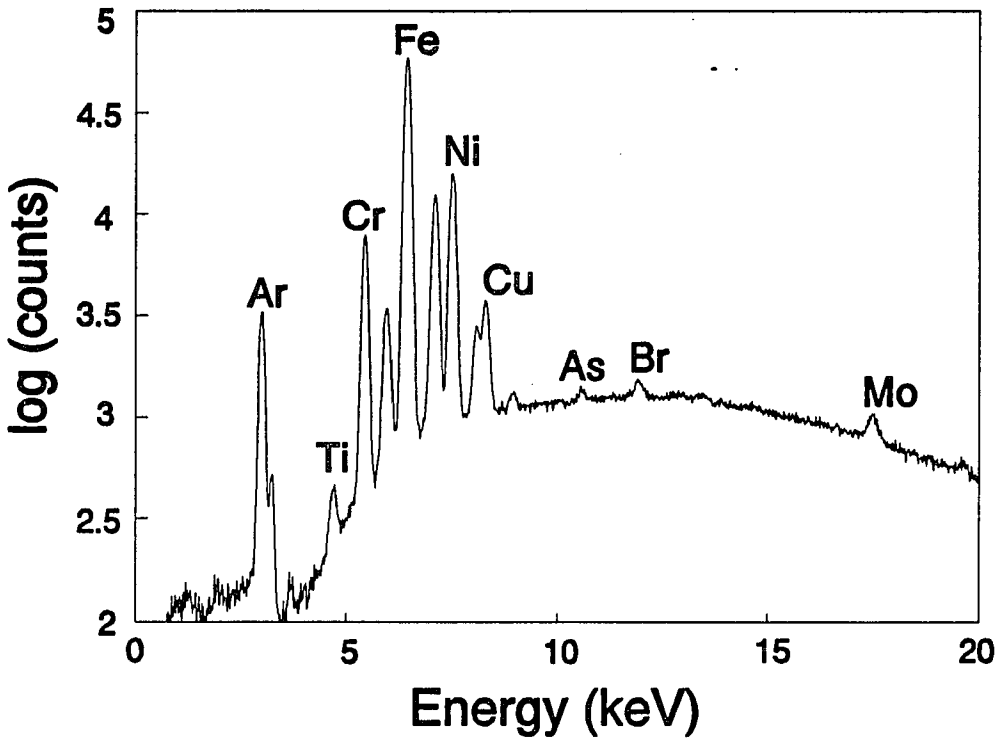

Fig. 6.7. A fluorescence spectrum of the pit solution inside the cavity at 0.05 mm above the foil interface during anodic dissolution.

period of sampling time (600 sec) and were not seen when counting for 30 ~ 60 sec. This does show however the capability of x-ray fluorescence measurement which could be extended to quantitative analysis of trace impurities down to extremely low levels (183).

In the present work, the spectrum was obtained with a 20 μm (2 × radius *r*) x-ray microprobe and the cell thickness (*l*) was 16 μm. The total sample volume that was investigated in this particular spectrum is then $\pi r_2 l = 5.024 \times 10^{-12}\ dm^3$. If the concentration of Mo in the solution was assumed to be 0.001 M (the actual concentration should be lower than this value), the actual amount of Mo in the sample solution is approximately 0.5×10^{-12} *grams*. The fluorescence spectrum shows that such a small quantity is within the detection limits.

6.2.1 Normalization of Fluorescent Intensities

The peak intensities are usually normalized by dividing the fluorescent intensities of the elements by the "live time" and the ring current that might vary during the measurements. However, it was observed that the normalized counts for Fe, Cr and Ni in the steel were not constant during consecutive XRM measurements. This may indicate that the intensity of the x-ray beam after passing the pin-hole is not proportional to the ring current. This could be due to misalignment between the pin-hole and the motorized slits (4-jaw slits) which initially collimate the SR x-ray beam to a size of approximately $100 \times 100\ \mu m^2$, or due to thermal expansion of the slits.

Alternatively, the fluorescent intensities can be normalized to the Ar count. Since the amount of Ar in air is constant, any change in live time, beam intensity and energy distribution of the beam will be reflected in the Ar intensity. However the Ar intensities measured during scans appeared to be very noisy and the Ar-normalized intensities of the metal elements in the steel often showed fluctuations in the energy distribution of the incident x-ray beam.

A third method to normalize the peak intensities was attempted by using Ti as a reference element. A thin Ti film ($\sim$ 500 Å) deposited on Kapton plastic (200 μm) was placed in front of the XRM cell. This method turned out to be the most effective and reliable normalization method. The Ti intensities during the XRM measurements were stable and the normalized fluorescent intensities of metal elements in the steel were constant. The Ti-normalized fluorescent intensities of the metal elements as a function of distance from the steel/solution interface are plotted in Fig. 6.8. A "real time" and a step size were chosen at 40 sec and 50 μm, respectively.

One possible disadvantage of the method is in that the Ti K-absorption edge is 4.964 and the Cr K_α value is 5.414 KeV. A small portion of the Cr K_α fluorescence x-rays will be absorbed by Ti, a process which results in lower Cr intensities than those found without the Ti film. Therefore the sensitivity to Cr in the measurement is slightly diminished when using Ti as a normalizing element. However the effect of Ti presence on Cr fluorescent intensities can be quantitatively estimated by the fundamental

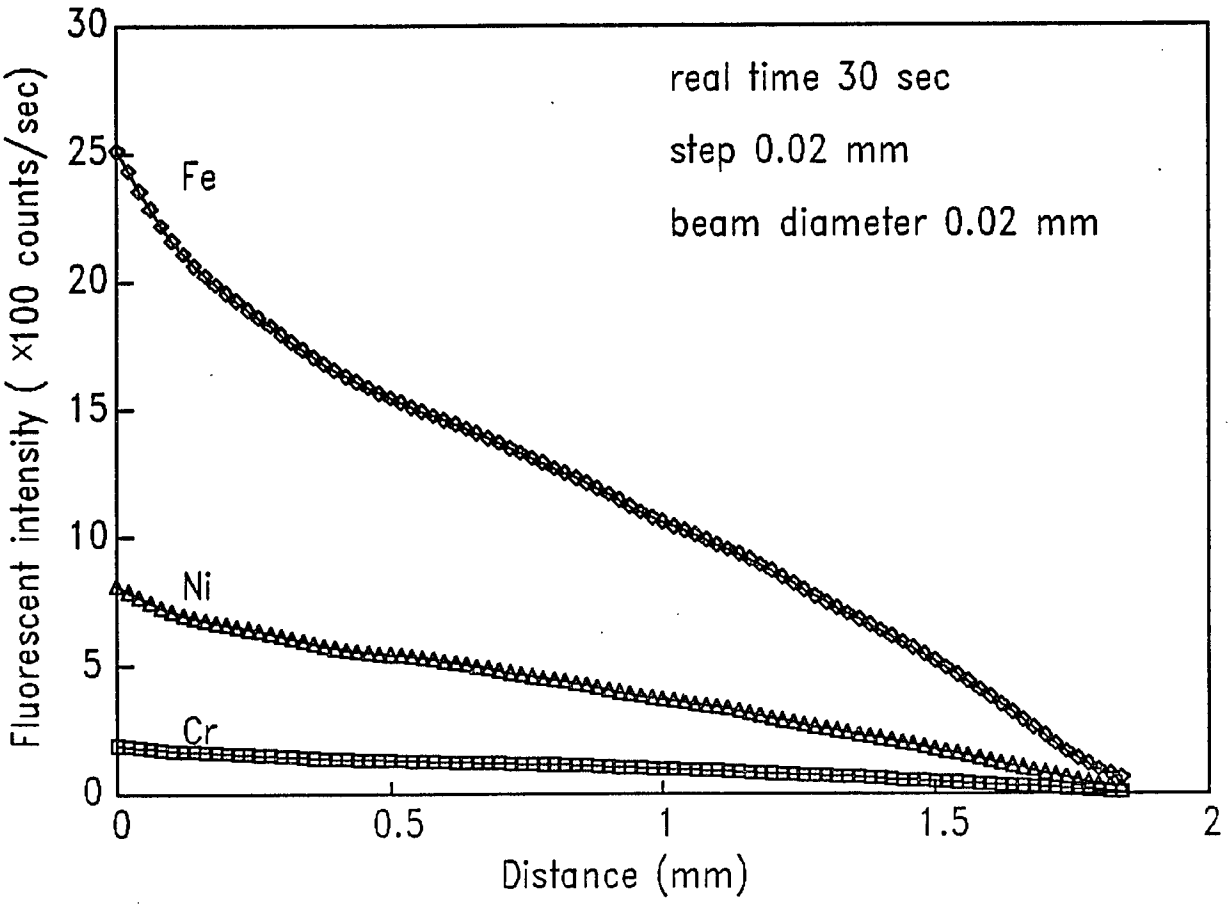

Fig. 6.8. A plot of normalized intensities vs distance from the steel surface. Intensities were taken at a pit depth of 1.8 mm during dissolution of the steel at 600 mV (vs SCE).

parameters method as discussed in Chapter 4 (166,168). The Ti-normalized intensities were then corrected against the cell thickness. Variation of the cell thickness was investigated by the scan along the cavity filled with a 0.5 M $NiCl_2$ + 0.8 M $CrCl_3$ standard solution. Variation of the fluorescent intensities less than 10 % within the cavity were attributed to thickness variations, as shown in Fig. 6.9.

6.2.2 Concentration Gradients of Pit Solution

Determination of the concentrations for each metal ion at a given position of the artificial cavity was made through calculations using a modified "NRLXRF" program (168) with the fundamental parameters method described in Chapter 4. The program requires various input parameters for complete calculations, such as the relative or normalized fluorescence counts for the elements of interest (Fe, Ni and Cr) in a standard, in unknown samples and the approximate compositions of the other elements (Cl, O and H), whose fluorescence counts were not measurable.

The concentrations of Fe, Cr and Ni were calculated for each position along the artificial pit based on the thickness-corrected Ti-normalized fluorescent intensity of each ion in the steel (whose composition is known) and in the solution (unknown). Fig. 6.10 shows the concentration variation of each metal element as a function of distance from the metal surface. The saturated salt concentration obtained from the present x-ray fluorescence microprobe analysis was ~ 4.7 M for total metal ions ($FeCl_2 \approx 3.15$ M, $CrCl_3 \approx 1.06$ M and $NiCl_2 \approx 0.50$ M). The chloride concentration deduced from these

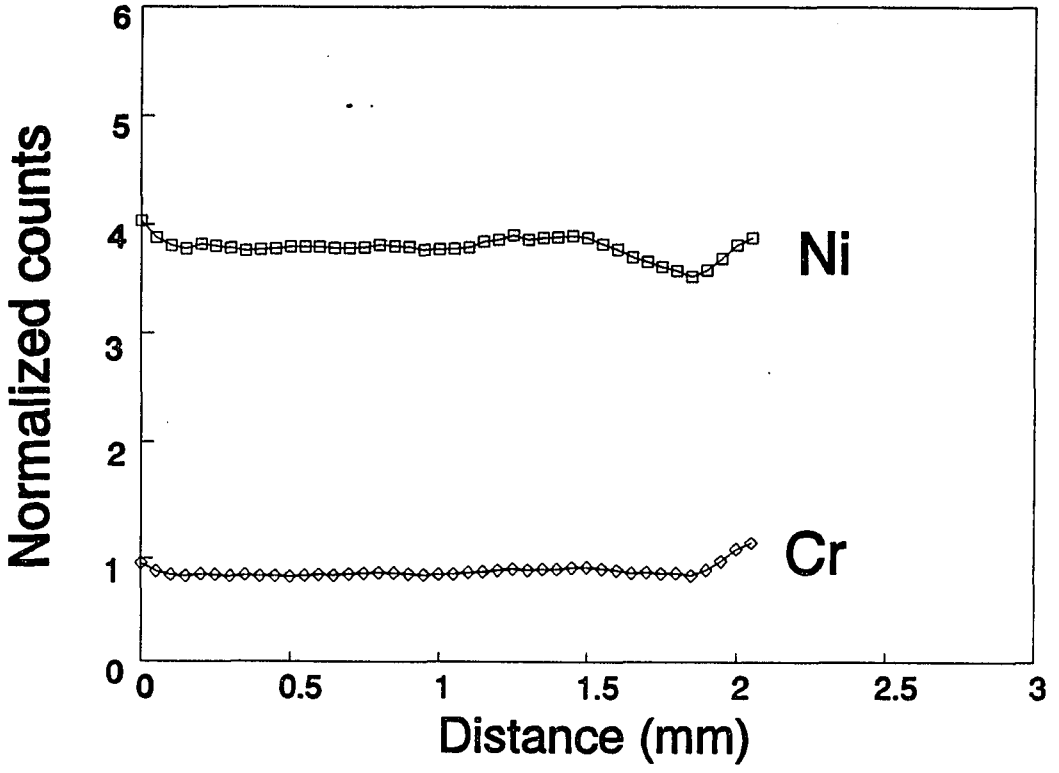

Fig. 6.9. A plot of normalized intensity vs beam position along the cavity formed by dissolution of the steel.

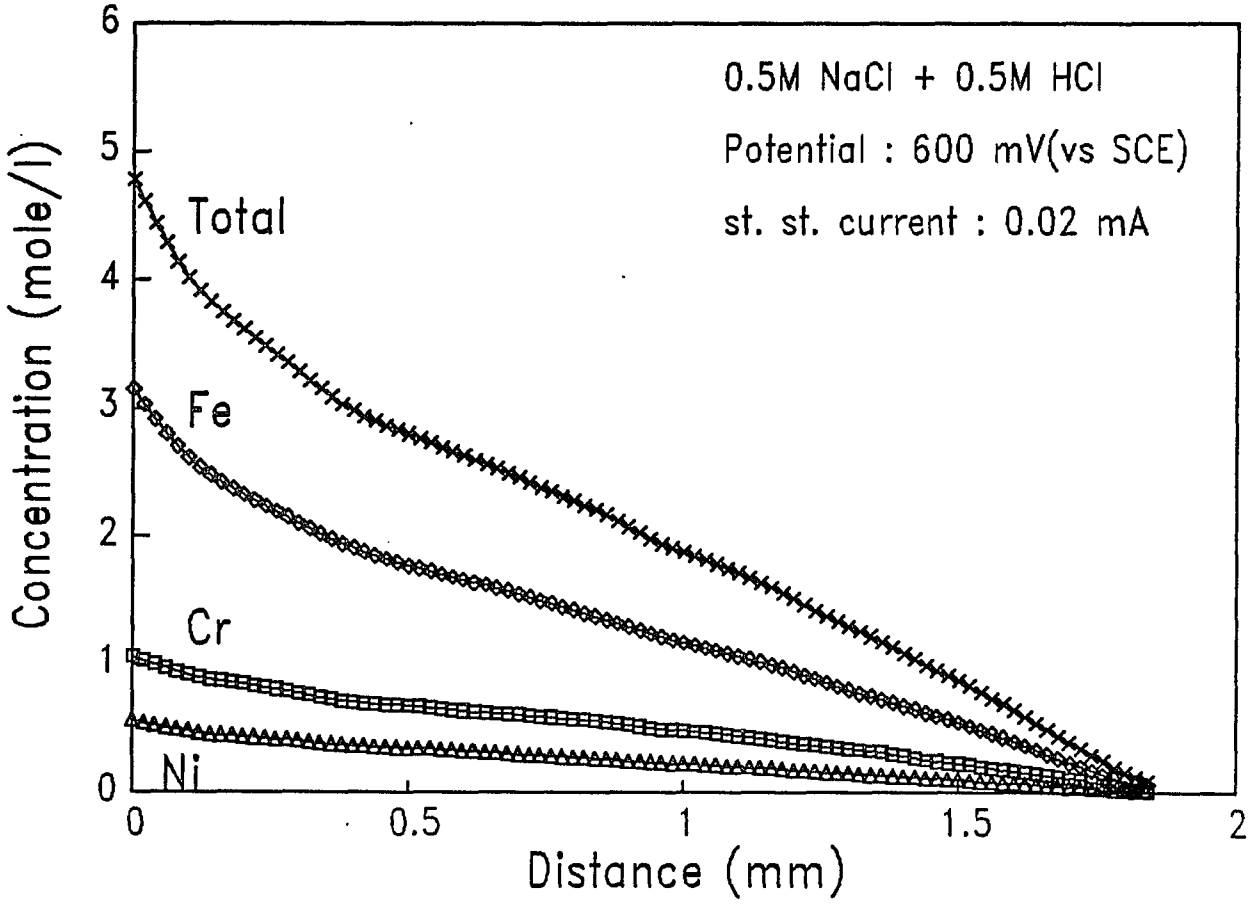

Fig. 6.10. Concentration gradients of metal ions inside the cavity. Concentration were calculated based on the experimental data and the fundamental parameters method.

results was approximately 10.6 M. The relative weight % of Fe : Cr : Ni for this concentrated solution was 67 : 22 : 11, which differ from the composition in the steel (68.7 : 18.2 : 13.1). The saturated concentrations of the $FeCl_2$, $CrCl_3$, and $NiCl_2$ salt in aqueous solution with the above ratios were not found in the literature. However, Hakkarainen (6) observed that approximately 10 M of chloride ions were contained in a saturated metal chloride solution formed by dissolving a Type 304 stainless steel in a concentrated HCl solution. Distinct changes in the gradients of each metal ion are apparent at high concentrations and close to the dissolving steel. The increased slopes are a consequence of an increased viscosity of the concentrated solution, of a decrease in diffusion coefficients or mobility of the ions. Variation of the gradients also suggests formation of metal-chloride complexes.

The corresponding current density recorded during the scan was 28.8 mA/cm^2 at a pit depth of 1.8 mm. The calculated current densities using Eqs. [1-8] and [1-9], the diffusion coefficients from the literature (constant for all concentrations) (79) and the concentration gradients of each ion determined from the XRM measurements were between 25 ~ 90 mA/cm^2. The calculation ignored the migration current, i.e., we assumed $d\phi/dx = 0$, and possible metal-chloride complexes. Table 6-I presents diffusion coefficients and concentration gradients which were used in the calculations. The calculated values of the current densities should be constant along the pit depth, but the calculations shows variation in the values. The results also shows deviation from the observed current density values. The major reason for the apparent discrepancy should

Table 6-I. The diffusion coefficients and the concentration gradients used to calculate current densities.

Element	Diffusion coefficient[1] (10^{-5} cm^2/sec)	dc/dx[2] (M/cm)
Fe	0.72	0.51 - 0.11
Ni	0.71	0.08 - 0.02
Cr	0.59	0.13 - 0.03

(1) From reference 79.

(2) From the results of this work.

be from the use of constant diffusion coefficient values. The calculation should use the diffusion coefficient that varies with concentration, yet the data for highly concentrated mixture of metal chloride solutions are not available in the literature.

In this work, correction of the diffusion coefficient as a function of concentration was attempted from the concentration gradients determined from the XRM measurements. First, the potential gradient was still ignored and any deviation in the calculated current density from the observed value was assumed to be due to variation in the constant diffusion coefficients in Table 6-I. It was also assumed that the constants of all metal ions vary with concentration at the same rates. Table 6-II presents the corrected diffusion coefficients at various total metal concentrations. Stokes *et al.* (188) reported the diffusion coefficients of Ni^{2+} and $NiCl_2$ as a function of aqueous nickel chloride concentration. Fig. 6.11 is a plot of the diffusion coefficients, based on Stokes *et al* (188) and our calculated results as a function of total metal chloride concentration. The line in the middle was calculated from the literature values (188) by assuming that 50 % Ni^{2+} + 50 % $NiCl_2$ complex are contained in nickel chloride solutions. In the region of low concentration ($\leq$ 1 M), most iron and nickel ions do not appreciably form complexes with chloride ions. The region of moderate concentration (1 M - 3 M) shows that the degree of the complex formation increases with concentration and reaches a maximum value at a total concentration of 3 M. For very high concentration (3.5 M $\leq$), the degree of the complex formation is approximately constant at 50 % which well agrees with observations in the literature (95,96).

Table 6-II. Corrected diffusion coefficients of each metal ion at various total metal concentrations.

	Diffusion coefficient (10^{-5} cm^2/sec)		
Concentration(M)	Fe	Ni	Cr
0.5	0.590	0.582	0.483
1.0	0.646	0.638	0.530
1.5	0.671	0.661	0.550
2.0	0.796	0.785	0.652
2.5	0.798	0.787	0.654
3.0	0.730	0.720	0.600
3.5	0.439	0.433	0.360
4.0	0.324	0.320	0.265
4.5	0.235	0.231	0.192

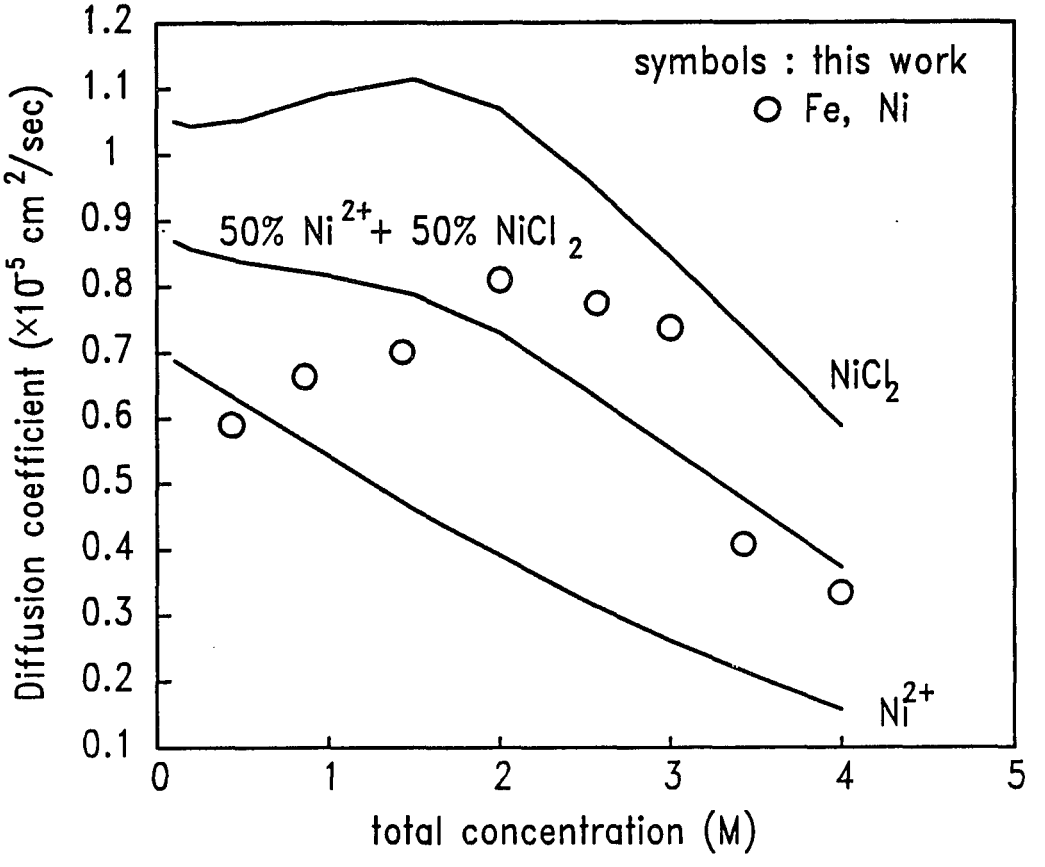

Fig. 6.11. Diffusion coefficient vs concentration. Lines are from Ref 188 and symbols are obtained from the present work.

Fig. 6.12 shows the relative weight fraction of each metal ion as a function of distance from the steel surface. The weight fractions of Fe and Ni decrease as the distance increases while the weight fraction of Cr increases with the distance. This phenomenon could be due to the difference in diffusion coefficients of metal ionic species. It suggests that the dissolved Cr species diffuse more slowly than the Fe and Ni species. Therefore, the higher ratio of Cr in the solution is not from selective or preferential dissolution of Cr which is not expected in dissolution of stainless steels (92-94), but due to slow diffusion rates.

In conclusion, x-ray fluorescence spectroscopy using the SR x-ray microprobe is a powerful *in situ* technique for investigating the solution inside the artificial cavity formed by dissolution of metal. The analysis of the XRM data along the pit solution yields quantitative concentration gradients for the metal species in the pit solutions. The results can be compared with theoretical results and could contribute to development of a better model calculation. Also, the results present important information on the metal-chloride complexes and the diffusion coefficients of the elements in the complex solution of aqueous metal chloride mixtures.

6.2.3 Salt Layer

The salt layer was observed with the optical microscope when the artificial pit was deeper than approximately 500 μm. The thickness of the layer was about a few μm for

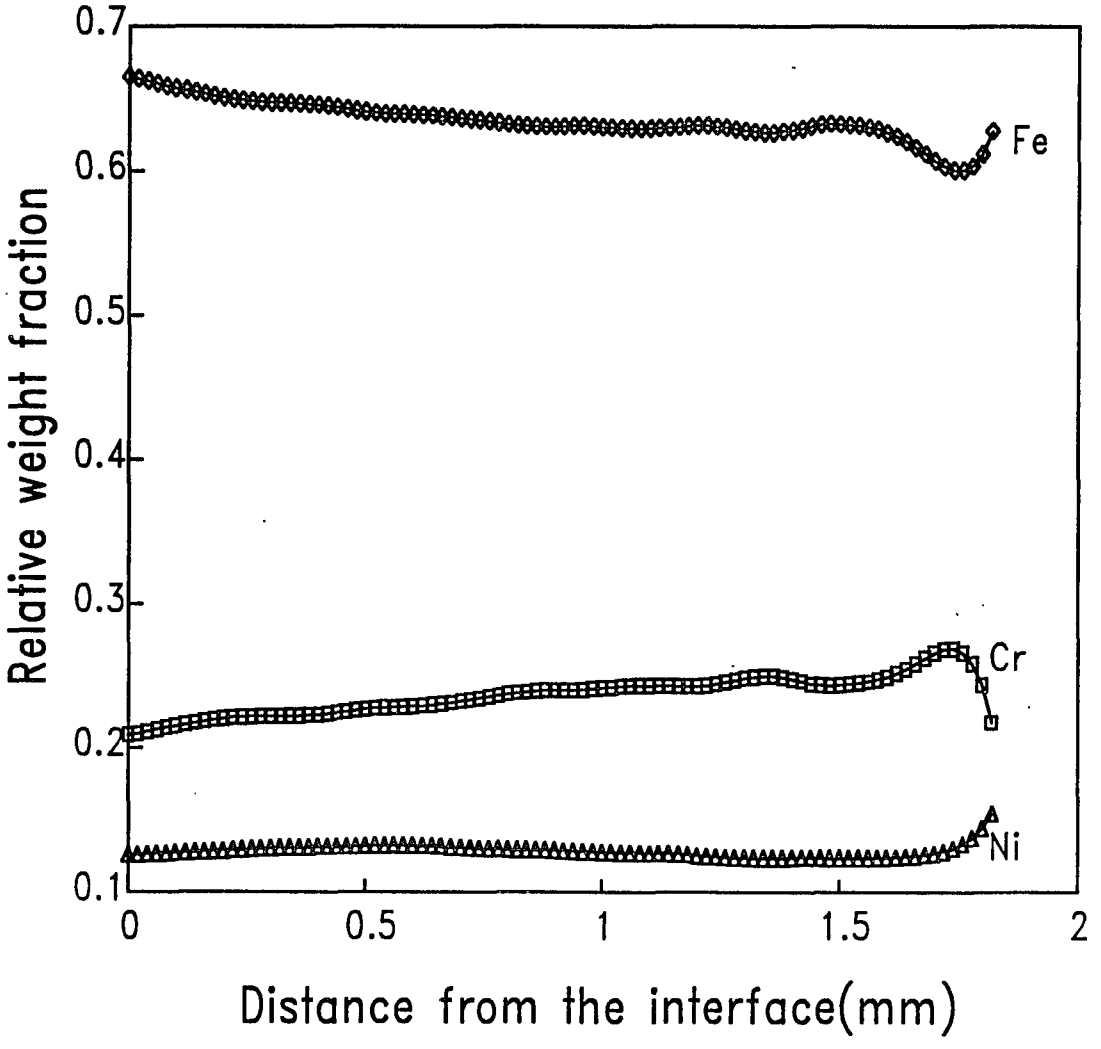

Fig. 6.12. Relative weight fraction of the metal elements along the cavity.

a pit with 500 μm deep and increased with the pit depth. In the present work, the fluorescent intensities of iron, chromium and nickel across the metal interface were compared when the pit depth reached approximately 1.6 mm, which allows us to estimate relative composition of salt layer at the given pit depth and the applied potential.

Fine scans (2 μm in step size) with a x-ray microprobe of 8 μm in diameter were carried out across the salt layer that was present at the metal/solution interface during anodic dissolution. A real counting time was chosen as 20 sec. Fig. 6.13 shows the ratios of the fluorescent intensities among the elements (Fe, Cr and Ni) as a function of beam position (a) with and (b) without the presence of the salt layer at a pit depth of 1.6 mm. Fig. 6.13 (a) was obtained from the scan when continuous dissolution of the steel foil was taking place at a constant potential of 600 mV (vs SCE). At the end of the scan, the potential was turned off and another scan was immediately started. Fig. 6.13 (b) was then obtained from the second scan. While carrying out the second scan, the optical microscope observation showed no salt layer at the interface.

Table 6-III gives the ratios of the fluorescent intensities for each metal ion in the saturated solution and the steel, determined by the x-ray microprobe measurements. The higher ratios of Fe/Cr and Ni/Cr in the solution than in the steel, indicates that Fe and Ni fluorescent x-rays are absorbed more at the steel site because of the higher density of the steel. The opposite trend for Fe/Ni ratio was observed, i.e., the Fe/Ni ratio was higher in the steel, which shows more absorption of Ni fluorescent x-rays at the steel

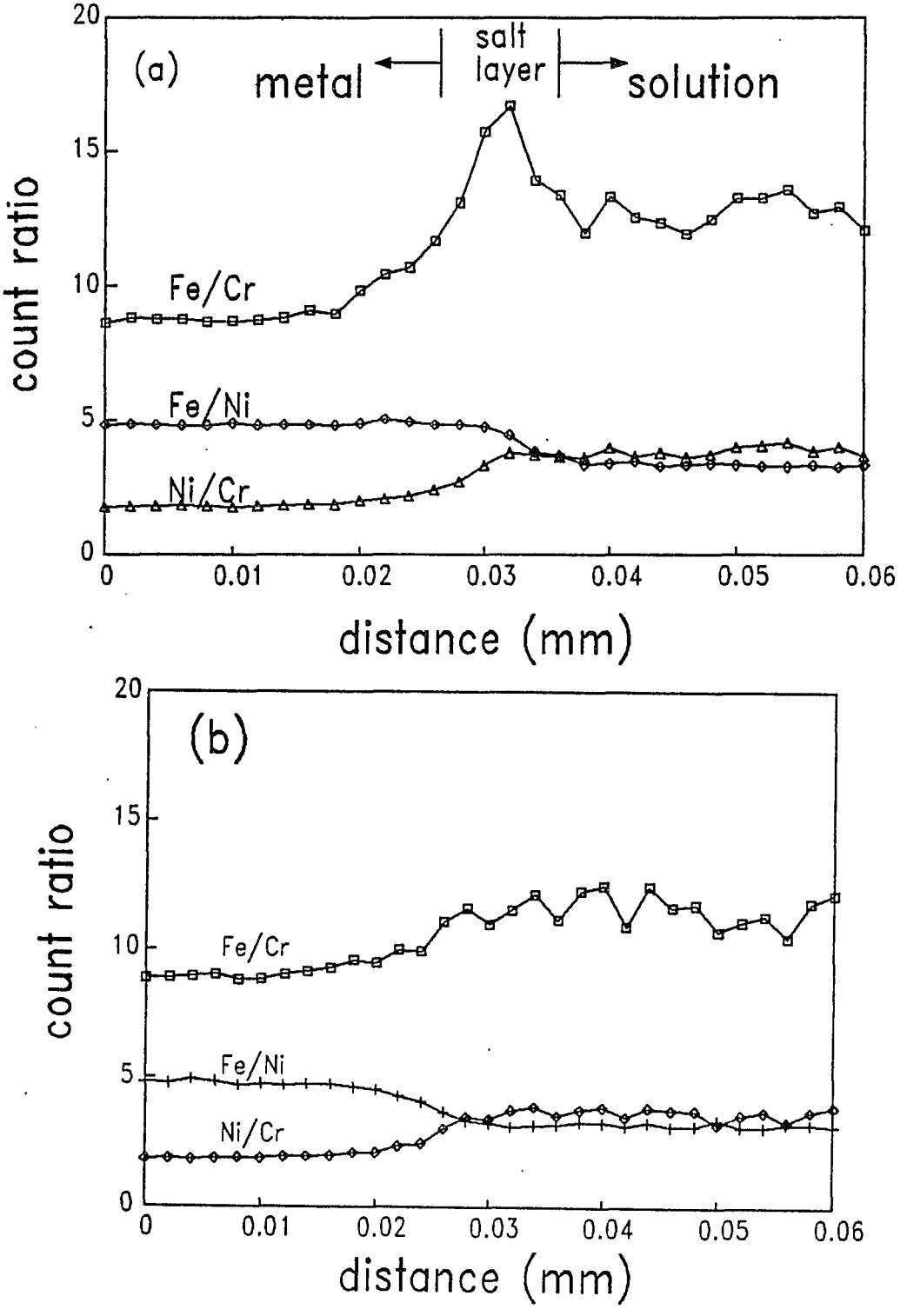

Fig. 6.13. Intensities ratio in metal elements as a function of beam position: (a) in the presence of salt layer (600 mV vs SCE and (b) in the absence of the salt layer.

Table 6-III. Intensity ratios of the metal species in the steel and the solution sides determined from the XRM measurements.

	Fluorescent intensity ratio	
Element ratio	Stainless steel	Solution
Fe/Cr	10	13.5
Fe/Ni	4.6	3.3
Ni/Cr	1.9	4.8

site. The differences in the ratios between the steel and the solution do not result from the difference in chemical composition, but rather are due to the differences in the densities between the sample mediums. The calculation with a modified "NRLXRF" program showed that the Fe/Cr ratio would be approximately 10 and 14 for the steel and the saturated solution (5 M in total metal concentration), respectively, if the relative metal compositions of both elements are the same.

In Fig. 6.13, the peaks in the Fe/Cr and Fe/Ni intensity ratios indicate that the chemical composition of the interface differs either from the steel or the solution. The peak was only observed with continuous dissolution when the salt layer is present at the interface. However, the peaks were not clearly distinguishable until the pit depth reached approximately 1 mm, and the maximum values of the peaks increased with the pit depth and the applied potential. The foil was continuously dissolved at a potential of 600 mV until the pit depth reached approximately 1.6 mm. Then the potential was changed between 200 mV and 1.0 V and the XRM measurements were carried out in order to investigate the potential dependency of the salt layer. The current fluctuated slightly up or down as the potential varied, but soon after it returned to the previous value. Fig. 6.14 shows the Ti-normalized fluorescent intensities of iron species obtained for a "real time" counting of 20 seconds during the consecutive fine scans (2 μm in step size) across the interface for the different applied potentials between 200 mV and 1 V at a pit depth of approximately 1.6 mm. The sequence of potential change was 800 mV, 1 V, 600 mV, 400 mV, 200 mV and then turned off.

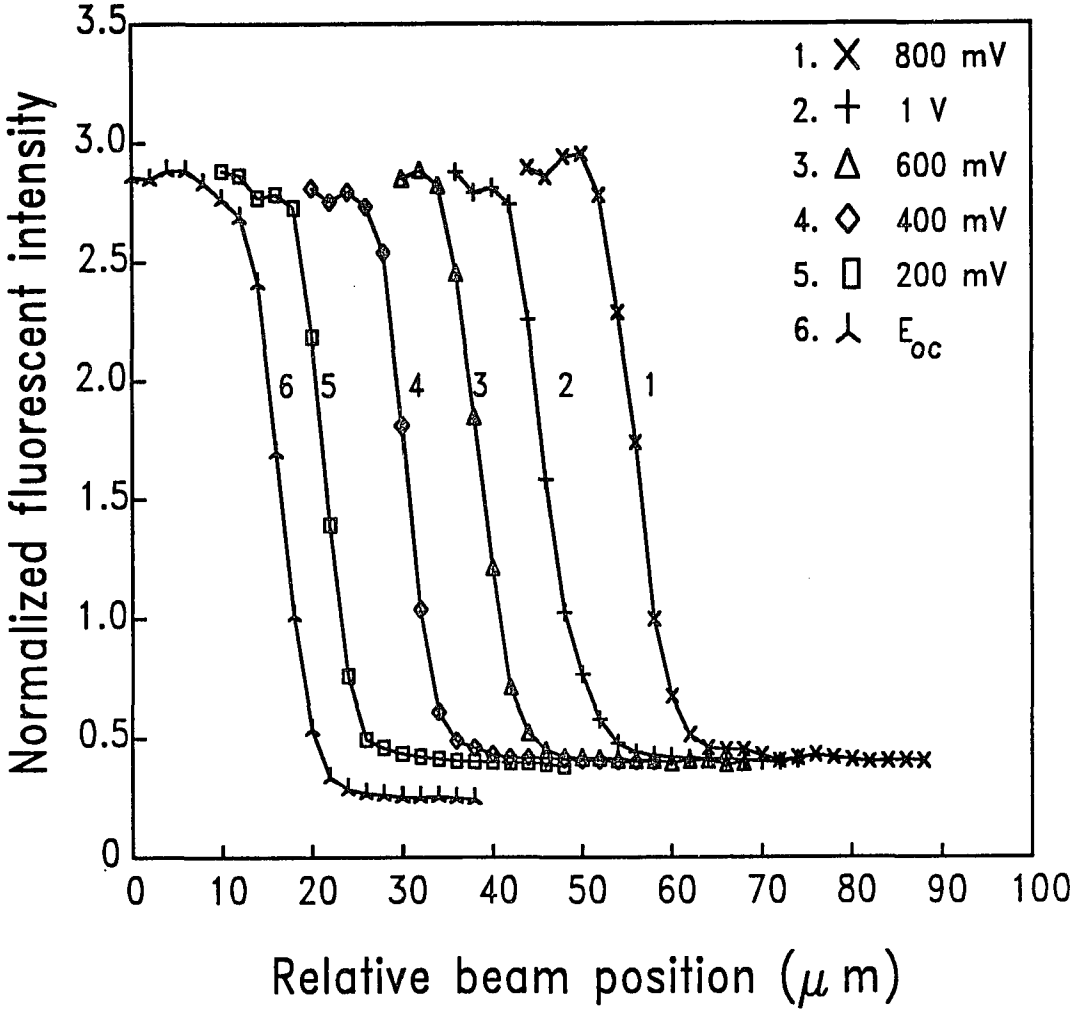

Fig. 6.14. The normalized Fe fluorescent intensities obtained from the consecutive fine scans across the steel interface at a pit depth of 1.6 mm with different potentials.

There was a 2 minute interval between the scans, which was necessary for the current to be stabilized. Scans 2, 3 and 5 involved 20 data points; and scans 1 and 4 involved 23 and 25 data points, respectively. The interface shifted due to the continuous dissolution, at a rate of 0.01 μm/sec, equivalent to less than a 3 % change in the pit depth during the 5 scans. The shift of the metal interface shows the potential dependency of the dissolution rate. The largest shift of the interface was observed when the potential changed from 800 mV to 1 V. This was due to both the time interval between the scans and dissolution of the excess metal ions which participated thereby thickening the salt layer. The 6th scan (the last one) was carried out after turning off the potential. The level of the Fe intensity of this scan in the solution side is lower than the other scans, which indicates that dissolution of the steel had ceased and the iron species had diffused away from the metal surface.

6.2.4 Quantitative Analysis of the Chemical Composition of Salt Layer

Fig. 6.15 and 6.16 give the Fe/Cr ratio and Fe/Ni ratios as a function of beam position relative to the middle of the intensity drop in Fig. 6.14, at different potentials (200 mV - 1 V). Both figures show that the maximum values of the ratios (Fe/ Cr and Fe/Ni) increased with potential. Fig. 6.17 shows the maximum values of the Fe/Cr ratios increase as the applied potential increases.

Quantitative analysis of the XRM data was carried out with the fundamental

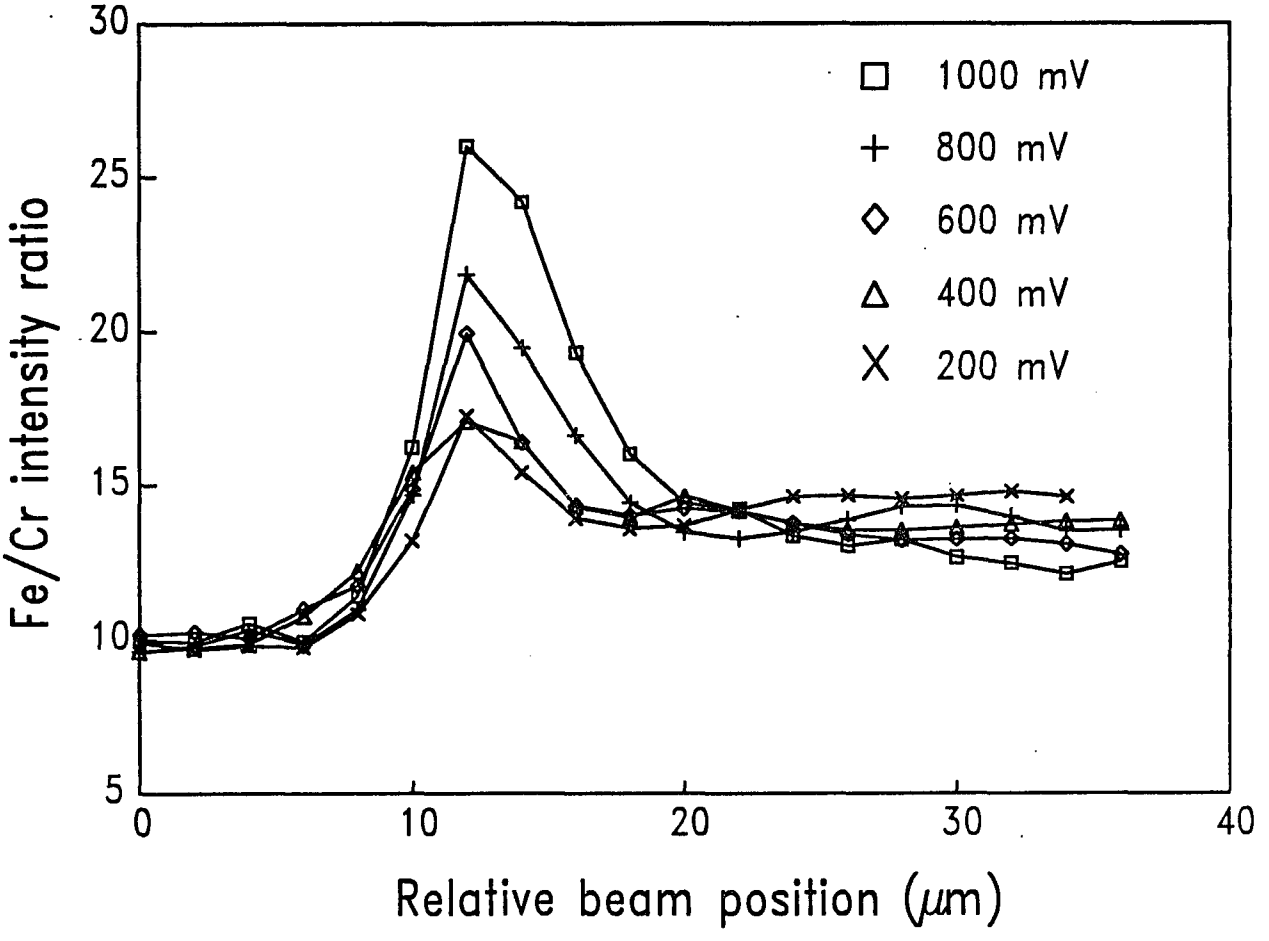

Fig. 6.15. Fe/Cr ratio as a function of beam position.

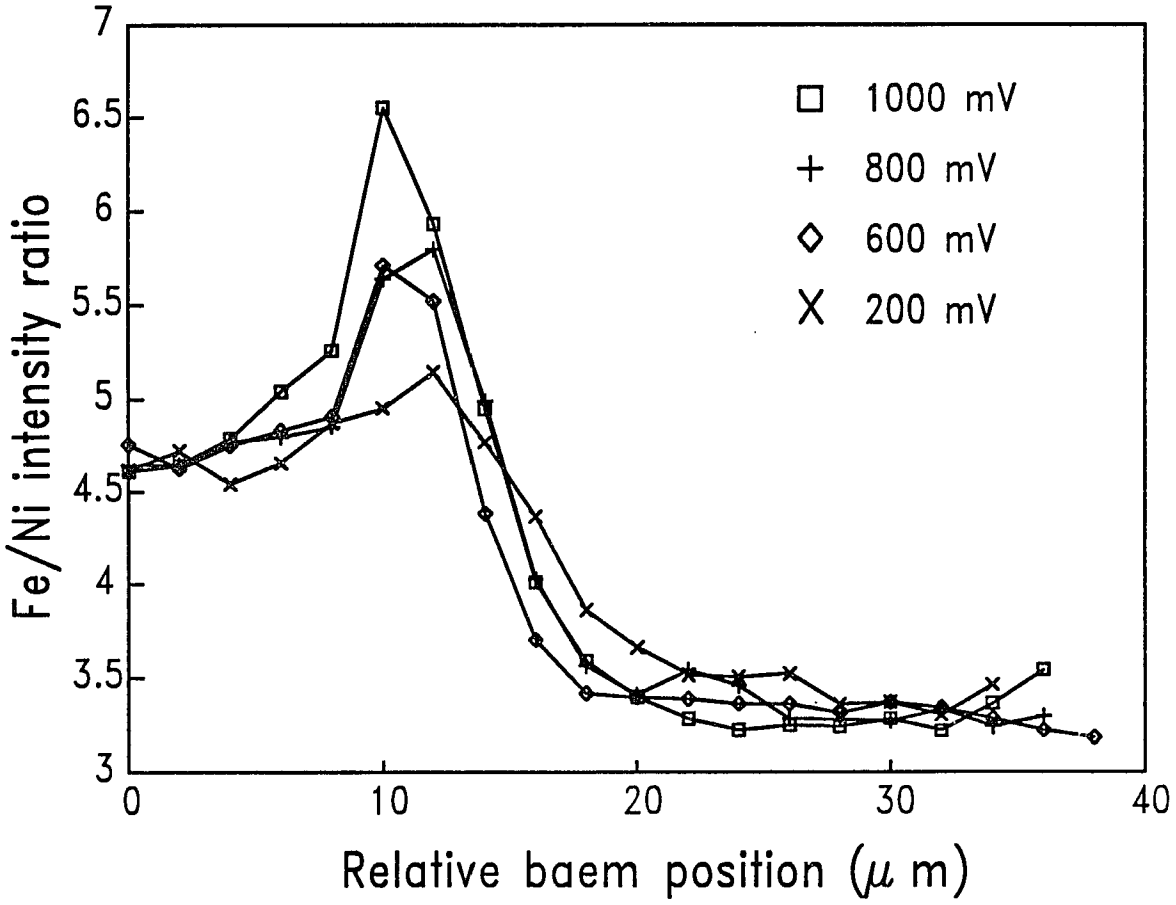

Fig. 6.16. Fe/Ni ratio as a function of beam position.

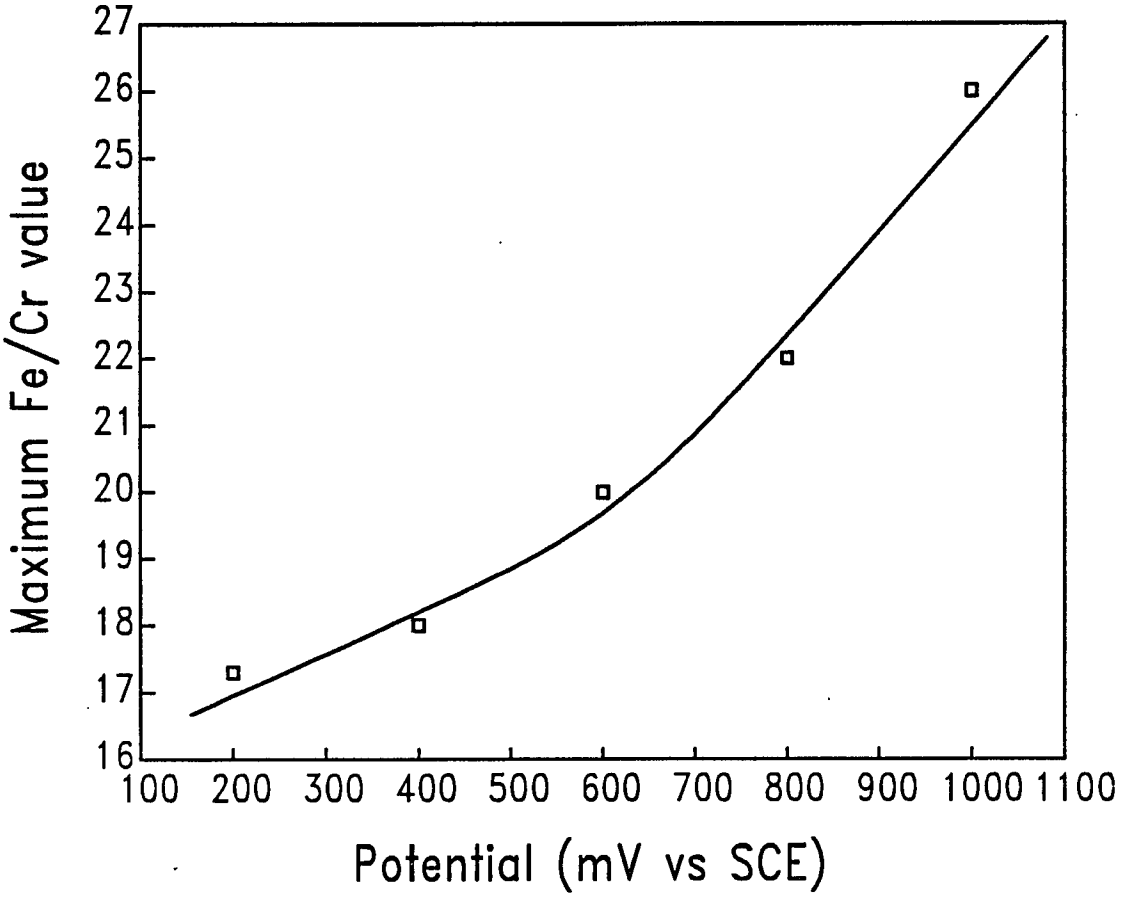

Fig. 6.17. The maximum values of Fe/Cr ratio as a function of potential.

parameters method and curve fitting. First, a simple geometry of the cell near the metal/solution interface was modeled as shown in Fig. 6.18 (a). Fig. 6.18 (b) shows the relative fluorescent intensities of each side (steel, salt and solution). The intensities in the steel and the solution sides were adopted from the experimental results. The intensities of the metal elements in the salt were calculated based on the fundamental parameters method. The chemical formulas assumed for each metal-chloride solid salt were: $FeCl_2 \cdot 4H_2O$, $CrCl_3 \cdot 4H_2O$ and $NiCl_2 \cdot 4H_2O$. The ratio of the metal-chloride solid salts was arbitrarily changed (but $FeCl_2 \cdot 4H_2O$ was always greater than 50 %) and the intensities were calculated for the different compositions of the solid salt mixture. A total concentration of the solid salt varied with the composition of the salt, over a range of 9.5 ~ 9.8 M. The same water content was used for all metal chlorides solid salts because $FeCl_2 \cdot 4H_2O$ is the dominating constituent among the mixture of metal chlorides solid salts and the structure of the solid mixture is a single phase (189). Fig. 6.18 (c) shows the beam profile, which indicates the relative fraction of the beam. The beam profile was deduced from the first derivative of the normalized Fe intensities obtained from the scan across the interface and was shown to have an effective size of 12 μm in diameter (202). This beam size was obtained when a 8 μm pin-hole was used to collimate the beam.

The above three parameters, i.e., the geometry, the fluorescent intensities and the beam profile, were employed to calculate the theoretical fluorescent intensities of the metal elements as the beam moves along the interface. Then the theoretical intensities

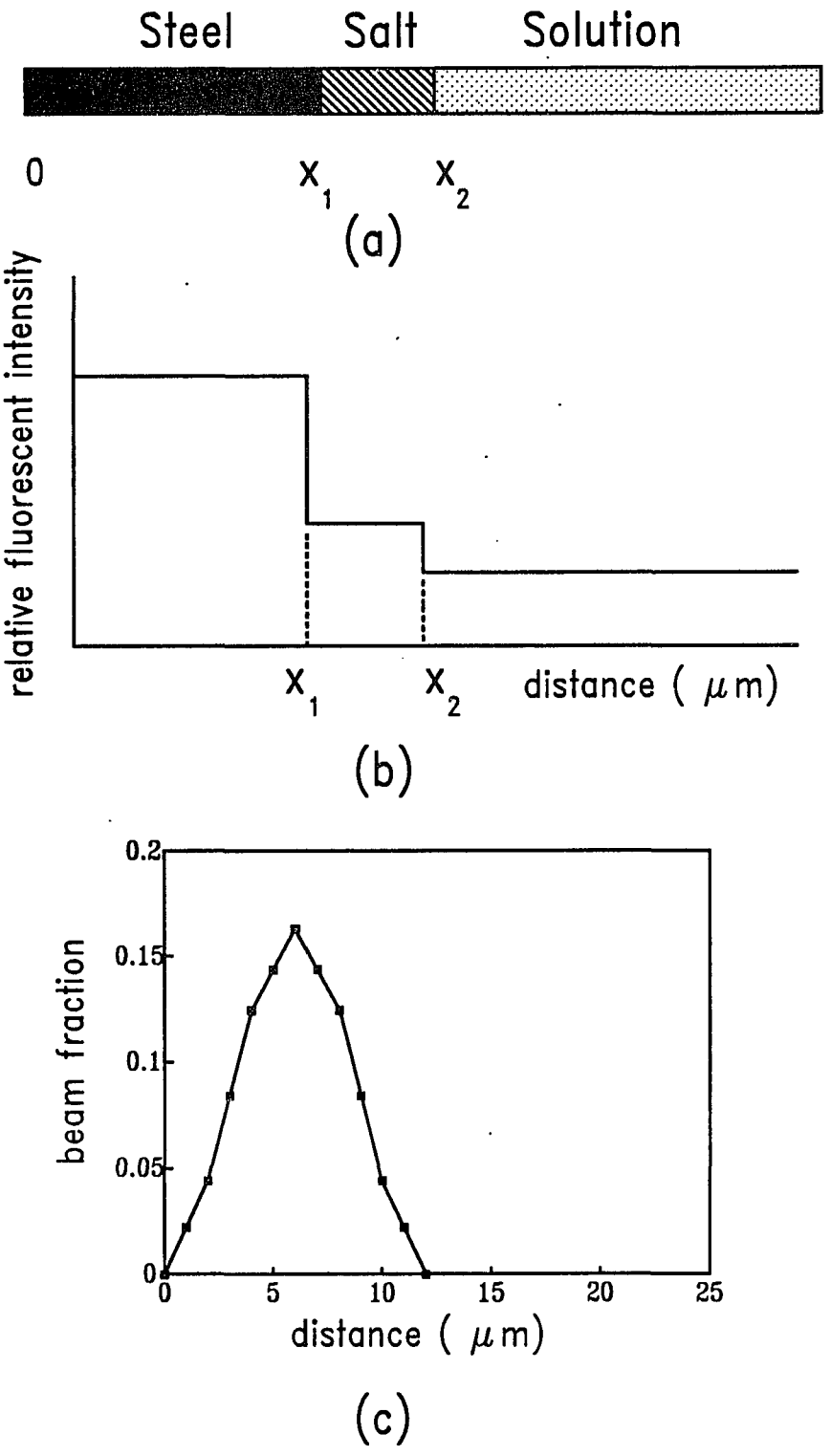

Fig. 6.18. A model for quantitative analysis of the salt layer.

of each metal element and the ratios of the intensities were compared with the experimental results.

Fig. 6.19 and 6.20 show the best-fit results for the intensities of each element and their ratios, respectively. The experimental intensities designated by symbols in the figures were from the second scan at a potential of 1 V (vs SCE). The best fit was achieved when a salt thickness of 6 μm and a total salt concentration of 9.65 M with the ratio of the salts being $FeCl_2 \cdot 4H_2O$: $CrCl_3 \cdot 4H_2O$: $NiCl_2 \cdot 4H_2O$ = 0.88 : 0.06 : 0.06 (in weight fraction) were used. The best fit results for the data obtained at the different potentials were obtained by changing the salt thickness, i.e., decreasing the salt thickness with decreasing potential. As discussed in the previous section, the beam was stepped 2 μm per 20 sec from the steel to the solution while the interface moved to the other direction due to continuous dissolution, at a rate of 0.01 μm/sec. Therefore practical step size of the beam relative to the interface would be 2.2 μm per 20 sec and the 6 μm thick salt was then corrected to 6.6 μm. Fig. 6.21 is a plot of the salt thickness determined as a function of potential, after correction for the step size.

The resistance of the salt layers were also investigated using Electrochemical Impedance Spectroscopy (EIS) at a pit depth of approximately 1.5 mm. Fig. 6.22 showed the resistivity of the salt layer as a function of potential. It was founded from the impedance measurements that the resistive salt layer is presented at the metal/solution interface and that the resistance of the salt layer increases linearly with the applied potential.

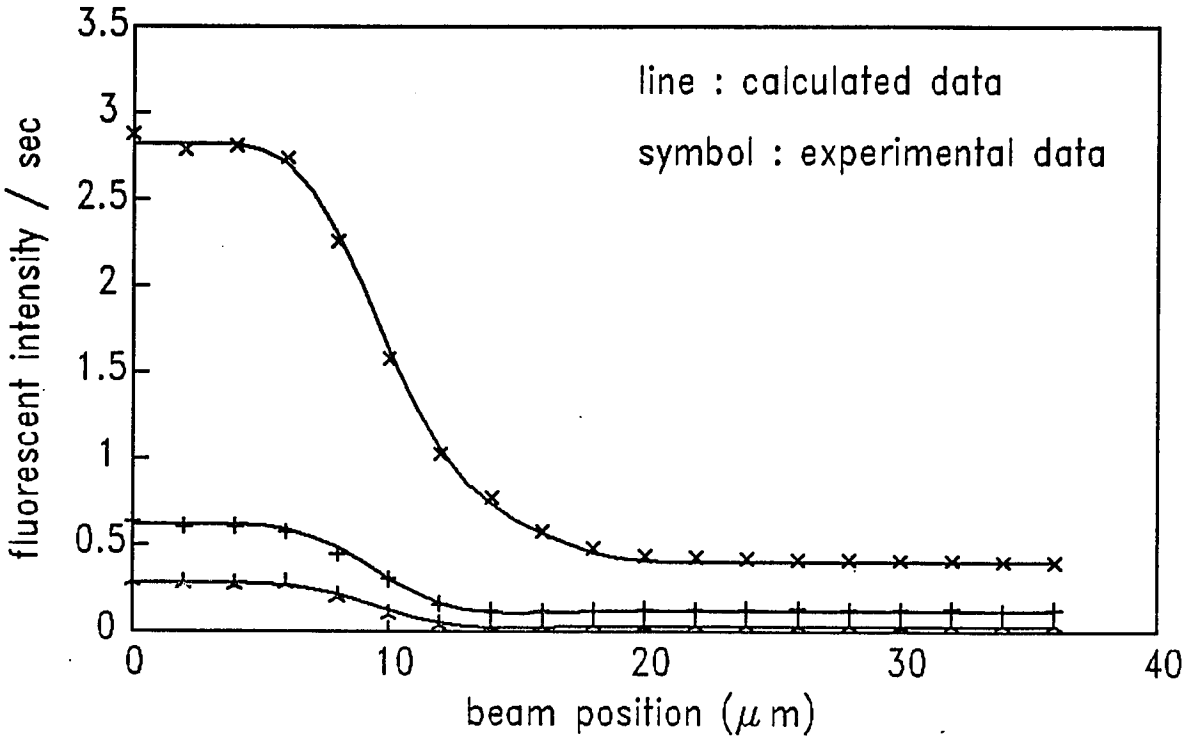

Fig. 6.19. Comparison between the best-fit calculated and measured fluorescent intensities across the interface. The measured intensities were obtained from the scan at 1 V (vs SCE).

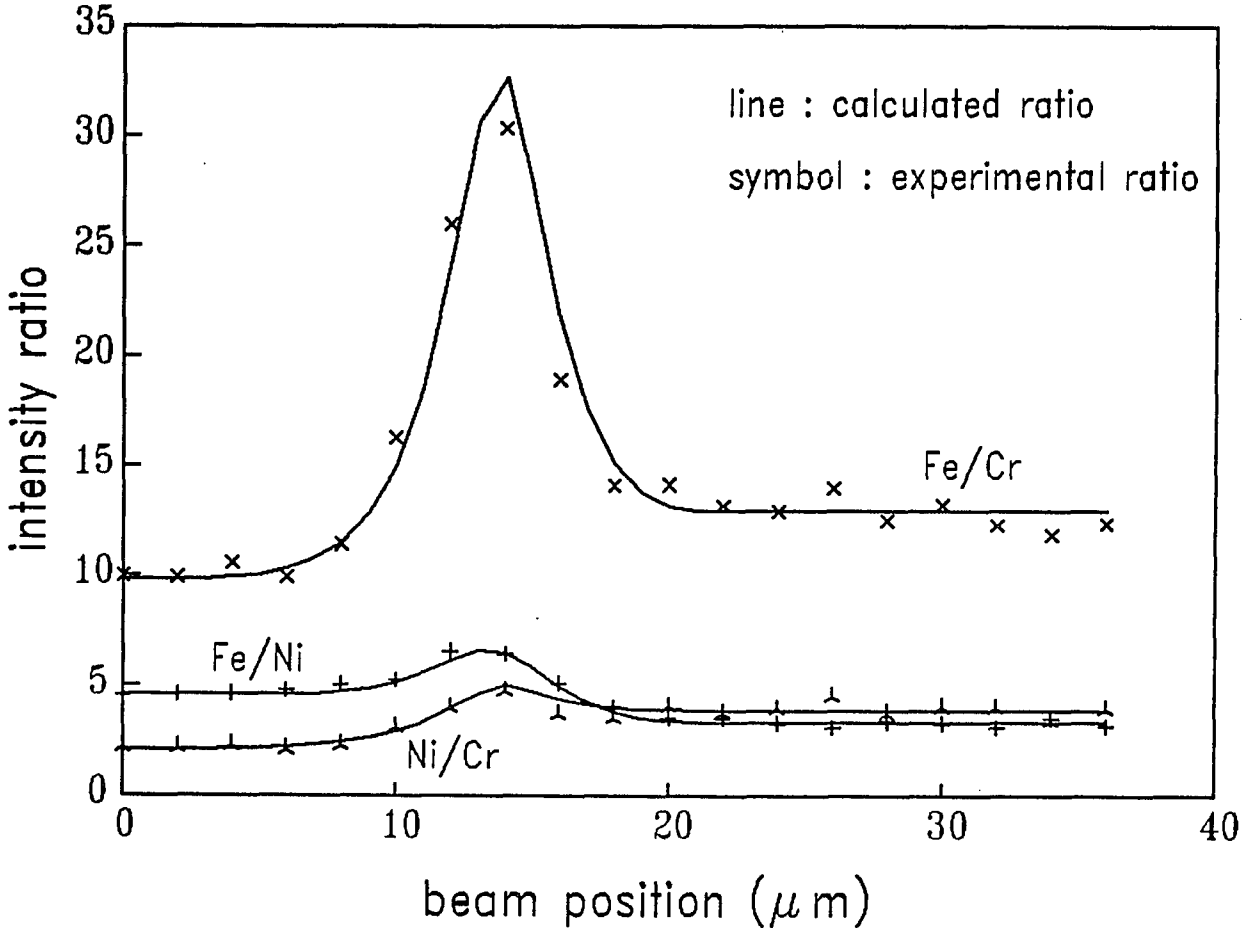

Fig. 6.20. Calculated and measured intensity ratios during a scan across the interface at 1 V (vs SCE) at a pit depth of 1.6 mm.

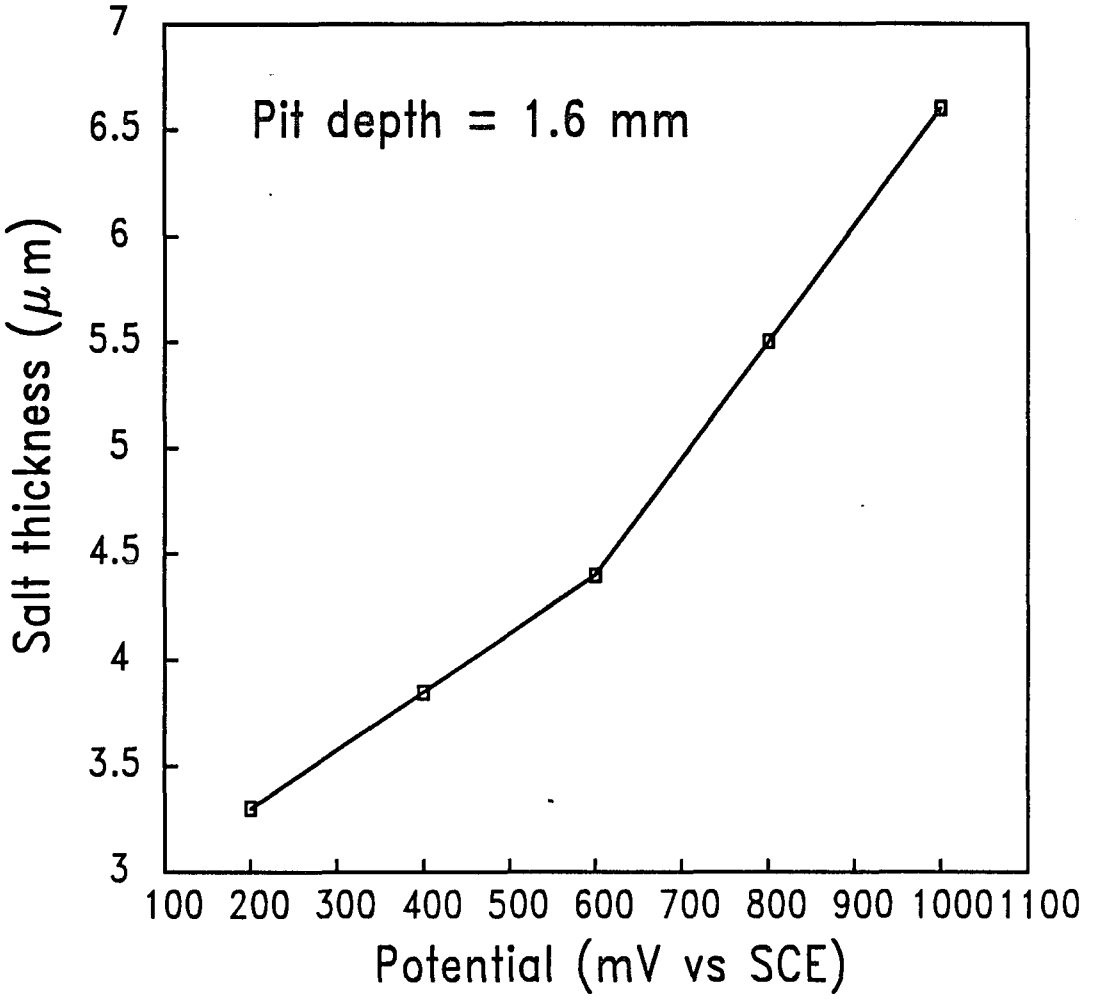

Fig. 6.21. The estimated salt thickness as a function of potential.

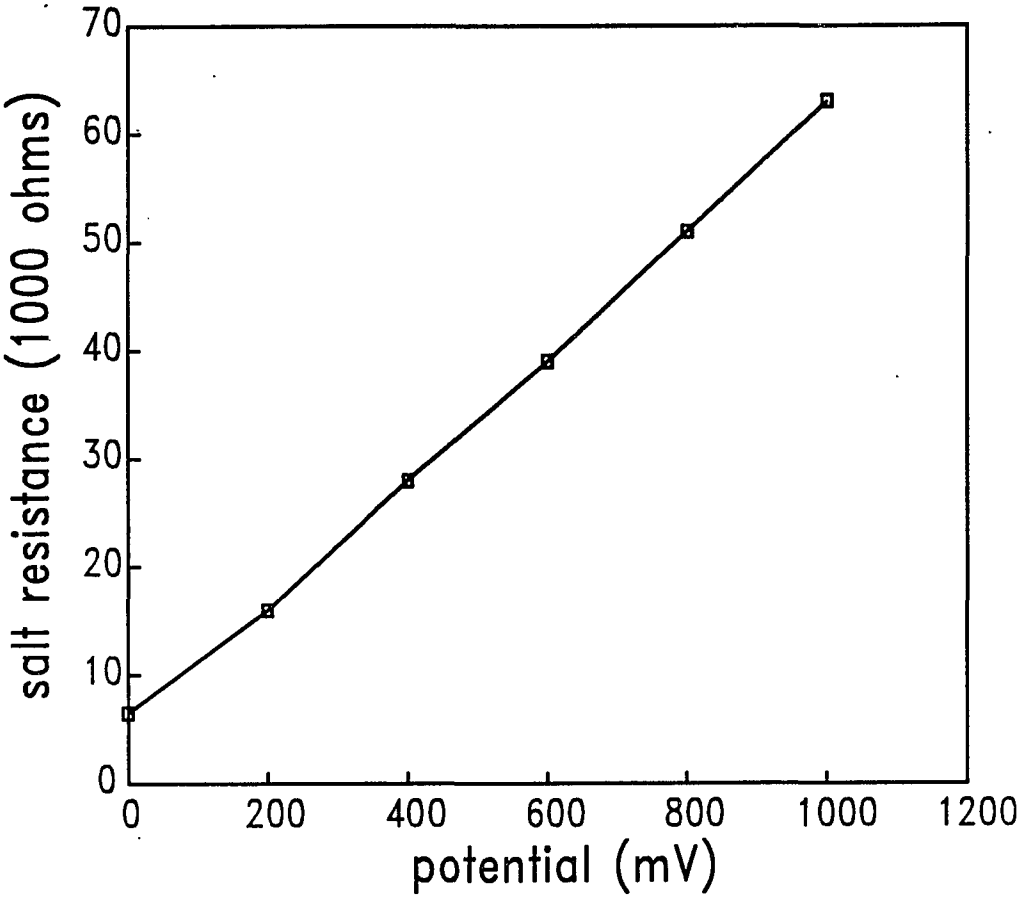

Fig. 6.22. Plot of the resistance of the salt layer vs applied potential at a pit depth of 1.5 mm.

6.3 Conclusions

X-ray microscopy (XRM) measurements and video optical microscopy (VOM) observation are excellent *in situ* techniques to investigate phenomena of localized corrosion. The chemical compositions of the pit solution and the salt layer were quantitatively obtained from the XRM measurements. The results obtained by the technique promise to lead to a better understanding the roles of the pit solution and the salt layer in localized corrosion. Video optical microscopy (VOM) is a desirable tool for monitoring *in situ* corrosion processes taking place at the metal interface. Therefore, one can quantitatively monitor and measure micrometer-scale changes of the interface during electrochemical experiments using both techniques.

This work provided some valuable information for the chemistry of the pit solution and of the salt layer;

1. X-ray fluorescence microscopy measurements were used to determine the concentration profile of the solution and to investigate the chemical composition of the salt layer inside an artificial pit.
2. A saturated salt concentration of the pit solution near the metal/solution interface was approximately 4.7 M ($FeCl_2 \approx 3.15$ M, $CrCl_3 \approx 1.06$ M and $NiCl_2 \approx 0.50$ M).
3. The solution in the pit contains a higher wt % of Cr than in the alloy.
4. The Cr content increased (22 % to 28 %) as the solution approached the pit

mouth, due to slow diffusion of Cr cations.

5. Diffusion coefficients of each metal ion were obtained at different total metal concentrations based on the comparison between the measured and the calculated current densities.

6. The estimated values of the diffusion coefficients of iron and nickel species indicated metal-chloride complexes formed in the highly concentrated solutions inside the artificial pit.

7. The composition of the salt layer was quite different from either the alloy or the solution, consisting mainly of iron chloride.

8. The thicknesses of the salt layer at various applied potential were estimated with curve fitting at a pit depth of approximately 1.6 mm.

9. The resistance of the salt layer increases linearly with applied potential.

10. A crystalline salt was observed at the interface when the potential was interrupted, i.e., when the potential was turned on again after a brief period of turning off the potential.

Chapter 7

RESULTS AND DISCUSSION:

II. Analysis of AC Impedance and Signal Transients

7.1 AC Impedance of a Type 304 Stainless Steel Wire Electrode with Uniform Current Distribution

The AC impedance of a stainless steel wire electrode (3 cm long) immersed in various concentrations (1.0, 0.10 and 0.01 M) of Na_2SO_4 solutions, with a uniform current density at 0.0 mV (vs SCE) in the cell geometry of Fig. 5.7 (a), were plotted in the real/imaginary plane in Fig. 7.1 and showed a constant phase angle, θ, of 80^o in the frequency region between 1.0 and 1000 Hz for all the solutions tested. The impedance measurements were attempted below a frequency of 1.0 Hz, but the results in that frequency region (0.01 ~ 1.0 Hz) were random and did not show reproducibility.

The measured interfacial impedance of the stainless steel wire in the solutions showed some deviation from ideal behavior of a pure capacitor. If the interface were a pure capacitor, the phase angle would be constant at 90^o. For a capacitor and a resistor in parallel, the phase angle varies with frequency and approaches 90^o at the high frequencies. Although the constant phase angle (CPA) with a deviation from 90^o has been often reported in the literature (142-145,190-195), no clear explanation has been proposed (140). The constant phase angle (CPA) has been, in general, observed if the

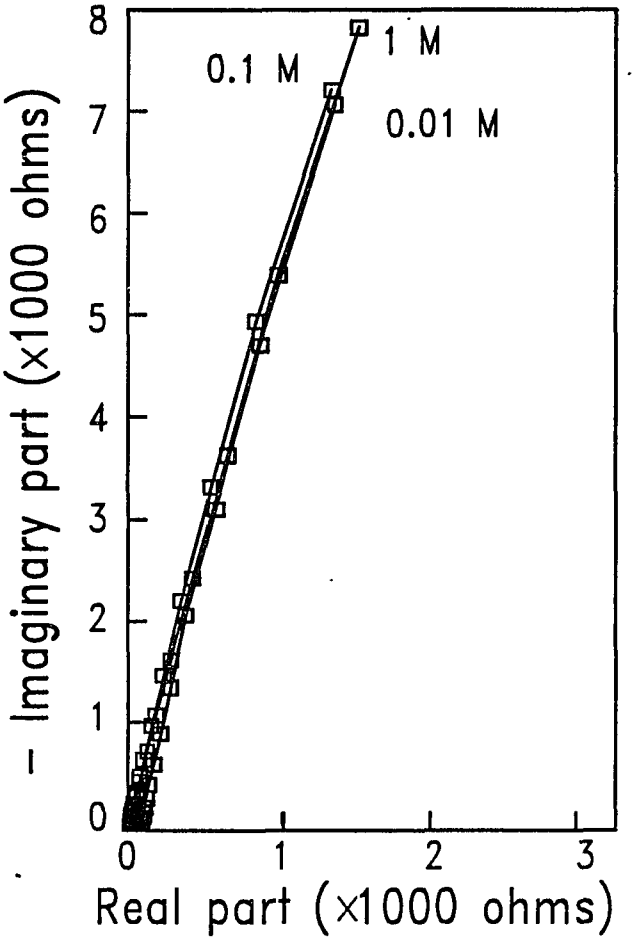

Fig. 7.1. AC impedance of the stainless steel wire electrode in Na_2SO_4 solutions at a potential of 0 mV (vs Ag electrode).

material under investigation is not homogeneous.

The present work does not clarify the cause of the CPA phenomenon, but rather we use the characteristics of the interfacial impedance for a quantitative analysis of the AC signal transmission to study localized corrosion transients. The following equation was established from the measurements for the magnitude of the unit interfacial impedance (ohms/cm) as a function of angular frequency ω:

$$\log z(\omega) = c_1 - c_2 \log \omega \qquad [7\text{-}1]$$

where c_1 and c_2 are the frequency-independent real constants. Eq. [7-1] is the analogue of Eq. [2-6] that shows the constant phase angle (CPA) element. Table 7-I presents the constant values, for various solution concentrations, calculated from the experimental results.

Fig. 7.2 shows the linear dependence of the log of magnitudes of the AC impedance for the short wire electrode with log ω. Deviations from linearity at high frequencies (especially for 0.1 M and 0.01 M solutions) are due to solution resistance between the reference electrode and the wire electrode. An equivalent electrical circuit corresponding to the system can be represented by Fig. 7.3. Since the interfacial impedance cannot be explained as a pure capacitor or a combination of RC components, Z_i was symbolized to represent the interfacial impedance of the wire electrode.

Table 7-I. The values for Eq. [7-1] determined from the experimental results.

Concentration (M)	c_1	c_2
0.01	5.03 ± 0.02	0.892 ± 0.004
0.10	5.07 ± 0.01	0.898 ± 0.002
1.0	5.10 ± 0.01	0.888 ± 0.002

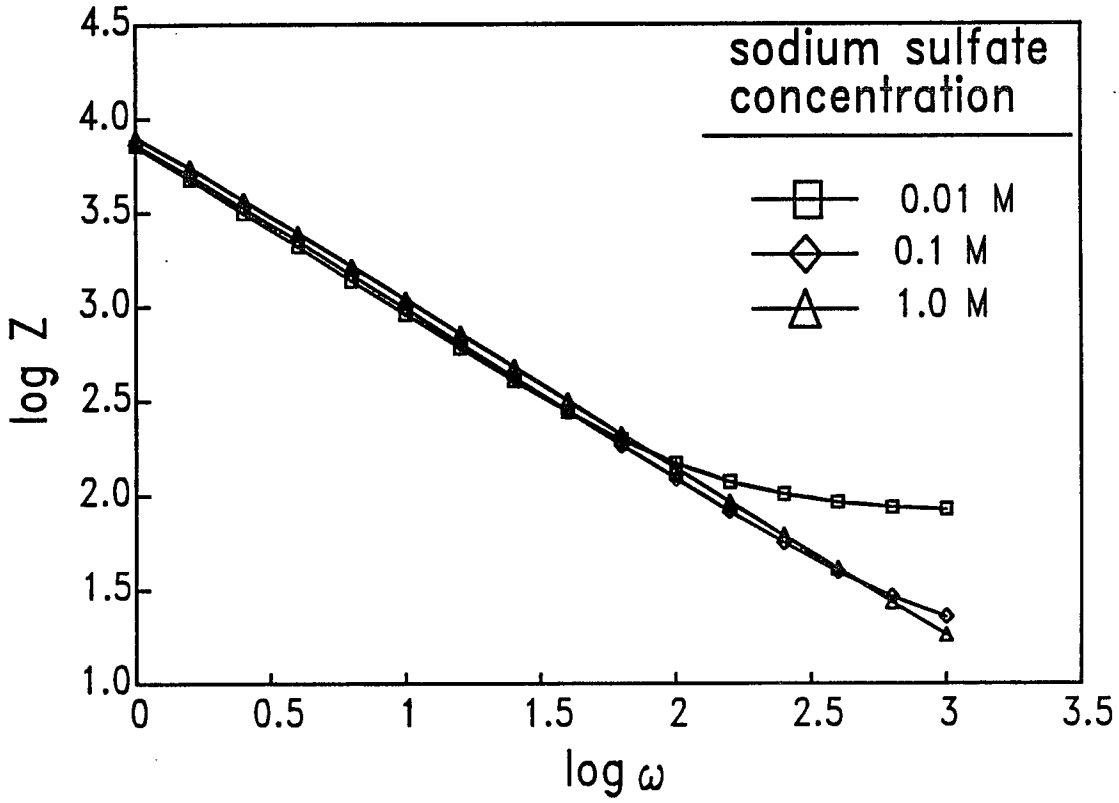

Fig. 7.2. Magnitude of AC impedance of the steel wire as a function of frequency.

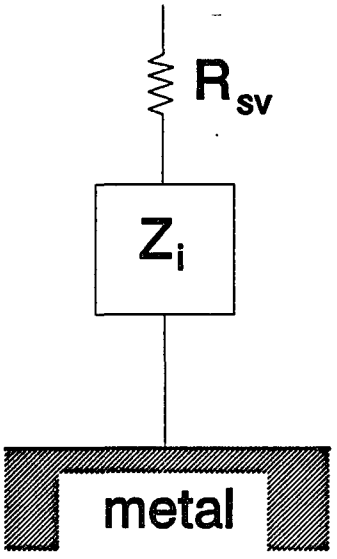

R_{sv} : solution resistance normal to the metal surface

Z_i : interfacial impedance

Fig. 7.3. Equivalent circuit for the electrochemical cell consisting of the wire electrode and the solution.

Fig. 7.4 shows the variation in the magnitudes of the AC impedance, obtained from the short wire, at fixed frequencies as a function of applied DC potential. A potential step of 100 mV was applied from -100 to 400 mV (vs SCE) and a 0.4 M Na_2SO_4 solution was used. The results show that the magnitudes do not change significantly and the capacitive passive oxide film is stable in this potential range. The same result was observed in a 0.55 M NaCl solution which has a conductivity similar to a 0.4 M Na_2SO_4 solution.

7.2 Theoretical Calculation of the Apparent Impedance along a One-dimensional Transmission Line

Cho *et al.* (157) introduced the apparent impedance which described the effects of the capacitive passive metal surface, the solution resistance and the location of the sensing electrode on the impedance measurements. The apparent impedance $\mathbf{Z}(x) = \mathbf{V}(x)/\mathbf{I}(0)$, in which x is a distance along a one-dimensional transmission line, was derived from the equivalent circuit diagram shown in Fig. 5.8. $\mathbf{V}(x)$ is the small sinusoidal potential at a given distance x and $\mathbf{I}(0)$ is the sinusoidal current flowing at the origin.

The variation of potential and current along a one-dimensional electrode can be mathematically written as

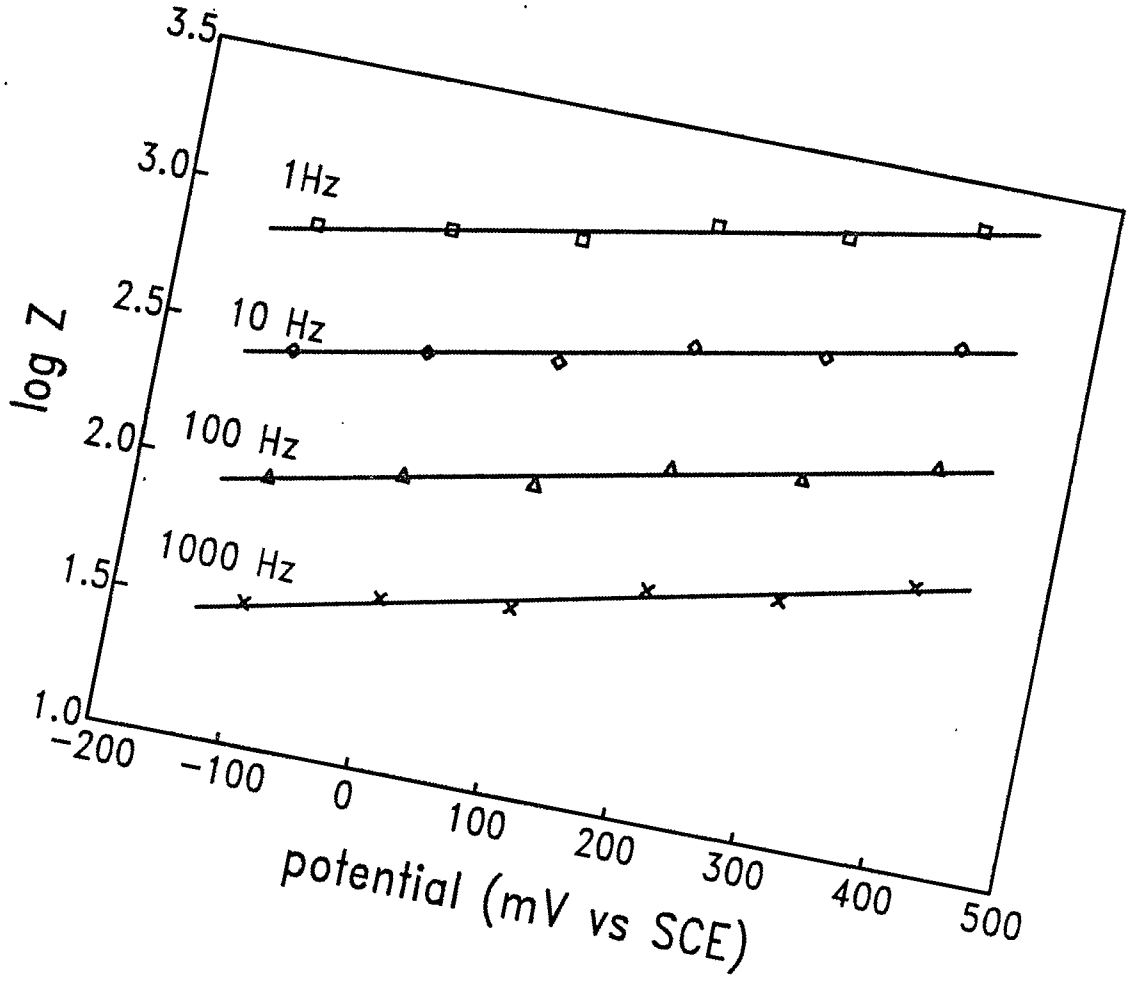

Fig. 7.4. Magnitudes of AC impedance of the steel wire as a function of a applied DC potential.

$$\frac{\partial V(x)}{\partial x} = -I(x)\ R_s(x) \qquad [7\text{-}2]$$

$$\frac{\partial I(x)}{\partial x} = \frac{V(x)}{Z_i} \qquad [7\text{-}3]$$

The second derivatives of Eqs. [7-2] and [7-3] lead to

$$\frac{\partial^2 V(x)}{\partial x^2} - \frac{R_s}{Z_i} V(x) = 0 \qquad [7\text{-}4]$$

For a semi-infinite transmission line system, the general solution becomes

$$V(x) = I(0)\sqrt{R_s Z_i}\exp(-x\sqrt{R_s/Z_i}) \qquad [7\text{-}5]$$

The interfacial impedance of the wire electrode per unit length, Z_i, can be expressed in terms of its magnitude, $z(\omega)$, and phase angle, $\theta(\omega)$:

$$Z_i(\omega) = z(\omega)\ \{\ \cos\theta(\omega) + i\ \sin\theta(\omega)\ \} \qquad [7\text{-}6]$$

R_S is the solution resistance per unit length (cm) which can be determined from the equation

$$R_s = \frac{\rho}{A} \qquad [7\text{-}7]$$

where ρ is the solution resistivity and A is the cross-sectional area of the solution.

Since it is not possible to measure the current flowing at a distance x, the apparent impedance, $Z(x)$, is introduced. The apparent impedance is defined by the voltage, $V(x)$, divided by the total current, $I(0)$, flowing into the line at $x = 0$. Therefore the mathematical expression of the apparent impedance can be obtained using Eq. [7-5]:

$$Z(x) = \frac{V(x)}{I(0)} = \sqrt{R_s Z_l}\exp(-x\sqrt{R_s/Z_l}) \qquad [7\text{-}8]$$

Eq. [7-8] shows the relationship between the apparent impedance and the distance along a one-dimensional transmission line.

Combining Eqs. [7-6] and [7-8] yields an expression for the real and the imaginary part of the apparent impedance:

$$Z(\omega,x) = P(\omega,x)\ \{\ \cos Q(\omega,x) + i\ \sin Q(\omega,x)\ \} \qquad [7\text{-}9]$$

$$P(\omega,x) = \sqrt{R_s z(\omega)}\ \exp\{-x\sqrt{R_s/z(\omega)}\ \cos\frac{\theta(\omega)}{2}\} \qquad [7\text{-}10]$$

$$Q(\omega,x) = \frac{\theta(\omega)}{2} + x\sqrt{R_s/z(\omega)}\ \sin\frac{\theta(\omega)}{2} \qquad [7\text{-}11]$$

As the distance x increases, the magnitude of the impedance decreases exponentially while the phase angle increases continuously giving a spiral Nyquist plot. The above equations were manipulated to calculate the theoretical apparent impedances at a given

distance on a one-dimensional transmission line with the interfacial impedance and solution resistance being determined by EIS measurements.

The main idea behind the work in this chapter is the use of experimentally-determined interfacial impedances. Others generally use capacitance (135,136) or a combination of capacitance and resistance (155) to represent interfaces. The difference may be not significant for an individual interfacial circuit unit, i.e., the difference between C_i or Z_i from generalized circuit elements and experimentally-determined Z_i may be very small. However, when the unit impedances are added to the transmission lines, the difference is magnified due to the exponential terms involved in the model calculation (see Eq. [7-8]). Therefore it should be emphasized that accurate determination of the interfacial impedance and the solution resistance is very important for model calculation of transmission lines.

7.3 Analysis of the Apparent Impedance along A One-dimensional Transmission Line

In the present work, the transmission of AC signals along the electrode surface was investigated with the measurements of the apparent impedance $\mathbf{Z}(x)$, at a particular distance x, and the interfacial impedances $\mathbf{Z_i}$. The solution resistance of each concentration fixed in the tube was measured using the same size tube (Fig. 5.7 (b)) and was also calculated from the resistivity of the solution and the tube area as demonstrated in Eq. [7-7]. The values obtained from both processes were identically 220 ohm/cm for

a 0.1M Na_2SO_4 solution.

Fig. 7.5 shows a plot of the experimental results for the real and imaginary part of the AC impedance at various distances from one end of a one-dimensional transmission line consisting of the long stainless steel wire and 0.1 M Na_2SO_4 solution. The measurements were made at a potential of 0 mV (vs Ag electrode). The theoretical apparent impedances were calculated from Eqs. [7-9], [7-10] and [7-11] with the values of the interfacial impedance determined from the measurements and of the solution resistance. The calculated results agreed well with the experimental ones within the error range of $\pm$ 5 %. However, for high frequencies far from the origin, the error range was larger.

Fig. 7.6 shows the variation of the magnitude of the apparent impedance, at various frequencies, as a function of frequency. The magnitudes of the high frequencies at the distances of 16 and 25 cm did not decrease as expected. This could be due to the vertical portion of the solution resistance which is significant for high frequency compartments. A correction of the model considering the vertical solution resistance will be discussed in a later section (Section 7.7). The measurement limit of the instruments or the noise level of the electrochemical cell may also contribute to this observation. The travel distance of the high frequency signals along the transmission line is shorter than the low frequency signals, and therefore the low frequency signals should be used for detection of localized corrosion along transmission line systems (155).

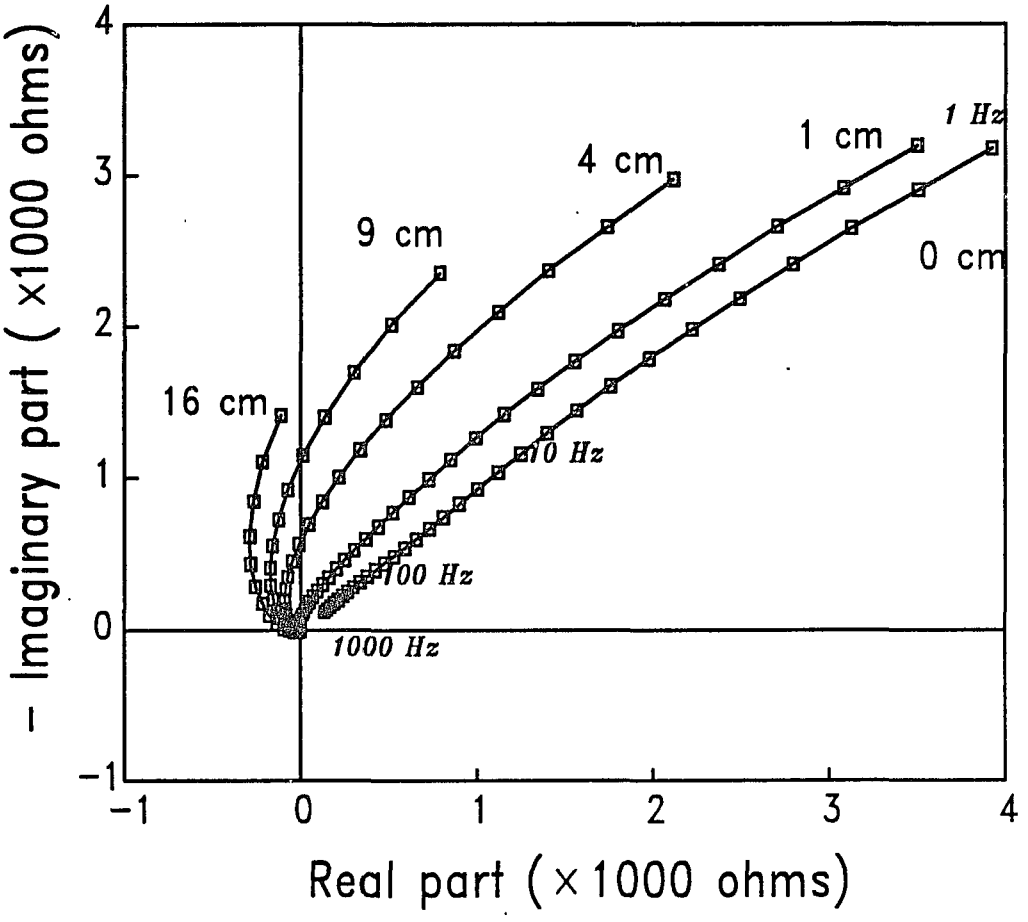

Fig. 7.5. Real and imaginary part of the apparent impedance for the system consisting of the wire and a 0.1 M Na_2SO_4 solution.

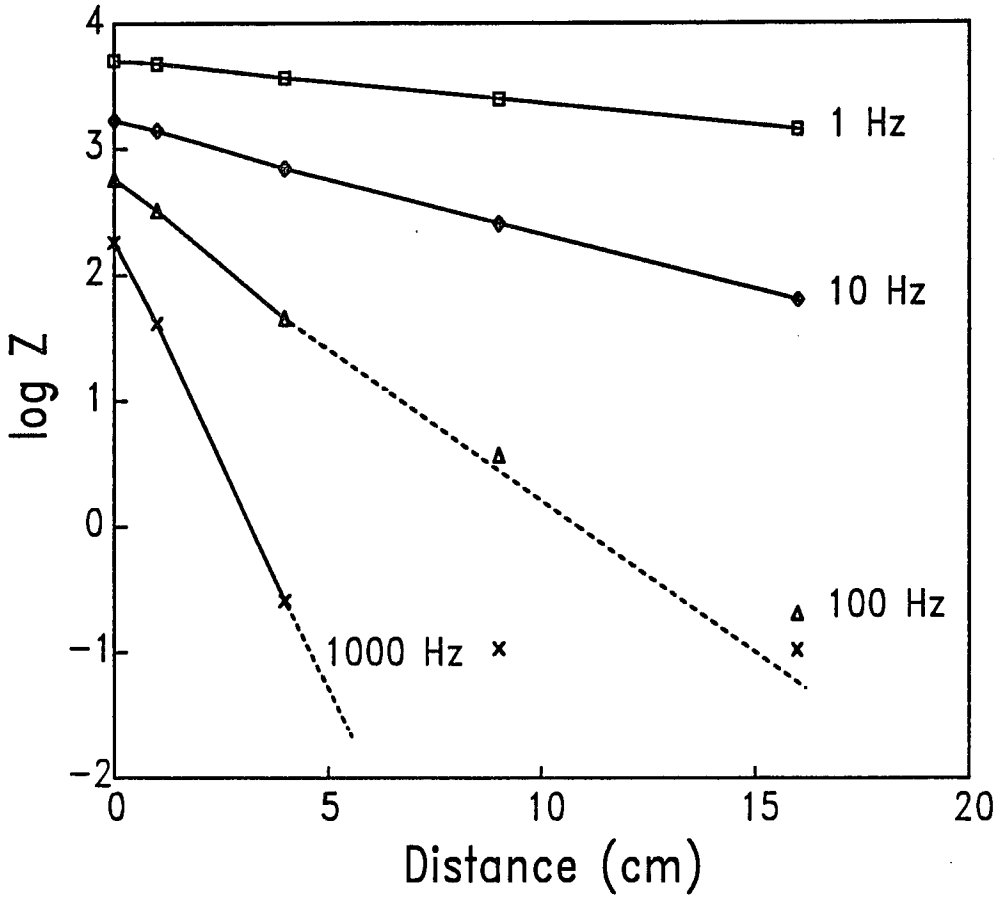

Fig. 7.6. Plot of the magnitude of the apparent impedance as a function of distance along the transmission line.

7.4 Effect of Local Corrosion on the Apparent Impedance

A piece of iron wire connected to the long steel wire was immersed at a particular position along the tube and the apparent impedance was measured at 0 distance. Fig. 7.7 illustrates the effect of a iron wire on the magnitude of the apparent impedance measured in 0.55 M NaCl solution at a potential of 0 mV (vs Ag/AgCl electrode). The iron wire is certainly more corrosive than the stainless steel at this potential and acts as a localized corrosion site on the transmission line. The corroding iron wire has a lower impedance value than the steel. The magnitude of the apparent impedance decreased markedly in the low frequency region when iron was placed 4 cm from the origin. The apparent impedance in the high frequency region, however, increased slightly in magnitude. The low frequencies which arrive at the iron site (corrosion site) experience a low impedance site and the measurements result in lower apparent impedances. The changes in the magnitude of the apparent impedance are dependent on the position of a corrosion site. The apparent impedance measurements of the transmission line therefore can be a useful tool to monitor localized corrosion as well as to determine its location.

7.5 Theoretical Calculations of Potential Response along Transmission Line

A part of the present work involves development of a quantitative analytical method of investigating localized corrosion transients using Fourier analysis and EIS measurements. Current and potential transients in the time domain can be converted to frequency components by Fourier transformation and each frequency segment of the

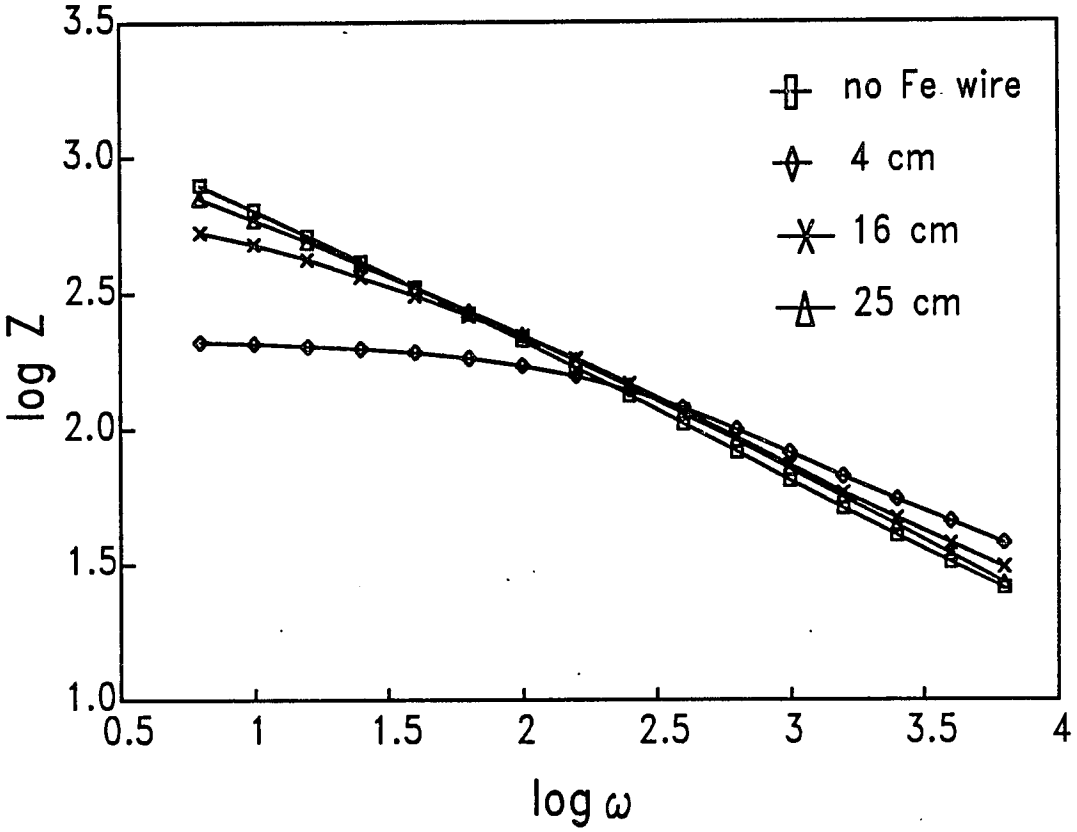

Fig. 7.7. The apparent impedance of the steel wire in the presence of iron wire at various positions along the transmission line.

transients can be treated independently.

A known-shaped potential (rectangular) pulse was employed as an initial transient that simplifies a localized corrosion transient observed during pit initiation and repassivation. Then the potential responses at various distances along the transmission line were measured and the expected transients were also calculated by Fourier analysis of the transients. Variations in the magnitude and the phase angle of the frequencies as a function of distance along the transmission line, which are predicted from Eq. [7-9] and inverse Fourier transformation, make it possible to construct the expected signal transient (158) at a given distance.

Fig. 7.8 shows how the theoretical response of the transient can be calculated. The processes are reversible so that a initial transient can be ideally recovered from an observed transient if one 1) can take into account the effects of surface impedance and solution resistance on transmission of an AC signal and 2) knows the distance from the origin where localized corrosion events take place. Fourier transform of an input pulse transient, $f(t)$, in the time domain produces a corresponding frequency spectrum, $g(\omega)$, which will be altered by the characteristics of a transmission line. $G(\omega,x)$ will be later used to construct a transient response, $F(t,x)$, at a particular distance. Finally, the simulated results will be compared with the observed potential transients.

The Fourier-pair equations for a transient are written as follows:

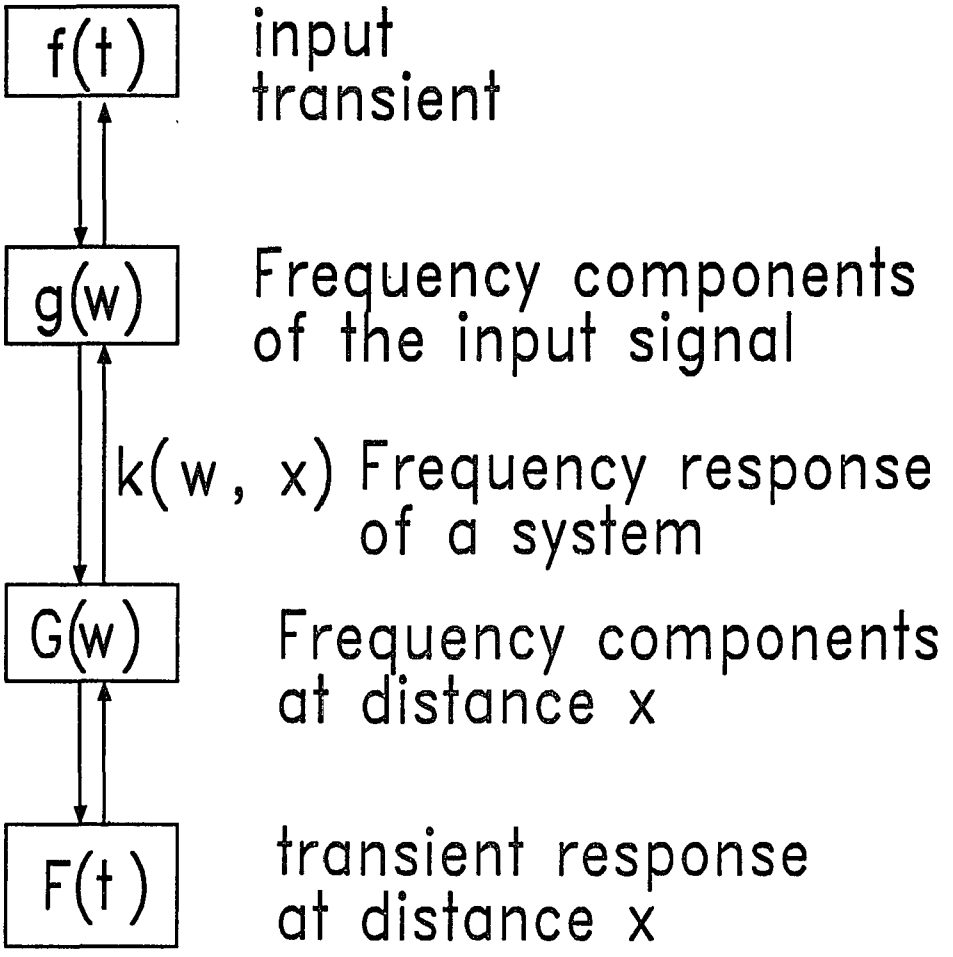

Fig. 7.8. A schematic diagram for the Fourier transformation of a transient.

$$f(t) = \frac{1}{\sqrt{2\pi}} \int_{-\infty}^{\infty} g(\omega) \exp(i\omega t)\, d\omega \qquad [7\text{-}12]$$

$$g(\omega) = \frac{1}{\sqrt{2\pi}} \int_{-\infty}^{\infty} f(t) \exp(-i\omega t)\, dt \qquad [7\text{-}13]$$

Eq. [7-12] is called the complex Fourier integral representation of the transient function, $f(t)$, and $g(\omega)$ is the Fourier transform of $f(t)$ (158). The transfer characteristic, $k(\omega,x)$, is multiplied by $g(\omega)$ which is the amplitude of the input AC signal. This process produces the outcome AC components, $G(\omega,x)$, at a given distance.

$$G(\omega,x) = g(\omega)\, k(\omega,x) = g(\omega) \exp\{-x\sqrt{R_s/Z_i(\omega)}\} \qquad [7\text{-}14]$$

where x is the distance from the origin,

R_S is solution resistance, and

$Z_i(w)$ is the interfacial impedance.

The inverse Fourier transform of $G(\omega,x)$ gives a transient $F(t,x)$ at a distance x.

$$F(t,x) = \frac{1}{\sqrt{2\pi}} \int_{-\infty}^{\infty} G(\omega,x) \exp(i\omega t)\, d\omega \qquad [7\text{-}15]$$

A more complete description of the mathematical derivation is given in Appendix.

In the present work, the experimentally-determined interfacial impedance which showed the complicated behavior represented by the constant phase angle (CPA) was utilized to construct the simulated response of potential transients at a given distance.

The computer calculation of a response pulse was as follows: a rectangular pulse in the time domain was converted to a frequency domain by Fourier transform, the magnitude and the phase angle of each frequency at a given distance were deduced from Eq. [7-5] based on a one-dimensional transmission line model, and finally a pulse response at a given distance was constructed by Eq. [7-15]. The processes will be explained more precisely in the following sections.

7.6 Analysis of a Simulated Potential Transient During Localized Corrosion

Mathematical derivation of the expected signal transient at a given distance is complicated because of the complex terms involved in the calculations. First, the frequency spectrum of the pulse (200 mV in magnitude and 2 msec in duration) was calculated with a Fourier transform, Eq. [A1] and [A2] (see Appendix) where t_1 = 2 msec, t_2 = 4 msec and f_o = 200 mV. Fig. 7.9 shows that the amplitudes of the frequencies higher than 10 kHz do not decrease to 0 or even near 0. Therefore integration of frequencies in Eq. [A5] must be carried out from - ∞ to ∞ for reconstruction of the rectangular pulse. Since it is impossible to integrate an infinite range of frequencies, a cutting-off above a certain frequency is a must to perform the calculations within a finite time.

Fig. 7.10 shows a rectangular pulse constructed by integration between a frequency range of 0 to 10000 Hz with a frequency interval of 10 Hz. It is not

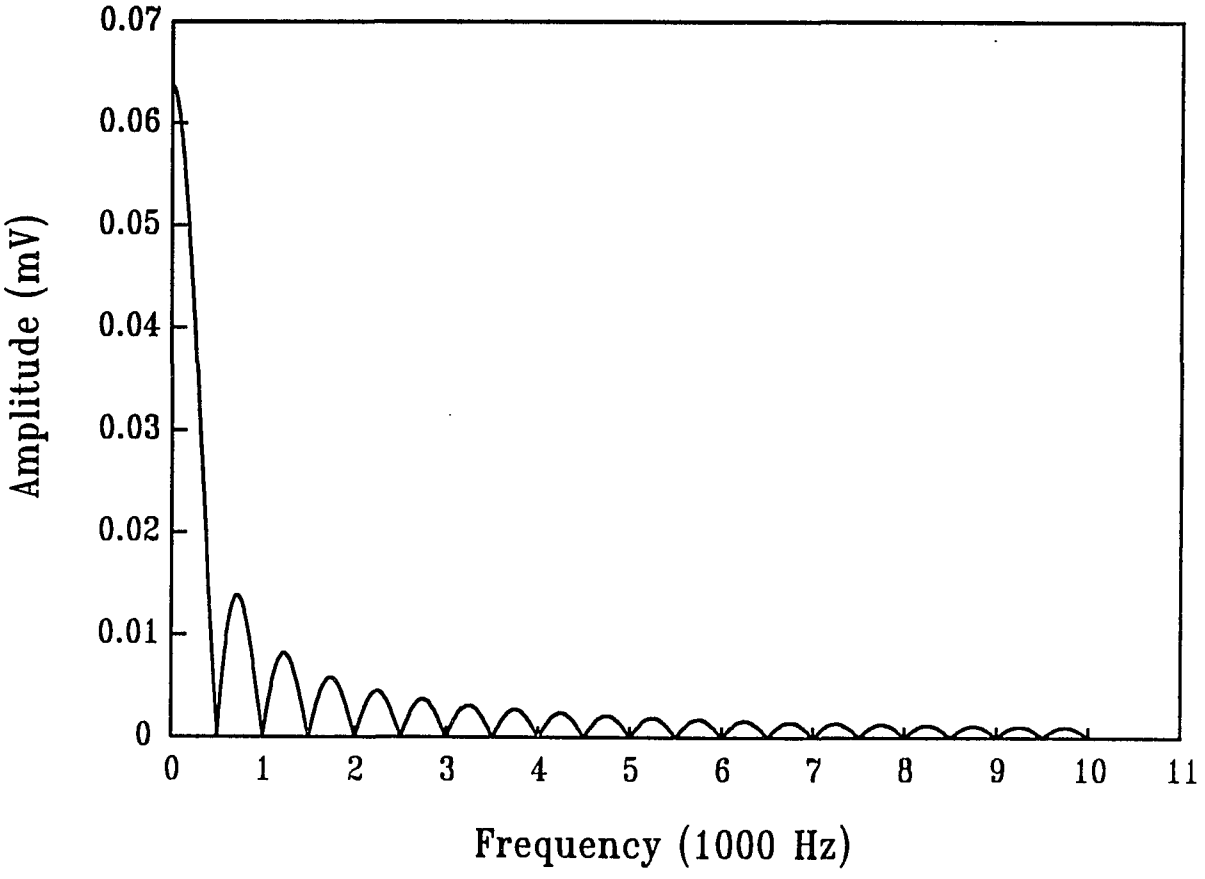

Fig. 7.9. Amplitude of frequencies which are the components of the rectangular pulse (200 mV and 2 msec).

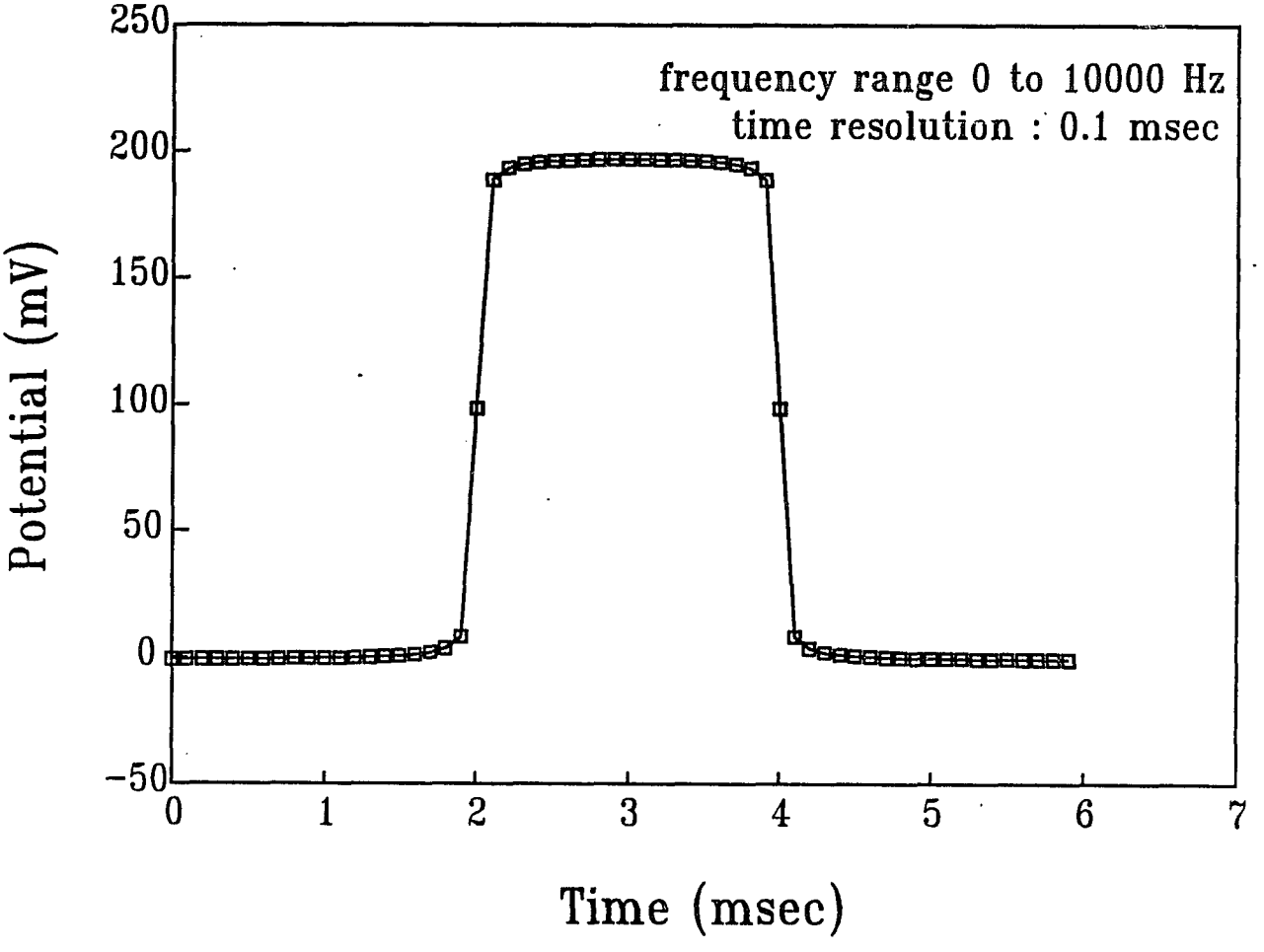

Fig. 7.10. A rectangular pulse constructed from a Fourier integral of the frequencies from 0 to 10000 Hz.

completely rectangular, but gives a shape that can represent a rectangle. A faster, more powerful computer can allow a increase in integration range and reduce the time for calculations. Away from the original point where the pulse was introduced, the magnitudes for higher frequencies decrease rapidly and exponentially so that one can ignore those high frequencies without any significant problem. This will be more obvious from Fig. 7.11 that shows the amplitude of the frequency components at various distances from the position where the original pulse was initiated. Fig. 7.11 can be compared with Fig. 7.9 to see how the magnitudes of the high frequency components decrease with distance. It also indicates that monitoring of transient signals far from the origin would result in a loss of information from the high frequency components. The apparent impedance of the lower frequencies than 1 Hz was not determined by the experiment for the practical purpose because the measurements were not reliable and it would take long time to collect impedance data beyond this frequency.

7.7 Correction for a Vertical Solution Resistance

The characteristics of high frequencies (> 1 kHz) were also considered using Eq. [7-1]. As discussed, the magnitudes and the phase angles of the high frequencies are significantly affected by a vertical solution resistance. The solution resistance, R_{sv}, vertical to the transmission line was added to correct Eq. [7-1]:

$$z_s(\omega) = \sqrt{z(\omega)^2 + R_{sv}^2} \qquad [7\text{-}16]$$

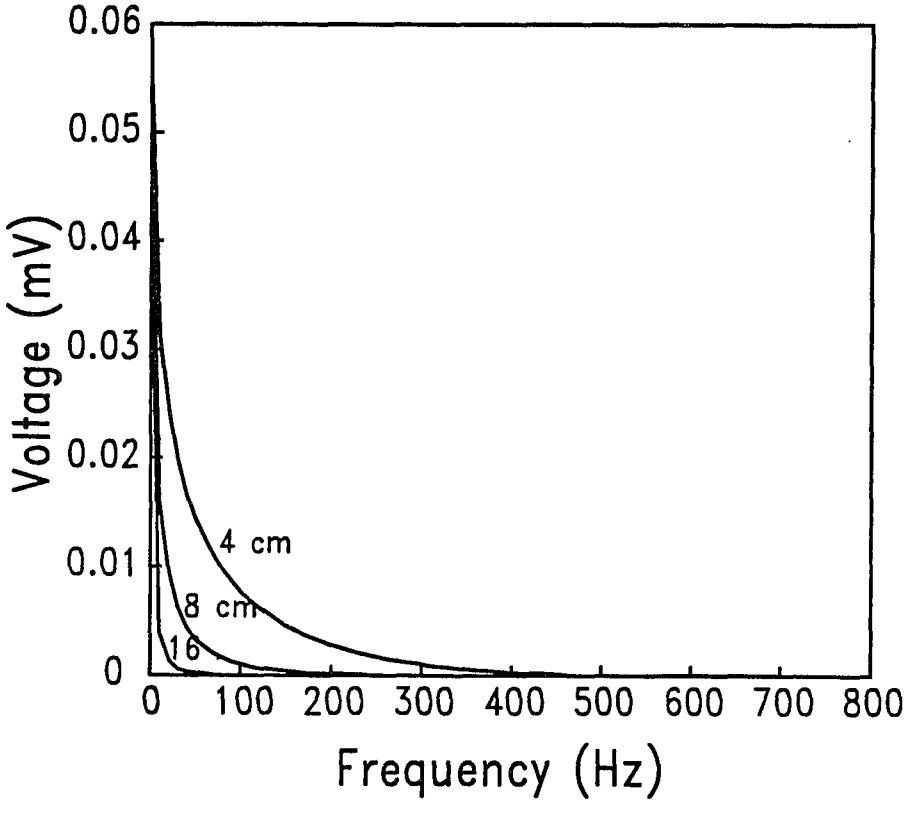

Fig. 7.11. Magnitude of the frequency components of the pulse responses calculated based on a transmission line.

where z_s is the modified interfacial impedance including R_{sv}. The phase angle is also no longer a constant, being expressed as

$$\theta_s(\omega) = \tan^{-1}\frac{z(\omega)\sin\theta}{R_{sv} + z(\omega)\cos\theta} \qquad [7\text{-}17]$$

where θ_S is the modified phase angle corrected with R_{sv}. The above correction particularly gives a significant change in the region of high frequency. The AC impedance for high frequencies almost acts as a pure resistance.

Fig. 7.12 shows the observed transient in 0.1M Na_2SO_4 solution (R_s = 220 ohm/cm and R_{sv} = 50 ohm/cm) and the simulated transients at 4 cm with and without considering a vertical solution resistance, R_{sv}. The integration range in Eq. [A6] was chosen from 0.0 to 1000 Hz with a interval of 10.0 Hz. The simulated transient using R_{sv} provides a slightly better fit to the observed transient. This indicates that the vertical solution resistance should be included in the consideration of a transient response along a one-dimensional transmission line.

The process of reconstructing a response pulse here has a certain limitations: limitations in the integration range and a width of the frequency interval ($d\omega$), and a limited range in the frequency response of the system (in this work we only obtained information over the frequency range between 1.0 and 1000 Hz). In addition,

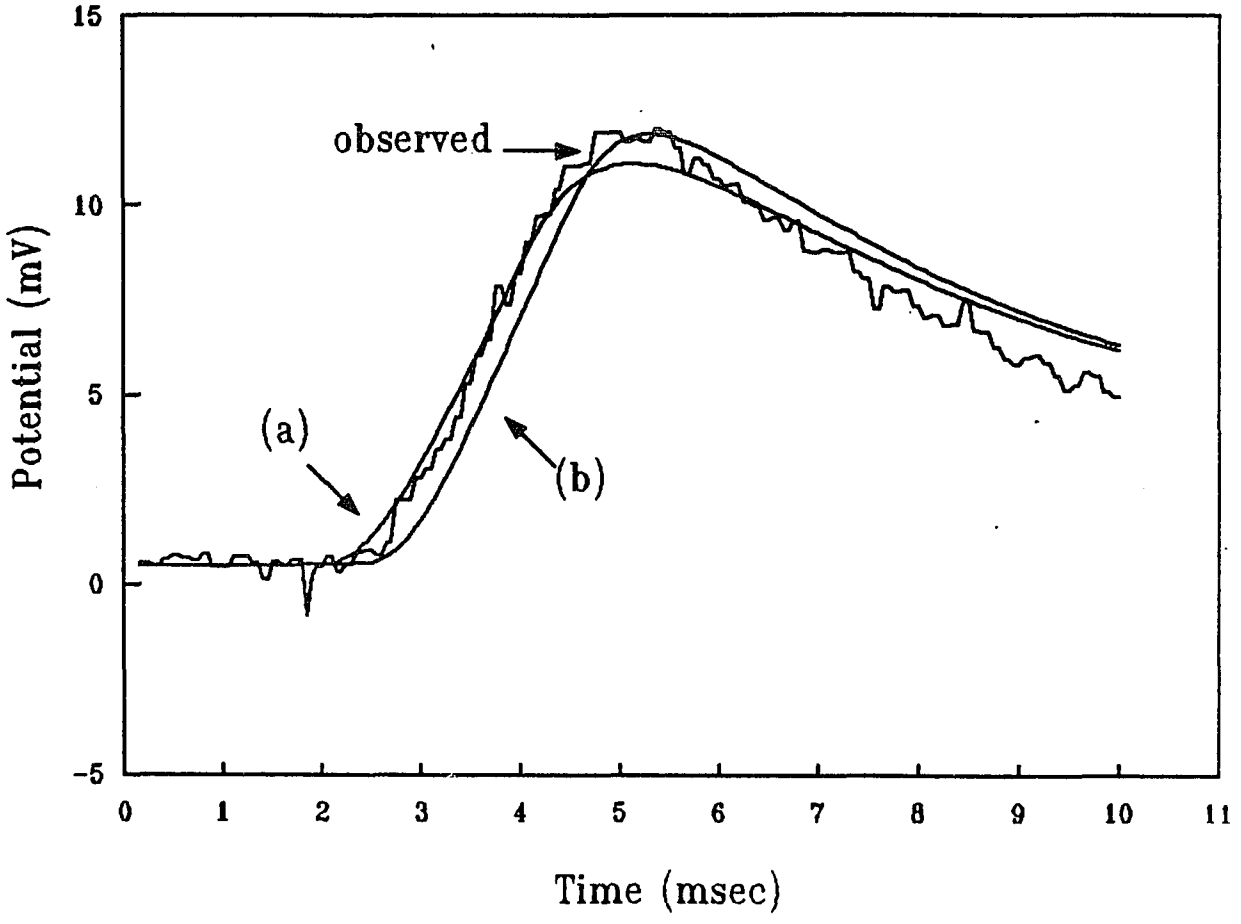

Fig. 7.12. A pulse response measured at 4 cm from the origin and its theoretical response calculated using the Fourier transformation: (a) with and (b) without considering the vertical solution resistance.

frequencies lower than 1.0 Hz are not properly involved in calculation due to the lack of experimental information for this low frequency. It is, however, possible that one can use information over moderate frequency range (1.0 to 1000 Hz for the system that we investigated) to study signal transients associated with localized corrosion. Constructing a pulse response resulted in a better understanding of signal transients along a one-dimensional transmission line.

Chapter 8

SUMMARY

8.1 *In situ* Microanalysis of Artificial Pits

This work provided some valuable information on the chemistry of the pit solution and the salt layers, which were obtained using various experimental techniques to investigate artificial cavities formed during anodic dissolution of the metal. The present work demonstrated the capability of *in situ* x-ray microprobe techniques, video optical microscopy observations and scanning electron microscopy for investigating localized corrosion. The fluorescence measurements using a synchrotron radiation x-ray microprobe, which has been available only recently, provided microanalytical chemical information on the pit solution and the salt layer. This chemical information has not been obtained by any other conventional chemical analysis. Video optical microscopy is a superior *in situ* tool for observation of the salt films at the metal/solution interface under various conditions of applied potential and at various pit depths.

The important results and discussion mentioned in the present thesis, related to the microanalysis of artificial pits, are summarized as:

1. A one-dimensional artificial pit, "a sandwich-type pit", was fabricated for x-ray fluorescence microscopy study of localized corrosion.
2. X-ray fluorescence microscopy measurements were used to determine the

concentration profile of the solution and the salt layer inside a simulated pit.

3. The saturated concentration of 67% $FeCl_2 \cdot 4H_2O$, 22% $CrCl_3 \cdot 6H_2O$ and 11% $NiCl_2 \cdot 4H_2O$ mixture was found to be approximately 4.7 M near the metal/solution interface.

4. The solution in the pit contains relatively higher wt% of Cr than in the alloy.

5. The Cr content increased (22% to 28%) as the solution approached the pit mouth.

6. Diffusion coefficients of each metal ion were calculated from the analysis of the XRM data as a function of its concentration. The diffusion coefficients of iron and nickel were compared with literature values, indicating the presence of metal-chloride complexes in the high concentrated pit solutions.

7. Video optical microscopy was used to monitor the salt layer at the metal/solution interface during anodic dissolution of the metal. This initiated the investigation of the salt layer using the XRM measurements.

8. The composition of the salt layer (Fe : Cr : Ni = 88 : 6: 6) was quite different from either the alloy (69 : 18 : 13) or the solution (67 : 22 : 11) near the metal interface.

9. The concentration of the salt was found as 9.65 M with the above metallic ratio. The difference in the concentration between the salt and the saturated solution may indicate that a supersaturation period during anodic dissolution of the metal is transiently required in order to form a salt layer. This supersaturation stage was experimentally observed by x-ray absorption measurements (the results were not shown in this thesis) that were carried out during the early stage of the

present work at the Beamline X-11 in National Synchrotron Light Source (NSLS).

10. The thicknesses of the salt layer at a pit depth of 1.6 mm as a function of the applied potential (vs SCE) were estimated by using a curve fitting and the fundamental parameters method.

11. Electrochemical impedance measurements demonstrated that the salt layer has resistance characteristics which are dependent on the applied potential.

12. A crystalline salt was observed transiently when anodic dissolution was reactivated after a short interruption of the potential. The crystal were thick and provided a large potential drop between the metal surface and the solution, resulting in a current minimum during anodic dissolution.

13. Insoluble corrosion products were observed in the dissolved area of the commercial stainless steel. A very porous gel-like silica occupied the dissolved area of the steel, but this did not affect the diffusion path of the dissolved corrosion products. These products were investigated by Scanning Electron Microscopy (SEM).

14. If the applied potential was turned off for enough time to allow for the steel interface to repassivate completely, subsequent dissolution often left fragments of the steel under the passive surface that were undermined when the adjacent surface was reactivated. These were observed with an optical microscope.

15. The fragments were the major obstacle for the diffusion path of the dissolved species and for the x-ray microscopy measurements. Therefore, x-ray measurements were conducted with a single continuous dissolution.

8.2 AC Impedance and Signal Transients along a Transmission Line

In the investigation of transmission of AC signals along a one-dimensional transmission line, we were able to understand the quantitative behavior of AC signals subject to a one-dimensional transmission line and to construct the simulated transients based upon a knowledge of the AC signal transmitted in a one-dimensional system. The transmission of a AC signal along a one-dimensional system was as expected by the model. However, high frequency components do not depend upon distance beyond a certain limit. Therefore, the validity of high frequency information on the transmission line decreases with increasing distances and low frequency components can be used to study signal transmission quantitatively. The measurements of the apparent impedance at the beginning of a transmission line can be a useful tool to monitor localized corrosion as well as to determine its location. Again, the magnitudes of the impedance in the low frequency region were markedly changed, depending on the position of a corrosion site. The magnitudes in the high frequency region were also changed with a corrosion site and this may correspond to the change in the capacitive passive surface.

Reconstruction of the potential or current transient generated at a corrosion site during the early stage of pitting could be possible by analysis of the signal transients monitored along a transmission line. The capacitive interfacial impedance, the solution resistance and location of the pitting site are the variables in the analysis. Fourier analysis of the pulse was used to investigate this signal transient problem. A rectangular

pulse was made by fourier integral of frequencies and a pulse response at 4 cm apart from the original site was also constructed after consideration of the above variables. The actual measurements were carried out using the pulse that was used in the calculation and the response at 4 cm was monitored. The measured and the calculated pulse response were well agreed each other. The processes of the calculation is reversible so that recovery of the original transient can be made from the signal response recorded at a certain distance away from the original site. This original signal transient could provide valuable information for the kinetic study of pit initiation and repassivation. It was also found that the vertical portion of solution resistances as well as the interfacial impedance and the solution resistance plays a role in signal transients.

8.3 Suggestion for the future work

A more thorough analysis of the experimental results obtained from x-ray fluorescence, absorption measurements and scanning electron microscopy can provide necessary information on theoretical calculations. The effect of gel-like silica occupying the dissolved area on dissolution of the metal was not visible when the XRM results between a commercial (0.5 % Si) and a pure (no Si) stainless steel were compared. However, it is quite possible that the physical presence of the silica in the dissolved area could affect diffusion rates of the dissolved corrosion products. Therefore, the silica effect should be carefully investigate in order to understand diffusion of the dissolved metal species. The effects of the minor elements, such as molybdenum and copper, on dissolution of the steel were excluded at the present work. However, they are important

elements (especially Mo) of stainless steels. The next step of the study should focus on these elements.

A complete model calculation for pit solutions will be possible if all the variables, such as stability constants of metal-chloride complexes, their diffusion coefficients as a function of a total metallic concentration, potential gradients and mobilities of the species, can be found. However, the variables are not available in most cases for the concentrated solution formed by dissolution of stainless steels in chloride environments. The experimental works using x-ray fluorescence and absorption should be continued to provide these variables. An early study of the present work using x-ray absorption technique focused on the energy region of the K-absorption edge for each metal element. The magnitude of the edge peak would provide the amount of the element, which was investigated, in a sample solution, but the simultaneous determination of all the elements was not possible by the measurements. However, x-ray absorption measurements can be used to obtain a extended x-ray fine structure which can contribute to a quantitative understanding of metal-chloride complexation in the pit solution.

Higher spacial resolution of the x-ray microprobe could be achieved by using a smaller pin-hole ()8 μm in diameter). An increase in the spacial resolution will be critical to investigate the very thin salt layer (less than 10 μm) present on the metal/solution interface during anodic dissolution of the metal.

In the present work, iron was found as a dominant element in the salt layer which was formed during anodic dissolution of the stainless steel. The dissolution rate of the salt, which could be a determining step of the corrosion rate, may depends on the chemical composition of the salt layer. Investigation of the salt layers, forming during dissolution of other alloys, will be interesting to understand the effect of chemical compositions of the salt on the dissolution rate and corrosion rate. Nickel-based alloys may be suitable to study since nickel is expected as a dominant element in the salt layer. Differences in corrosion rate or in corrosion resistance between nickel-based and iron-based (stainless steels) alloys could be explained by differences in the chemical compositions of the salt layers between the alloys.

A video camera attached to an optical microscope provides another dimension to photography. With a video cameras equipped with optical microscopes, dissolution of metal can be observed instantaneously, so that events taking place at the interface are recorded in micrometer-scale unit. However some artifacts are possible by the use of a video camera. Insufficient or improper lighting can cause poor image quality. Also a video tape, if used as a storage medium, has less resolution than photographic film and finally video cameras are less efficient at gathering light. These difficulties can be overcome by using a S-VHS VCR and video tapes which provide high resolution images and better contrast even in poor lighting environments.

The studies of the potential transients carried out in this work was restricted into

a one-dimensional case. Development of a two-dimensional transmission line model will be necessary for broad applications of this method to various corrosion systems. It was recognized that a certain range of the frequencies, that is a part of a potential transient, can be used to determine the location of the original site of the transient. Using frequency instead of a transient could save time to analyze the transient signal and may be more accurate to determine the location of the corrosion site.

Appendix

When a rectangular pulse initiates at t_1 and ends at t_2 with a magnitude of f_0, Eq. [7-13] becomes

$$g(\omega) = \frac{1}{\sqrt{2\pi}} \int_{t_1}^{t_2} f_o \exp(-i\omega t)\, dt \qquad [A1]$$

By substituting $\exp(-i\omega t) = \cos(\omega t) - i \sin(\omega t)$, Eq. [A1] can be solved:

$$g(\omega) = \frac{f_o}{\sqrt{2\pi}\omega}[(\sin\omega t_2 - \sin\omega t_1) + i\,(\cos\omega t_2 - \cos\omega t_1)]$$

$$= g_1 + i g_2 \qquad [A2]$$

The exponential term in Eq. [7-14] rearranged into its real and imaginary part gives:

$$k(\omega,x) = \exp(-x\sqrt{\frac{R_s}{z(\omega)}}\cos\frac{\theta}{2})[\cos(x\sqrt{\frac{R_s}{z(\omega)}}\sin\frac{\theta}{2}) + i\sin(x\sqrt{\frac{R_s}{z(\omega)}}\sin\frac{\theta}{2})]$$

$$= k_1 + i\, k_2 \qquad [A3]$$

A full description of Eq. [7-14] in terms of g_1, g_2, k_1, and k_2 is

$$G(\omega,x) = g(\omega)\, k(\omega,x) = (g_1k_1 - g_2k_2) + i\,(g_2k_1 + g_2k_1) \qquad [A4]$$

valid at $x = 0$, $k_1 = 1$ and $k_2 = 0$. Therefore, Eq. [A4] is equivalent to Eq. [A2] which

represents the frequency components of the original pulse. The expected pulse transient at a distance x is then calculated by

$$F(t,x) = \frac{1}{\sqrt{2\pi}} \int_{-\infty}^{\infty} G(\omega,x) \exp(i\omega t)\, d\omega \qquad [A5]$$

Since the complex terms drop out, Eq. [A5] becomes

$$\sqrt{2\pi}\, F(t,x) = \int_{-\infty}^{\infty} (g_1 k_1 - g_2 k_2) \cos\omega t\, d\omega + \int_{-\infty}^{\infty} (g_1 k_2 + g_2 k_1) \sin\omega t\, d\omega \qquad [A6]$$

A pulse response using Eq. [A6] can be calculated with a proper integration range and step size ($d\omega$).

Reference

1. Z. Szklarska-Smialowska, *Pitting Corrosion of Metals,* NACE, Houston, Texas (1986).

2. A. J. Sedriks, *Corrosion of Stainless Steels*, John Wiley & Sons, New York (1979).

3. H. H. Uhlig and R. W. Revie, *Corrosion and Corrosion Control*, John Wiley & Sons, New York (1971).

4. J. Stewart, Ph. D. Thesis, University of Southampton, United Kingdom (1991).

5. J. S. Newman, *Electrochemical Systems*, Prentice-Hall, Englewood Cliffs, NJ (1973).

6. T. Hakkarainen, in A. Turnbull (Ed.), *Corrosion Chemistry within Pits, Crevices and Cracks*, p. 17, HMSO, London (1987).

7. F. Hunkeler and H. Böhni, in A. Turnbull (Ed.), *Corrosion Chemistry within Pits, Crevices and Cracks*, p. 27, HMSO, London (1987).

8. H. S. Isaacs and R. C. Newman, in A. Turnbull (Ed.), *Corrosion Chemistry within Pits, Crevices and Cracks*, p. 45, HMSO, London (1987).

9. M. Stern and A. L. Geary, *J. Electrochem. Soc.*, **104**, 56 (1957).

10. R. Oltra and M. Keddam, in H. S. Isaacs, U. Bertocci, J. Kruger, and S. Smialowska (Eds.), *Advances in Localized Corrosion*, p. 17, NACE, Houston, Texas (1990).

11. M. Urquidi-Macdonald and D. D. Macdonald, in H. S. Isaacs, U. Bertocci, J. Kruger, and S. Smialowska (Eds.), *Advances in Localized Corrosion*, p. 33, NACE, Houston, Texas (1990).

12. D. Landolt, in H. S. Isaacs, U. Bertocci, J. Kruger, and S. Smialowska (Eds.), *Advances in Localized Corrosion*, p. 25, NACE, Houston, Texas (1990).

13. Z. Szklarska-Smialowska, in H. S. Isaacs, U. Bertocci, J. Kruger, and S. Smialowska (Eds.), *Advances in Localized Corrosion*, p. 41, NACE, Houston, Texas (1990).

14. T. R. Beck, in H. S. Isaacs, U. Bertocci, J. Kruger, and S. Smialowska (Eds.),

Advances in Localized Corrosion, p. 85, NACE, Houston, Texas (1990).

15. U. Bertocci, in H. S. Isaacs, U. Bertocci, J. Kruger, and S. Smialowska (Eds.), *Advances in Localized Corrosion*, p.126, NACE, Houston, Texas (1990).

16. G. S. Frankel, in H. S. Isaacs, U. Bertocci, J. Kruger, and S. Smialowska (Eds.), *Advances in Localized Corrosion*, p. 137, NACE, Houston, Texas (1990).

17. H. S. Isaacs, in H. S. Isaacs, U. Bertocci, J. Kruger, and S. Smialowska (Eds.), *Advances in Localized Corrosion*, p. 221, NACE, Houston, Texas (1990).

18. J. Newman, in H. S. Isaacs, U. Bertocci, J. Kruger, and S. Smialowska (Eds.), *Advances in Localized Corrosion*, p. 227, NACE, Houston, Texas (1990).

19. R. C. Newman and A. J. Betts, in H. S. Isaacs, U. Bertocci, J. Kruger, and S. Smialowska (Eds.), *Advances in Localized Corrosion*, p. 271, NACE, Houston, Texas (1990).

20. R. P. Frankenthal, in R. W. Staehle and H. Okada (Eds.), *Passivity and its Breakdown on Iron and Iron base Alloys*, p. 10, NACE, Houston, Texas (1976).

21. J. R. Galvele, in R. W. Staehle and H. Okada (Eds.), *Passivity and its Breakdown on Iron and Iron base Alloys*, p. 118, NACE, Houston, Texas (1976).

22. H. H. Uhlig, *J. Electrochem. Soc.*, **97**, 215C (1950).

23. H. H. Uhlig, *Z. Elektrochem.*, **62**, 626 (1958).

24. H. P. Leckie, H. H. Uhlig, *J. Electrochem. Soc.*, **113**, 1261 (1966).

25. Z. Szklarska-Smialowska, in R. Staehle, B. Brown, J. Kruger and A. Agrawal (Eds.), *Proceedings of the U.R. Evans Conference on Localized Corrosion, 1971*, p. 312, NACE, Houston, Texas (1974).

26. Y. M. Kolotyrkin, *J. Electrochem. Soc.*, **108**, 2097 (1961).

27. Y. M. Kolotyrkin, *Corrosion*, **19**, 261t (1963).

28. K. E. Heusler and L. Fisher, *Werkstoffe Korros.*, **27**, 551, 697 and 788 (1976).

29. M. Janik-Czachor, A. Szummer and Z. Szklarska-Smialowska, *Corros. Sci.*,

15, 75 (1975).

30. M. Janik-Czachor, *J. Electrochem. Soc.*, **128,** 513C (1981).

31. U. R. Evans, *J. Chem. Soc. London,* (1927) 1020.

32. T. P. Hoar, D. C. Mears, and G. P. Rothwell, *Corros. Sci.*, **5,** 279 (1965).

33. I. L. Rozenfeld and I. K. Marshakov, *Corrosion,* **20,** 115t (1964).

34. G. A. Basset and C. Edeleanu, *Phil. Mag.*, **5,** 1217 (1960).

35. M. J. Pryor, in in R. Staehle, B. Brown, J. Kruger and A. Agrawal (Eds.), *Proceedings of the U.R. Evans Conference on Localized Corrosion, 1971*, p. 312, NACE, Houston, Texas (1974).

36. N. Sato, *Electrochim. Acta,* **19,** 1683 (1971).

37. T. P. Hoar, *Corros. Sci.*, **7,** 88 (1967).

38. J. R. Galvele, *Corros. Sci.*, **21,** 551 (1981).

39. J. R. Galvele, J. B. Lumsden, and R. W. Staehle, *J. Electrochem. Soc.*, **125,** 1204 (1978).

40. J. R. Galvele, *J. Electrochem. Soc.*, **123,** 464 (1976).

41. Z. Szklarska-Smialowska, *Br. Corros. J.*, **10,** 11 (1975).

42. C. Y. Chao, L. F. Lin, and D. D. Macdonald, *J. Electrochem. Soc.*, **128,** 1187 (1981).

43. L. F. Lin, C. Y. Chao, and D. D. Macdonald, *J. Electrochem. Soc.*, **129,** 1194 (1981).

44. M. Urquidi and D. D. Macdonald, *J. Electrochem. Soc.*, **132,** 557 (1985).

45. D. D. Macdonald and M. Urquidi-Macdonald, *J. Electrochem. Soc.*, **137,** 2395 (1990).

46. R. T. Foley, in R. W. Staehle and H. Okada (Eds.), *Passivity and its Breakdown on Iron and Iron base Alloys*, p. 32, NACE, Houston, Texas (1976).

47. S. E. Traubenberg and R. T. Foley, *J. Electrochem. Soc.*, **118,** 1026 (1971).

48. K. J. Vetter, *Ber. Bunsenges. Phys. Chem.*, **66**, 589, 683 (1965).

49. A. P. Honess, *The Nature, Origin and Interpretation of Etch Figures on Crystals*, John Wiley, New York (1927).

50. K. Asami, K. Hashimoto, and S. Shimodaira, *Corros. Sci.*, **18**, 151 (1978).

51. R. P. Frankenthal and D. L. Malm, in R. W. Staehle and H. Okada (Eds.), *Passivity and Its Breakdown on Iron Base Alloys*, p. 77, NACE, Houston, Texas (1976).

52. G. Okamoto, K. Tashibana, T. Shibata, and K. Hoshino, *J. Japan Inst. Met.*, **38**, 684 (1974).

53. S. C. Tjong, J. Eldridge, R. Hoffman, R. Henemann and E. Yeager, in R. Frankenthal (Ed.), *Corrosion and Corrosion Protection Processes, Proc. Int. Symp. Honoring H. H. Uhlig's 75th Birthday*, **Vol 81-8**, p. 50, The Electrochemical Society, Princeton, New Jersey (1981).

54. I. Olefjord and B.-O. Elfstrom, *Corrosion*, **38**, 46 (1982).

55. G. J. Barnes, A. W. Aldag, and R. C. Jerner, *J. Electrochem. Soc.*, **119**, 684 (1972).

56. D. M. Hercules, *Anal. Chem.*, **42**, 20A (1970).

57. K. Sugimoto and Y. Sawada, *Corros. Sci.*, **17**, 425 (1977).

58. A. T. Fromhold and S. J. Noh, *Corros. Sci.*, **29**, 237 (1989).

59. A. Di Paola, D. Shukla and U. Stimming, *Electrochimica Acta*, **36**, 345 (1991).

60. C. R. Clayton and Y. C. Lu, *J. Electrochem. Soc.*, **133**, 2465 (1986).

61. M. Urretabizkya, C. D. Pallotta, N. De Cristofaro, R. C. Salvarezza and A. J. Arvia, *Electrochimica Acta*, **33**, 1645 (1988).

62. A. J. Davenport, H. S. Isaacs, G. S. Frankel, A. G. Schrott, C. V. Jahnes, and M. A. Russak, *J. Electrochem. Soc.*, **138**, 337 (1991).

63. J. A. Bardwell, G. I. Sproule, B. MacDougall, M. J. Graham, A. J. Davenport, and H. S. Isaacs, *J. Electrochem. Soc.*, **139**, 371 (1992).

64. M. Pourbaix, *Corrosion*, **26**, 431 (1970).

65. S. Brennert, *J. Iron Steel Inst.*, **135**, 101 (1936).

66. W. Batista, A.M.T. Louvisse, O. R. Mattos, and L. Sathler, *Corros. Sci.*, **28**, 759 (1988).

67. Z. Szklarska-Smialowska, *Corrosion*, **27**, 223 (1971).

68. J. O'M. Bockris and A. K. N. Reddy, *Modern Electrochemistry*, Vol. 2, p. 883, 1287, Plenum Press, New York (1970).

69. A. J. Bard and L. R. Faulkner, *Electrochemical Methods Fundamentals and Applications*, Chapter 3 and 4, John Wiley & Sons, New York (1980).

70. J. Tafel, *Z. Physik. Chem.*, **50A**, 641 (1905).

71. J.W. Oldfield and W.H. Sutton, *British Corrosion Journal*, **13**, 104 (1978).

72. A. Turnbull and D.H. Ferriss, *Corrosion Sci.*, **27**, 1323 (1987).

73. S.M. Sharland and P.W. Tasker, *Corrosion Sci.*, **28**, 603 (1988).

74. S.M. Sharland, C.P. Jackson and A.J. Diver, *Corrosion Sci.*, **29**, 1149 (1989).

75. J.C. Watson, *Corrosion Sci.*, **30**, 915 (1990).

76. K. Hebert and R. C. Alkire, *J. Electrochem. Soc.*, **130**, 1007 (1983).

77. J. N. Harb and R. C. Alkire, *J. Electrochem. Soc.*, **138**, 2594 (1991).

78. B.G. Ateya and H.W. Pickering, *"Passivity of Metals"*, Eds. R. P. Frankenthal and J. Kruger, p.350, The Electrochemical Society, Princeton, New Jersey (1978).

79. M. Watson and J. Postlethwaite, *Corrosion*, **46**, 522 (1990).

80. J. A. Beavers and N. G. Thompson, *Corrosion*, **43**, 185 (1987).

81. J. W. Tester and H.S. Isaacs, *J. Electrochem. Soc.*, **122**, 1438 (1975).

82. E. McCafferty, *J. Electrochem. Soc.*, **128**, 39 (1981).

83. R. C. Alkire, D. Ernsberger and D. Damon, *J. Electrochem. Soc.*, **123**, 458 (1976).

84. A. Turnbull, *Corrosion Sci.*, **23**, 833 (1983).

85. G. Butler, P. Stretton and J. G. Beynon, *British Corrosion Journal*, **7**, 168 (1972).

86. H. W. Pickering and R. P. Frankenthal, in *Proceedings of the U.R. Evans Conference on Localized Corrosion, 1971*, Eds. R. Staehle, B. Brown, J. Kruger and A. Agrawal, NACE, p. 261, Houston, Texas (1974).

87. J. A. Davis, in *Proceedings of the U.R. Evans Conference on Localized Corrosion, 1971*, Eds. R. Staehle, B. Brown, J. Kruger and A. Agrawal, NACE, p. 168, Houston, Texas (1974).

88. Z. Szklarska-Smialowska and J. Mankowski, *Corros. Sci.*, **12**, 925 (1972).

89. M. B. Ives and J. L. Luo, *11th International Corrosion Congress*, Paper No. 88, Firenze, Italy, April, (1990).

90. J. A. Smith, M. H. Peterson and B. F. Brown, *Corrosion*, **26**, 539 (1970).

91. D. A. Meyn, *Metal Trans.*, **2**, 853 (1971).

92. S. E. Lott and R. C. Alkire, *Corrosion Sci.*, **28**, 479 (1988).

93. B. K. Nash and R. G. Kelly, *J. Electrochem. Soc.*, **139**, L47 (1992).

94. J. E. Castle and J. H. Qiu, *J. Electrochem. Soc.*, **137**, 2031 (1990).

95. T. Tsuru, K. Hashimoto, A. Nishikata and S. Haruyama, *Material Science Forum*, **44&45**, 289 (1989).

96. M. J. Apted, G. A. Waychunas and G. E. Brown, *Geochim. Cosmochim. Acta*, **49**, 2081 (1985).

97. Y. H. Lee, Z. Takehara and S. Yoshizawa, *Corros. Sci.*, **21**, 391 (1981).

98. L. Sathler, J. Van Muylder, R. Winand and M. Pourbiax, *7th Int. Cong. Metallic Corrosion*, Rio de Janeiro (1978).

99. F. van Langevelde and R. D. Vis, *Anal. Chem.*, **63**, 2253 (1991).

100. H. S. Isaacs, A. J. Davenport, J. H. Cho, M. Rivers and S. Sutton, in *Proceedings of the Symposium on X-ray Methods in Corrosion and Interfacial Electrochemistry*, Eds: A.J. Davenport and J.G. Gordon, **PV 92-1**, p. 354, The

Electrochemical Society, Phoenix, Arizona, October (1991).

101. H. S. Isaacs and Y. Ishikawa, *J. Electrochem. Soc.*, **132**, 1288 (1985).

102. J. Mankowski and Z. Szklarska-Smialowska, *Corros. Sci.*, **15**, 493 (1975).

103. M. Takahashi, *Boshoku Gijutsu*, **23**, 625 (1974).

104. W. Yang, R. Ni, H. Hua, and A. Pourbaix, *Corros. Sci.*, **24**, 691 (1984).

105. W. J. Muller, *Die Bedeckungstheorie der Passivitat der Metalle under ihre Experimentelle Begrundung*, Verlag-Chemie, Berlin (1933).

106. R. Weiner and F. Halla, *Z. Elektrochem.*, **48**, 361 (1942).

107. W. Machu and A. Ragheb, *Werkst. Korros.*, **4**, 429 (1953).

108. T. P. Hoar, in *Modern Aspects of Electrochemistry*, Vol. 2, Ed. J. O'M. Bockris, p. 262, Butterworths, London (1959).

109. K. J. Vetter and H.-H. Strehblow, *Ber. Bunsenges. Phys. Chem.*, **74**, 1024 (1970).

110. H.-H. Strehblow and J. Wenners, *Z. Phys. Chemie. N.F.*, **98**, 199 (1975).

111. T. R. Beck, *J. Electrochem. Soc.*, **120**, 1310, 1318 (1973).

112. H. S. Isaacs, *J. Electrochem. Soc.*, **120**, 1456 (1973).

113. H. C. Kuo and D. Landolt, *Electrochimica Acta*, **20**, 393 (1975).

114. H. C. Kuo and D. Landolt, *Corros. Sci.*, **16**, 915 (1976).

115. K. J. Vetter and H.-H. Strehblow, *Localized Corrosion*, NACE 3, pp. 240-251, Houston, TX (1974).

116. T. R. Beck and R. C. Alkire, *J. Electrochem. Soc.*, **126**, 1662 (1979).

117. R. C. Alkire, D. Ernsberger and T. R. Beck, *J. Electrochem. Soc.*, **125**, 1382 (1978).

118. I. L. Rosenfeld, I. S. Danilov and R. N. Oranskaya, *J. Electrochem. Soc.*, **125**, 1729 (1978).

119. T. R. Beck, *J. Electrochem. Soc.*, **129**, 2412 (1982).

120. F. Hunkeler, A. Krolikowski and H. Bohni, *Electrochimica Acta*, **32**, 615 (1987).

121. M. J. Danielson, *J. Electrochem. Soc.*, **135**, 1326 (1988).

122. W. Li, X. Wang and K. Nobe, *J. Electrochem. Soc.*, **137**, 1184 (1990).

123. C. Clerc and D. Landolt, *Electrochimica Acta.*, **33**, 859 (1988).

124. W. P. Iverson, *J. Electrochem. Soc.*, **115**, 617 (1968).

125. H. H. Uhlig, *Corrosion and Corrosion Control*, p. 231, John Wiley & Sons, New York (1963).

126. C. Blanc, C. Gabrielli and M. Keddam, *Electrochimica Acta.*, **20**, 687 (1975).

127. I. Epelboin, C. Gabrielli, M. Keddam and L. Railon, *J. Electroanal. Chem.*, **93**, 155 (1978).

128. P. C. Searson and J. L. Dawson, *J. Electrochem. Soc.*, **135**, 1908 (1988).

129. S. Magaino, A. Kawaguchi, A. Hirata and T. Osaka, *J. Electrochem. Soc.*, **134**, 2993 (1987).

130. H. J. Pearson, G. T. Burstein and R. C. Newman, *J. Electrochem. Soc.*, **128**, 2297 (1981).

131. R. P. Wei, M. Gao and P. Y. Xu, *J. Electrochem. Soc.*, **136**, 1835 (1989).

132. R. G. Kelly and R. C. Newman, *J. Electrochem. Soc.*, **137**, 357 (1990).

133. J. Newman, *J. Electrochem. Soc.* **117**, 198 (1970).

134. R. Oltra, G. M. Indrianjafy, J. C. Colson and M. Keddam, *11th International Corrosion Congress*, Florence, Italy, April (1990).

135. H. S. Isaacs, A. J. Davenport and P. J. Rulon 3, *Corrosion 89*, NACE (1989) Paper No. 29.

136. H. S. Isaacs and A. J. Davenport, *J. Electrochem. Soc.*, **137**, 2196 (1990).

137. J. R. Macdonald, *Impedance Spectroscopy*, p. 5, John Wiley & Sons, New York (1987).

138. K. S. Cole and R. S. Cole, *J. Chem. Phys.*, **9**, 341 (1941).

139. E. Warburg, *Ann. Phys. Chem.*, **67**, 493 (1899).

140. J. R. Macdonald, *J. Electroanal. Chem.* , **223**, 25 (1987).

141. B. B. Mandelbrot, *The Fractal Geometry of Nature*, Freeman, San Francisco (1982).

142. A. Le Mehaute and G. Crepy, *Solid State Ionics*, **9/10**, 17 (1983).

143. H. Liu, *Phys. Rev. Lett.*, **55**, 529 (1985).

144. G. Kahanda and M. Tomkiewicz, *J. Electrochem. Soc.*, **137**, 3423 (1990).

145. U. Rammelt and G. Reinhard, *Electrochim. Acta*, **35**, 1045 (1990).

146. R. Oltra and M. Keddam, *Corrosion Sci.*, **28**, 1 (1988).

147. R. Oltra and M. Keddam, *Electrochim. Acta*, **35**, 1619 (1990).

148. A. Roelandt and J. Vereecken, *Surf. Technol.*, **9**, 347 (1979).

149. T. E. Springer and I. Raistirck, *1st International Symposium on EIS*, Ext. Abst. C2.1 (1989).

150. K. Juttner, *Electrochim. Acta*, **35**, 1501 (1990).

151. F. Mansfeld, M. W. Kendig and S. Tsai, *Corrosion*, **38**, 478 (1982).

152. F. Mansfeld, *Corrosion*, **44**, 858 (1988).

153. F. K. Crundwell, *Electrochim. Acta*, **36**, 1183 (1991).

154. R. de Levie, in *Advances in Electrochemistry and Electrochemical Engineering*, Ed. R. Delahay, Vol.VI. p. 329 Interscience, New York (1967).

155. D. D. Macdonald, M. C. H. McKubre and M. Urquidi-Macdonald, *Corrosion*, **44**, 2 (1988).

156. C. Fiaud, M. Keddam, A. Kadri and H. Takenouti, *Electrochim. Acta*, **32**, 445

(1987).

157. J. H. Cho, H. S. Isaacs, and A. J. Davenport, *Extended Abst.*, **89-2**, No. 147, Electrochemical Society meeting, Hollywood, FL, October (1989).

158. S. Paull, " Topics in Advanced Mathematics For Electronics Technology", John Wiley & Sons, Inc., New York (1966).

159. B. Dziunikowski, *Energy Dispersive X-ray Fluorescence Analysis*, Elsevier Science Publishing, NY (1989).

160. T. B. Johansson, *Nucl. Instr. Meth.*, **84**, 141 (1970).

161. F. Folkmann, *Nucl. Instr. Meth.*, **116**, 487 (1970).

162. S. Fine and C. F. Hendee, *Nucleonics*, **13 (3)**, 36 (1955).

163. H. Hall, *Phis. Rev.*, **84**, 167 (1951).

164. R. Jenkins and J. L. De Vries, *Principal X-Ray Spectrometry*, Philips Technical Library, Macmillan and Co., London (1970).

165. G. E. Gigante and A. L. Hanson, *Basic Principles of Synchrotron Radiation-Induced X-ray Fluorescence (SRXRF)*, BNL-44768, Brookhaven National Laboratory, Upton, NY (1990).

166. H. S. Lucas-Tooth and E. C. Pyne, *Advances in X-Ray Analysis*, Vol. 7, Plenum Press, New York, p. 523 (1964).

167. J. W. Criss and L. S. Birk, *Anal. Chem.*, **20**, 1080 (1968).

168. J. W. Criss, *NRLXRF, A FORTRAN Program for X-ray Fluorescence Analysis*, Naval Research Laboratory, Washington, D.C. (1977).

169. J. W. Millor, *A Comprehensive Treatise on Inorganic and Theoretical Chemistry*, Vol. XV, Longmans, Green and Co., London (1940).

170. R. C. Weast, *CRC Handbook of Chemistry and Physics*, 66th edition, CRC Press Inc., Boca Raton, Florida (1985).

171. J. Sherman, *Spectrochim. Acta*, **7**, 283 (1952).

172. J. Sherman, *Spectrochim. Acta*, **15**, 466 (1959).

173. T. Shiraiwa and N. Fujino, *Japan. J. Appl. Phys.*, **5**, 886 (1966).

174. L. X. Zhang, *X-ray Spectroscopy*, **13**, 52 (1984).

175. R. Jenkins, in *X-ray Spectrometry*, Eds. H. K. Herglotz and L. S. Birks, p. 241, Marcel Dekker, Inc., New York (1978).

176. R. O. Muller, *Spectrochemical Analysis by Fluorescence*, Adam Hilger Ltd., London (1977).

177. Woldseth, *XES Energy Spectroscopy*, Kevex Corp., Burlingame, Vt (1973).

178. L. H. Schwart and J. B. Cohen, *Diffraction from Materials*, Springer-Verlag, Berlin, Heidelberg (1987).

179. H. Winick, G. Brown, K. Halbach and J. Harris, *Physics Today*, May, p. 50 (1981).

180. G. von Hevesy, *Chemical Analysis by X-Ray and Its Applications*, McGrew-Hill, New York (1932).

181. Y. Wu, A. C. Thompson, J. H. Underwood, R. D. Gaiuque, K. Chapman, M. L. Rivers and K. W. Jones, *Nucl. Inst. and Methods*, **A291**, 146 (1990).

182. K. W. Jones, in *Advances in X-Ray Analysis*, Eds. C. S. Barrett, J. V. Gilfrich, R. Jenkins, J. C. Russ, J. W. Richdson, Jr., P. K. Predecki, Plenum Publishing Co., New York (1988).

183. K. W. Jones and B. M. Gordon, *Anal. Chem.*, **61**, 341A (1989).

184. H. You, Z. Nagy, C. A. Melendres, D. J. Zurawski, R. P. Chiarello, R. M. Yonco, H. K. Kim and V. A. Maroni, in *Proceedings of the Symposium on X-ray Methods in Corrosion and Interfacial Electrochemistry*, Eds: A.J. Davenport and J.G. Gordon, **PV 92-1**, p. 73, The Electrochemical Society, Fall Meeting, Phoenix, Arizona, October (1991).

185. S. Inoue, *Video Microscopy*, Plenum Press, New York (1987).

186. H. S. Isaacs, A. J. Davenport and A. Shipley, *J. Electrochem. Soc.*, **138**, 390 (1991).

187. L. McVay, R. H. Muller and C. W. Tobias, *J. Electrochem. Soc.*, **136**, 3384 (1989).

188. R. H. Stokes, S. Phang and R. Mills, *J. Solution Chem.*, **8**, 489 (1979).

189. B. Y. Enwiya, J. Silver and I. E. G. Morrison, *J. Chem. Soc. Dalton Trans.*, (1982) 2231.

190. J. Epelboin, P. Morel and H. Takenouti, *J. Electrochem. Soc.*, **118**, 1282 (1971).

191. L. Young, Trans. *Faraday Soc.*, **51**, 1250 (1955).

192. M. W. Kendig, F. Mansfeld and S. Tsai, *Corros. Sci.*, **23**, 317 (1983).

193. A. K. Jonscher, *Phys. St. Sol.*, **A32**, 665 (1975).

194. J. F. McCann and S. P. S. Badwal, *J. Electrochem. Soc.*, **129**, 551 (1982).

195. J. H. Cho, A. J. Davenport and H. S. Isaacs, to be published.

196. C. Gabrielli, M. Ksouri and R. Wiart, *J. Electroanal. Chem.*, **86**, 234 (1978).

197. G. Okamoto and T. Shibata, in R. P. Frankenthal and J. Kruger (Eds.), *Passivity of Metals*, p. 646, The Electrochemical Society Softbound Proceedings Series, Princeton, NJ (1978).

198. U. Bertocci, *J. Electrochem. Soc.*, **127**, 1931 (1980).

199. U. Bertocci, *J. Electrochem. Soc.*, **128**, 520 (1981).

200. U. Bertocci and J. Kruger, *Surf. Sci.*, **101**, 608 (1980).

201. H. S. Isaacs, J.-H. Cho, A. J. Davenport and G. S. Frankel, *Corrosion 92*, paper No. 217, Nashville, Tennessee, April 27 - May1 (1992).

202. M. L. Rivers, personal communication.